Physical-chemical studies of transfection lipids in 2D and 3D model systems

Dissertation

zur Erlangung des

Doktorgrades der Naturwissenschaften (Dr. rer. nat.)

der

Naturwissenschaftlichen Fakultät I

– Biowissenschaften –

der Martin-Luther-Universität Halle-Wittenberg,

vorgelegt von

Frau M.Sc. Dorota Pawlowska

geb. am 29. August 1985 in Ketrzyn, Polen

Gutachter:

1. Prof. Dr. Bodo Dobner

2. Prof. Dr. Gerald Brezesinski

3. Prof. Dr. Reinhard Neubert

Halle (Saale), November 2014   verteidigt am 21.01.2015

Dla mojej rodziny i ukochanego męża.

CONTENTS

ABSTRACT

This work focuses on the physical-chemical characterization of several newly designed and synthesized lipids for gene transfection, the results of which have been correlated with *in-vitro* gene transfection efficiency. Single lipids as well as their lipoplexes have been tested. The main focus has been put on the influence of small changes in lipid structure on overall properties and gene delivery performance. Lipids with small differences in their hydrocarbon chains or headgroups as well as their purity have been investigated.

Substances have been examined as single lipid systems as well as complexes with helper lipids and model DNA (lipoplexes). Monolayer techniques (2D) as Langmuir trough, IRRAS and GIXD were employed to investigate single lipid systems and their interaction with DNA. Single lipids and their mixtures with helper lipid (DOPE or cholesterol) as well as lipoplexes were tested in bulk systems (3D) with SAXS, WAXS and DSC.

In **chapter one** the chemical-physical properties of monolayers and aggregates of two lipids of the same chemical structure but different chain purity were investigated. The difference of grade of the lipid samples comes from the purity of the chain precursor used for the synthesis. The much more cost effective technical grade lipid has been found to be much better for transfection, due to the membrane structure disturbance caused by other components of this multicomponent system. The lipid of analytical purity almost did not transfect, even though it shows several important properties which are believed to improve transfection efficiency (cubic phase formation, *cis*-configuration of the double bond).

Chapter two compares the physical-chemical properties of three lipids of the same chain structure but whose headgroups differ in size and charge. The lipids have been examined in monolayer systems. They show typical trends of growing fluidity with growing size and charge of their headgroups. The attempt of correlating the results with transfection efficiency was made. The lipid with the largest and most charged headgroup region was found the best for transfection. The other two lipids showed very similar transfection performance even though the differences in headgroups structure were quite significant.

Chapter three describes two lipids of the same headgroup but which differ in the structure of one of two acyl chains. One lipid is fully saturated and the second has one double bond in one of chains. The lipids have been examined in monolayers as well as hydrated aggregates. Even though they do show dissimilarities in physical-chemical properties that come from their different fluidity, there is no pronounced difference in their transfection efficiency.

ZUSAMMENFASSUNG

Diese Arbeit ist auf die physikalisch-chemische Charakterisierung einiger neu entwickelter und synthetisierter Lipide für die Gentransfektion ausgerichtet. Die Ergebnisse dieser Studien wurden mit der Effizienz von *in vitro* Gentransfektionsexperimenten korreliert. Einzelne Lipide als auch die entsprechenden Lipoplexe wurden untersucht. Das Hauptaugenmerk wurde auf den Einfluss kleiner Änderungen in der Lipidstruktur auf die Eigenschaften aggregierter Systeme und die Transfektionseffizienz gelegt. Lipide mit kleinen Unterschieden in der Ketten- oder Kopfgruppenstruktur als auch in ihrer Reinheit wurden untersucht.

Die Verbindungen wurden als Einkomponentensysteme als auch als Komplexe mit den entsprechenden Helferlipiden und Modell-DNA (Lipoplexe) untersucht. Monoschichttechniken (2D) wie Langmuir Trog, IRRAS und GIXD wurden eingesetzt, um sowohl Einkomponentensysteme als auch deren Wechselwirkung mit DNA zu untersuchen. Die einzelnen Lipide und deren Mischungen mit Helferlipiden (DOPE oder Cholesterol) als auch die entsprechenden Lipoplexe wurden auch in Volumensystemen (3D) mittel SAXS, WAXS und DSC untersucht.

In **Kapitel 1** werden die physikalisch-chemischen Eigenschaften von Monoschichten und Volumenaggregaten von zwei Lipiden, die die gleiche chemische Struktur aber eine deutlich unterschiedliche Kettenreinheit aufweisen, beschrieben. Die unterschiedliche Reinheit rührt von der unterschiedlichen Reinheit der in der Synthese eingesetzten Vorprodukte. Die kostengünstigere Verbindung mit technischem Gütegrad ist wesentlich besser für die Transfektion, offensichtlich wegen der Membranstörung durch die zusätzlichen Komponenten in der Mehrkomponenten Verbindung. Das hochreine Lipid transfiziert praktisch überhaupt nicht obwohl es einige wichtige Eigenschaften (kubische Struktur, cis-Konfiguration der Doppelbindung), die als wesentlich für eine Steigerung der Transfektionseffizienz angesehen werden, aufweist.

In **Kapitel 2** werden die physikalisch-chemischen Eigenschaften von drei Lipiden mit gleicher Kettenstruktur aber Unterschieden in der Kopfgruppenstruktur und Ladung verglichen. Diese Lipide wurden in 2D Monoschichten untersucht. Der erwartete Trend einer Fluidisierung mit wachsender Größe und Ladung der Kopfgruppe wird beobachtet. Es wurde versucht diese Ergebnisse mit der Transfektionseffizienz zu korrelieren. Das Lipid mit der größten und am stärksten geladenen Kopfgruppe ist am effektivsten, Die

beiden anderen Lipide zeigen sehr ähnliche Transfektionsleistungen obwohl die Unterschiede in der Kopfgruppenstruktur signifikant sind.

In **Kapitel 3** werden zwei Lipide beschrieben, die die gleiche Kopfgruppenstruktur aber unterschiedliche Kettenmuster besitzen. Ein Lipid hat zwei gesättigte Kohlenwasserstoffketten während das andere eine gesättigte Kette und eine Kette mit einer Doppelbindung hat. Die Lipide wurden als Monoschichten und als wässrige Dispersionen untersucht. Obwohl sie Unterschiede in den physikalisch-chemischen Eigenschaften aufweisen, die auf der unterschiedlichen Fluidität basieren, sind keine merklichen Unterschiede in der Transfektionseffizienz zu beobachten.

ABBREVIATIONS AND SYMBOLS

2D	two dimensional
3D	three dimensional
A_0	cross-section area
BAM	Brewster angle microscopy
ctDNA	calf thymus DNA
d	lamellar repeat distance of lipid bilayer plus one layer of water in bulk
DC-Chol	3β-[N-(N',N'-dimethylaminoethane)-carbamoyl]cholesterol
DODAB	dioctadecyldimethylammonium bromide
DODAC	N,N-dioleyl- N,N-dimethylammonium chloride
DODAP	1,2-dioleoyl-3-dimethylammonium-propane
DOGS	di-octadecyl-amido-glycyl-spermine
DOPE	dioleoylphosphatidylethanolamine
DOSPA	2,3-dioleyloxy-N-[2(sperminecarboxamido)ethyl]-N,N-dimethyl-l-propanaminium trifluoroacetate
DOTMA	N-(1-[2,3-dioleyloxy]propyl)-N,N,N-trimethylammonium chloride
DR	dichroic ratio
DSC	differential scanning calorimetry
eq.	equation
FWHM	full-width at half-maximum
GIXD	grazing incidence x-ray diffraction
ΔH_m	phase transition enthalpy (gel to liquid-crystalline state in bulk)
H_I	hexagonal phase in bulk
H_{II}	inverted hexagonal phase in bulk
IRRAS	infrared reflection-absorption spectroscopy
L_α	lamellar liquid phase in bulk
L_β	lamellar gel phase
$L_{\beta'}$	lamellar gel phase with tilted chains
L_C	cholesterol phase in bulk
LC	liquid-condensed phase in monolayer systems
$LC_{t=0}$	liquid-condensed phase of non-tilted chains in monolayer systems
LE	liquid-expanded phase state in monolayer systems
NN	nearest neighbor
NNN	next nearest neighbor
N/P ratio	ratio of moles of amine groups of cationic lipid and phosphate groups of DNA
π	surface pressure
$\pi_{t'}$	pressure of the phase transition from tilted to untilted phase
π_{tr}	phase transition pressure
Q	Cubic phase
Q_{xy}	vertical scattering vector
Q_z	horizontal scattering vector
SAINT	2 - N-methyl-4(dioleyl)methylpyridiniumchloride
SAXS	small-angle x-ray scattering

T_0	the temperature below which the LE phase exists no longer
T_c	critical temperature above which no LE state exists
T_m	melting temperature, in the text T_m refers often to the phase transition temperature (gel to liquid-crystalline state in bulk)
T_{PT}	phase transition temperature
$v_{as}(CH_2)$	asymmetric CH_2-stretching vibration
$v_s(CH_2)$	symmetric CH_2-stretching vibration
WAXS	wide-angle x-ray scattering
wt%	weight percent

INTRODUCTION

Gene therapy, a term to describe the supplementation or alternation of defected genes, is a promising method for curing genetic diseases. Extensive studies in this field have been performed worldwide since early 1970's [1,2]. Many of the proposed therapeutic systems have been tested on animals or humans but few clinical trials have given positive results [3-5] and so far no routine gene therapy treatment is available for people suffering from genetic defects. After years of research, the first treatment of its kind, which compensates for lipoprotein lipase deficiency (known as Glybera) has been approved in the European Union, Israel and Palestine and has been given access to the pharmaceutical market 6. Nevertheless, the few successes have shown promise and have become a driver for further study. The major disadvantage of existing systems is their low efficiency in delivering genetic material into a single cell already in *in-vitro*, which precludes them from *in-vivo* tests. Hence, many studies in this field focus on finding new DNA/RNA vectors as well as improving existing ones. There are many methods of introducing the foreign genetic material into a cell [7,8]. They are basically categorized into two systems: viral and non-viral. The recombinant virus carriers (viral vectors) are considered more efficient, because of their natural ability to insert their own genetic material into the host cell replication cycle. But they also suffer from number of drawbacks like high immunogenicity (the natural response of human body to viral infection), limited size (unable to incorporate large DNA/RNA fragments) and risk of uncontrolled mutations. Moreover, their production processes are difficult and expensive. Nonetheless, viruses have been the most widely used gene transfection vectors for clinical applications thus far [9-11]. However, the alternative, non-viral systems are constantly being developed [12-14]. Complexes of nucleic acid with cationic lipid, called lipoplexes, have become the most popular of alternatives to viral systems since their applicability in gene transfection was first reported by Felgner et al. in 1987[15]. The general advantages of lipoplexes over viruses are mainly low immunogenicity and feasibility of large scale production at lower cost. Apart from that, liposomes can host all kinds of nucleic acids in large quantities and are suitable for a wide range of cell types [16-18]. The general mechanism of lipofection (lipid mediated transfection) relies on

electrostatic attraction between positively charged lipid and negatively charged nucleic acid. Sometimes, a non-charged helper lipid is used to maintain a given charge density. An overall positive charge of the complex enables its attachment to the negatively charged cell membrane and uptake by endocytosis. Even though the exact mechanism of cytoplasmic delivery remains unclear, it is in no doubt that the structure of lipoplex, its phase behavior and fusogenic properties play a crucial role in interaction with the cell membrane, entrapment and release from the endosome compartment and transfer of RNA from the endosome to cytosol or DNA to nucleus [19-21]. Experiments on lipid model systems serve as the first step in the analysis of interactions between lipoplexes and a cell membrane. Careful fundamental study of lipids in bulk and monolayers can help to find the most important properties that make a given system useful for transfection. A great variety of new amphiphiles has been systematically synthesized and their biophysical properties have been investigated and correlated with *in-vitro* and *in-vivo* transfection efficiencies [22-25]. Since most of the synthesized cationic lipids can be easily chemically modified, fast system optimization as well as targeting is possible.

1. GENE TRANSFECTION

Transfection, the change of cell properties by the introduction and expression of foreign genetic material, is one of the most promising methods for curing many illnesses. The approach targets the origin of the disease and not just its symptoms. It can be used either to treat deficiencies caused by faultily expressed genes (for diseases as cystic fibrosis) [26] or suicide therapy in the case of cancer [27]. The term "gene transfection" describes a wide variety of methods that allow fixing faulty mechanisms which are based on genetic disorders in an animal eukaryotic cell. It includes delivery of missing or defected gene or its alternation by external DNA as well as the delivery of RNA that acts as a posttranscription agent. Here, mainly mRNA (messenger RNA) carrying the information about a protein sequence [28] and siRNA (small interfering RNA), that silences the expression of the gene of interest, were studied [29]. Due to the body's defense mechanisms, the external nucleic acid applied to a body at the physiological level is degraded by nucleases and does not reach the desired destination. It applies especially to very unstable one-stranded RNA. This obstacle can be overtaken by a carrier use or a

physical admission directly to the target cell.

1.1 GENE DELIVERY METHODS

For the purpose of introducing nucleic acid to the cell, transfection methods can be generally divided into three main groups: physical methods, virus-based systems and nonviral vector systems.

1.1.1 Physical methods

Physical methods are very suitable for single cell experiments, since usually the physical force must be aimed and applied very precisely, but there are techniques that enable using them also for tissue or *in-vivo* studies. Most of the physical methods utilize pore formation in the cell membrane. It has been achieved by electroporation, sonoporation, hydroporation, or through a laser. Naked DNA simply enters a cell through pores. There are also very precise methods that allow controlling the amount of the introduced DNA, such as needle injection and the gene gun (propelling DNA-coated gold nanoparticles into a cell). Apart from those, magnetofection is also used. This method employs magnetic particles of zinc oxide complexed with DNA that are concentrated on a target cell by external magnetic field and uptaken by endo- or pinocythosis. The physical approaches attract a lot of interest due to their simplicity; however, they show relatively low transfection efficiencies. Additionally, when used *in-vivo*, most of them can be utilized only for body cells that lay quite shallow (like skin) or others that can be easily surgically exposed [30].

1.1.2 Viral vectors

The second group of transfection methods is based on viral delivery systems. These have been used mainly in clinical trials so far. Viruses have evolved a natural ability of infecting cells and of employing its mechanisms to express virus genes, allowing virus particles to multiply. The genome of virus particles used for transfection is modified by the deletion of disease causing sequences and the introduction of the gene of interest. Both, DNA and RNA viruses have been used. The general feature that differentiates these two is the mechanism of their life cycle: RNA viruses integrate their genome with a host cell chromosome that results in long term expression, and DNA viruses usually express

their genes aside the cell nucleus (without integration). Thus far, several groups of viruses have been examined for transfection capability. The type used most commonly is the RNA retrovirus but DNA viruses like adenoviruses, adenovirus-associated viruses and herpes simplex viruses were also investigated [7,31]. Even though the viral vectors have shown the best transfection efficiencies, they have been also described as the most hazardous of any of the delivery systems. They are the natural enemies of living organisms so their introduction into a body almost always induces serious immunological response. Moreover viruses tend to recombine and mutate in uncontrollable ways [32]. Another disadvantage that limits their use is the virus particle size that constrains the amount of the genetic material that may be carried. They are, in addition, expensive and complicated to produce, thus limiting their use in fast trial processes [33,34].

1.1.3 Non-viral vectors

The disadvantages of viral systems have led to the development of other carriers. The strategy is based on the use of a compound that complexes the nucleic acid, typically cationic substances like lipids or polymers. This approach gives much lower transfection efficacies but the systems are less toxic and easier to formulate than viral vectors. Moreover, they are easy to modify and produce on a large scale at low cost. They have, however, serious drawbacks with their use *in-vivo*; generally, by inducing immune responses and, specifically, by their accumulation in lung capillary systems. Nevertheless, non-viral vectors are considered to have fewer safety concerns than viral systems. [35-37]. Cationic lipids for gene transfection are the subject of this work and will be described later.

2. CATIONIC LIPID MEDIATED TRANSFECTION

Lipid mediated transfection was first reported by Felgner in 1987 [15]. He used DOTMA to transfer plasmid to various cell lines. Since then it has been the most widely studied non-viral transfection delivery system. Some trials against EBOLA have been recently performed with positive results [38]. Generally the idea relies on the electrostatic interaction between positively charged liposomes made of cationic lipids and negatively

charged DNA or RNA strands. Nucleic acid trapped within the formed complex (called lipoplex) is compacted and protected from unfavorable physiological conditions. Due to the adjusted DNA – liposome ratio, the lipoplex has overall positive charge. Positively charged vesicles associate with a negatively charged cell membrane due to the electrostatic interactions. Then, dependent on the cell type and lipoplex size, they are up-taken by several possible pathways as phagocythosis, clathrin- and caveolae-mediated endocytosis or macropinocythosis [39]. The general picture of a lipid-mediated transfection mechanism is shown in Fig. 1
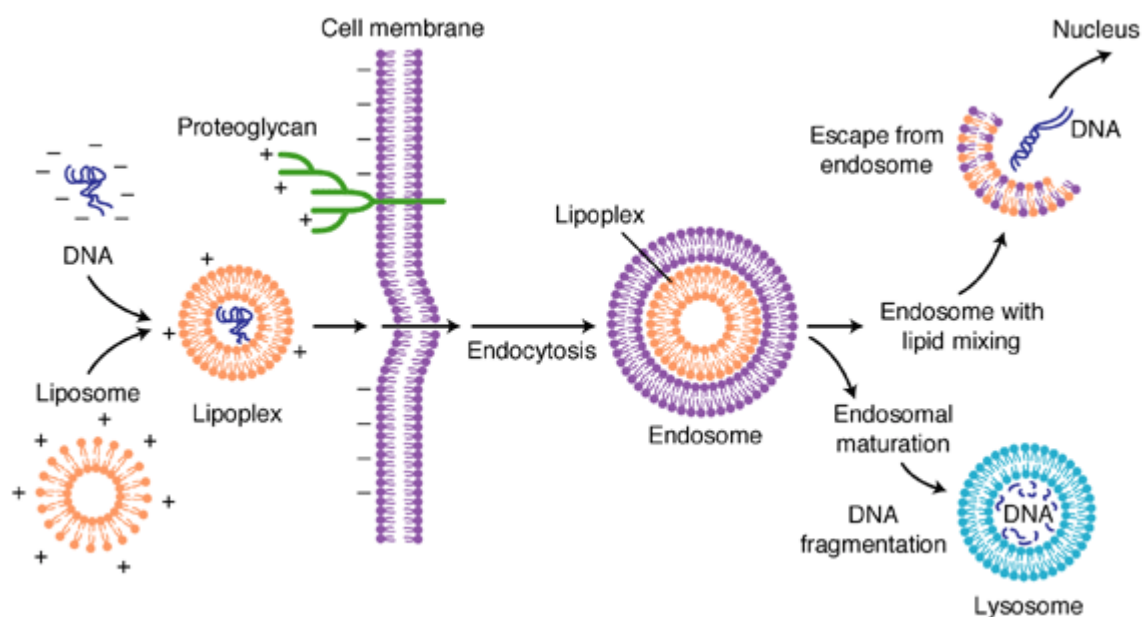

Fig. 1 Schematic representation of lipid mediated transfection. Adapted from [42].

One of the crucial steps for transfection efficiency is the load escape from the endosome before its fusion with lysosome and lysis by enzymes. For that, the endosome membrane has to be destabilized. There are several ways of endosome membrane disruption. The first is by fusion with other membrane that has tendencies to non-lamellar structure formation (micellar, hexagonal or cubic). Addition of, for example, DOPE that forms hexagonal phase at low pH (pH in an endosome is mildly acidic) helps in the membrane destabilization and load escape. Also the charge is important not only for a lipoplex attachment to the cell, but as well for the second escape way - by swelling. Buffering action of some compounds like lipids or polymers (e.g. PEI) causes proton pumping into endosome after a sudden drop of pH in it, what results in an increase of osmotic

pressure due to water entry and endosome collapse [40]. The other suggested mechanism is the swelling due to the protonation and electrostatic repulsion of pH-sensitive lipids or polymers which also leads to endosome disintegration [19]. After cargo escape from the endosome, it has to be delivered to its destination: siRNa to cytosol and DNA to a cell nucleus. The transport is by diffusion and its pace depends on the lipoplex size. Intracellular matrix can either slow it down or guide the vesicles inside the cell. The effective entrance to the nucleus is possible only when the nucleus membrane is disrupted during mitosis [41]. For that reason the cell division rate is also very important for the given gene expression. The passive transport of DNA through nucleus membrane pores is also possible but this way is very ineffective. Once in nucleus, DNA has to be expressed. At this point, the efficient expression depends on the delivered DNA sequence design.

As mentioned above, the morphology of the lipoplex plays a huge role in the transfection process. The factors that may influence its performance have been described below.

3. CATIONIC LIPIDS

Liposomal carriers are used not only as gene delivery systems but also as vectors of peptides, proteins and other drugs for pharmaceutical as well as cosmetic purpose. Ease in controlling their biophysical properties made them ideal vehicles for versatile applications. By optimizing the composition, liposomes may be designed for individual needs of size, charge, colloidal properties, fluidity, phase transitions and formulation structure. Precise analysis of the properties of a single lipid and made of it liposome helps understanding and predicting the system behavior in physiological conditions and choosing the right formulations for a given drug [43-45].

3.1 LIPID MOLECULE STRUCTURE

A lipid structure has a huge influence on its physical-chemical properties like phase behavior, general fluidity, polymorphism or polarity and biological relevance like toxicity or biodegradability. Also other properties, such as chemical stability enabling long storage is of critical importance for pharmaceuticals. The molecule shape influences the shape of liposomes and this way the lipoplex affects transfection efficiency. Most lipids used for gene delivery are inspired by biological membrane lipids. The most

common are DOTAP, DOTMA, DODAC, DOSPA, DOGS, DC-Chol and many others. But intensive research is being done on the design of molecules that could transfer genes into cells with minimal toxic effect and maximal efficacy. Generally, cationic lipids used for gene transfection consist of a hydrophobic part, a hydrophilic headgroup and the linker between those two (Fig. 2). Sometimes also a backbone that acts as a scaffold can be identified. Some liposomes are additionally equipped with a targeting moiety that enables specific delivery.
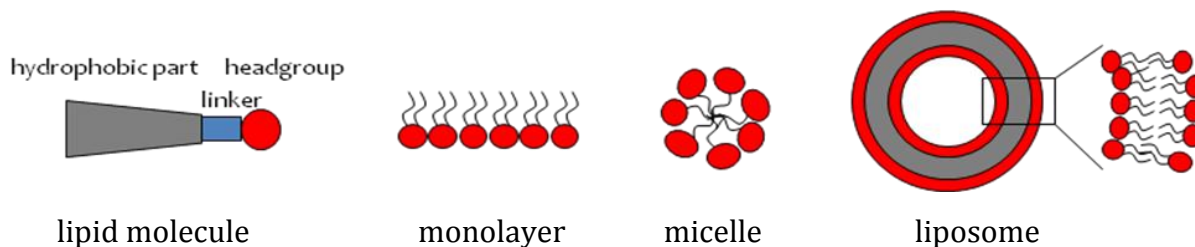

Fig. 2 Schematic representation of a lipid molecule and structures formed by lipids.

3.1.1 Hydrophobic domain

The hydrophobic domain is either a long hydrophobic chain or a cholesterol derivative. If the molecule comprises acyl chains in the hydrophobic part, then usually two, but also one or three chain lipids have been investigated. The hydrocarbon chains are 12- 18 carbons long and are not necessarily symmetrical. Generally molecules with one or two double bonds give better transfection efficacies than their analogues with saturated chains. *Cis-* as well as *trans*-isomers were tested but no pronounced tendency in their efficiency has been found thus far [46,47].

3.1.2 Headgroup domain

The hydrophilic headgroup is positively charged due to the presence of primary, secondary or quaternary amines. Also, guanidine and imidazole moieties have been investigated. Thanks to those groups the charge of the molecule is pH dependent and can be easily controlled. The headgroup region plays a crucial role in DNA binding and compacting and assures the overall positive charge of a lipoplex that enables its cellular up-take [48].

3.1.3 Backbone

The backbone is a scaffold of the molecule on which the headgroup and chains are fixed. Some molecules do not have it and the hydrophobic and a hydrophilic part are connected with each other only via a linker bond. Most commonly used backbone is glycerol-based but also amino-acids, aromatic groups, phosphonates and other structures have also been tested[49,50].

3.1.4 Linker bonds

If the molecule possesses the backbone, two linker bonds are present: between a tail and a backbone and backbone and a headgroup. Otherwise, the linker bond connects directly a headgroup with a tail. The two most important features of these bonds are their biodegradability and chemical stability. They also define the relative orientation of hydrophilic and hydrophobic domain and control the conformational flexibility. Esters and ethers bonds are of common use. Ethers (e.g. DOTMA) are more chemically stable but, in contrast, esters (e.g. DOTAP) can be easier hydrolyzed which reduces the lipid toxicity. Apart from these two carbamates, amides, carbonates, phosphonates and other bonds have been used [50].

The lipid structure has great influence on system efficiency. As shown by many studies, only a small difference in the molecule chemical structure can drastically change the system transfection efficacy. In this research the influence of the headgroup and the hydrocarbon tail structure is investigated and the meaning of those two molecular elements is described in detail later in the text.

3.2 LIPIDS IN BULK

Liposomes are the most efficient non-viral DNA carriers developed to date. Liposomes are small particles made of lipids, formed by one or more lipid bilayers. They are formed spontaneously when the lipid film is hydrated. Lipid molecules are amphiphiles. They have hydrophilic and hydrophobic parts so in contact with water they organize in tail-to-tail and head-to-water structures. After full hydration most of lipids form single- or multilamellar spherical liposomes, but other structures such as hexagonal (H_I), inverted hexagonal (H_{II}) and cubic (Q) are also known. As with monolayers, bulk systems also

exist as gel and fluid phases and can undergo temperature induced phase transition.

The structure of hydrated liposomes depends strongly on the lipid molecule architecture and can be predicted by a packing parameter, *P*. *P* is given by: *P= v/al* where *v* is the volume of the hydrophobic region, *l* is the length of the acyl chain and *a* is the area of a headgroup region. P higher than one means that the headgroup region is smaller than the hydrophobic region and the lipid aggregate will tend to form inverted hexagonal or cubic phases. If P is smaller than ½ then micelles are the most probable aggregate structure. All P values between ½ and 1 will result in cylinder-like lipid molecule shape and multilamellar membranes. The *P/* lipid membrane structure dependence has been shown in Fig. 3 [51-53].
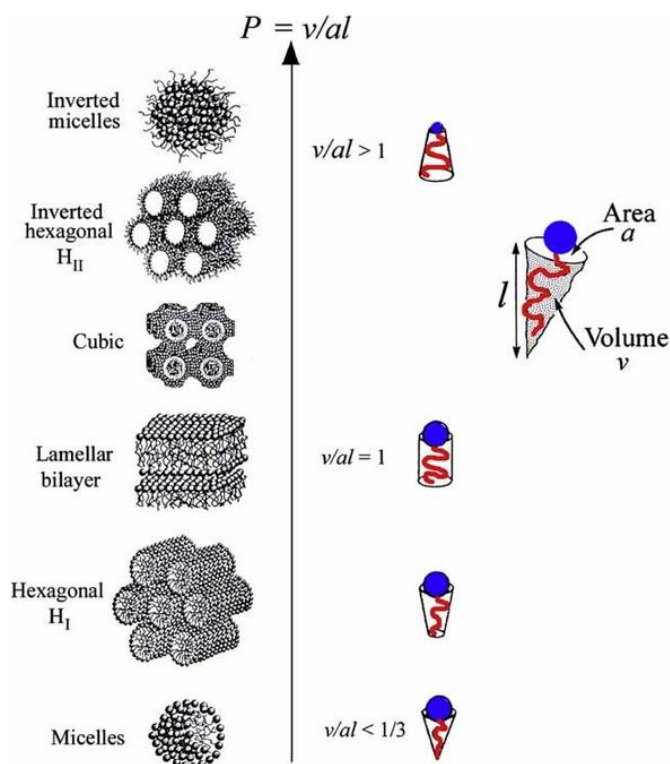
Fig. 3 Preferred lipid aggregate structures in dependence on the packing parameter P. Adapted from[53].

3.2.1 Polymorphism of lipid aggregates (lipid water suspensions)

As mentioned above, there are several structures that single lipid components can display in water. This depends on lipid geometry but also on other factors like the content of water, temperature or ionic strength of a dispersion solution. The same lipid can therefore form many different phases upon varying conditions. It is contingent upon

inter- and intramolecular interactions, like hydrophobic interactions between hydrocarbon chains or hydrogen bonds within headgroup region. The phase can be identified by X-ray scattering methods. Cryo-TEM can provide complementary information and help in phase recognition. Wide angle X-ray scattering (WAXS) gives information about the chains order in the membrane and allow the fluid and gel phase distinction. Small X-ray scattering (SAXS) shows the symmetry of lipid layers and enables lipid phase identification. All structures are characterized by given Bragg peak ratios in SAXS region that are described below. The SAXS and WAXS principles are explained in chapter 4.5. The three most common groups of lipid membrane shapes are lamellar, hexagonal and cubic. Each of them can be described by d that defines the repeat distance, which in this case is the thickness of the lipid bilayer with a hydration layer of water. Cubic and hexagonal phases have also their characteristic lattice constant a that describes the macro repeat unit of the phase [54].

3.2.1.1 Lamellar phase

The lamellar phase is formed by lipids of more or less cylindrical shape. It is characterized by Bragg peak ratios of 1: 2: 3 etc. The lipid molecules organize in back to back conformation in a sandwich like structure, where a certain amount of water, usually a layer of 8 – 16 Å, is trapped between the bilayers. The amount of water depends mainly on the temperature and polarity and charge of headgroups. The possible lamellar phases have been shown in Fig. 4 [55]
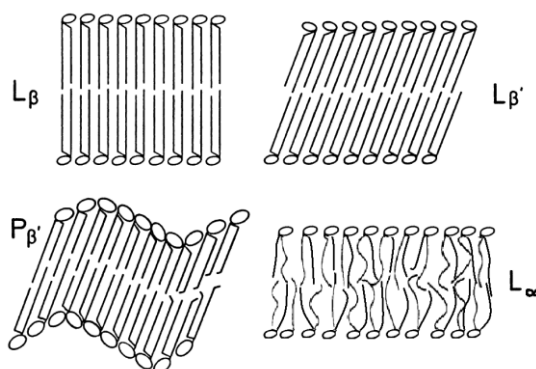

Fig. 4 Possible lamellar phases, L_β – untilted gel, $L_{\beta'}$ – tilted gel, $P_{\beta'}$ – ripple, L_α – fluid. Adapted from [56].

The lamellar phase is characterized by the parameter *d* that describes the thickness of the double layer with a hydration layer in between. At lower temperatures many lipid chains are ordered in *all-trans* conformation with crossectional area of ~20 Å^2 that indicates chain free rotations. The headgroups are usually disordered but can be ordered by intermolecular interaction like hydrogen bonds. The two most common gel lamellar phases are L$_\beta$ and L$_{\beta'}$, with untilted and tilted chains, respectively. Upon heating, layers of some lipids deform by periodical modulation and P$_{\beta'}$, ripple phase, is formed. In this phase the chains are still in *all-trans* conformation and tilted. Further heating causes chain melting (which practically means that they loose order) and the area per chain increases by 15 – 30 %. The melting is usually assisted by an increase of water content between layers. The lamellar fluid phase, L$_\alpha$, is formed (Fig. 4). The temperature at which the melting appears is called the transition temperature and can be detected by a sudden change of Bragg peak positions or by DSC.

3.2.1.2 Hexagonal phase

The hexagonal phase has 2D symmetry and is formed by fluid aggregates shaped in long cylinders that have either the hydrophilic headgroups oriented to the inside of the cylinder which is filled with water (inverse hexagonal, H$_{II}$) or that look more like the elongated micelles with chains pointing to the center (normal hexagonal, H$_I$) (Fig. 3). For diacyl lipids, the H$_{II}$ is more common (for example DOPE) while H$_I$ is often formed by one chain amphiphiles. Both phases are characterized by SAXS reflexions in a ratio of 1: $\sqrt{3}$: 2: $\sqrt{7}$: 3 etc. Apart from *d* spacing, the phase can be described by the *a* parameter which describes the distance between rods [57]. *a* and *d* are related by:

$$d_{hk} = \frac{\sqrt{3}a}{2\sqrt{(h^2 + k^2 - 2hk)}}$$

eq.1

Where *h, k* are Miller indices.

3.2.1.3 Cubic phase

Cubic phases are the largest family of fluid 3D phases, thus far there are only several well characterized types but much more than that have been detected. They generally divide into two types: biocontinuous, where both water and lipid components are continous, and micellar which is formed by densely packed micellar aggregates. Both

types may be normal or inverse. Their general structure is based on the three-dimensional network of connected rods. For cubic phases, the repeating distance, *d*, is related to the lattice constant, *a,* by:

$$d_{hkl} = \frac{a}{\sqrt{h^2 + k^2 + l^2}}$$

eq.2

where *h, k, l* are Miller indices of planes.

Biocontinuous phases are described by covered by bilayers minimal surface theory and can be divided into: gyroid (G), diamond (D) and primitive (P) phases (Fig. 5) [58,59].

Fig. 5 Biocontinious cubic phases. The green structures show water channels in the lipid aggregate and the blue ones minimal surfaces of each of phases. Figures A corresponds to Ia3d, B to Pn3m and C to Im3m structure. The figure adapted from [58] and [62].

Cubic phases can be also illustrated on the following Bravais lattices: primitive (P), body-centered (I) and face-centered (F) (Fig. 6) [60,61].

Fig. 6 Space groups P, F and I of cubic phases. Adapted from [60].

The well described biocontinuous cubic phases are listed below. Three of them are also shown in Fig. 5. For details see [60].

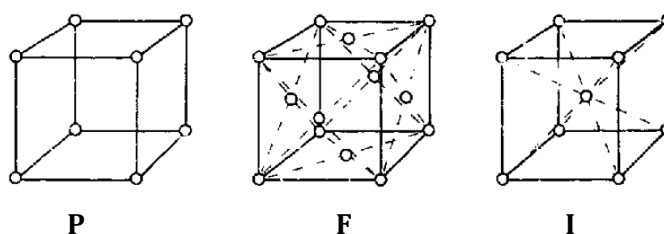*Ia3d.* This was the first cubic lipid structure that was unambiguously identified [63]. It is a body centered structure with gyroid type of minimal surface and to date the most commonly observed cubic structure formed by lipids, usually located between L_α and H_{II} and between L_α and H_I phases in the phase diagram. It is a body-centered space group that is characterized by X-ray reflexes with spacing ratio of $\sqrt{3}$: $\sqrt{4}$: $\sqrt{7}$: $\sqrt{8}$: $\sqrt{10}$: $\sqrt{11}$ etc.

Pn3m. This is a primitive cubic lattice characterized by SAXS spacing ratios of $\sqrt{2}$: $\sqrt{3}$: $\sqrt{4}$: $\sqrt{6}$: $\sqrt{8}$: $\sqrt{9}$ etc. It has been first described by A. Tardieu in her PhD thesis in 1970. Now it is recognized as a phase of diamond type minimal surface (D).

Pm3n. It is a primitive cubic lattice with Bragg peak ratios in SAXS region of $\sqrt{2}$: $\sqrt{4}$: $\sqrt{5}$: $\sqrt{6}$: $\sqrt{8}$ etc. It is usually located between micellar aqueous solution and H_I phase and is formed by closely packed rod-like micelles. It appears for high water contents and may be difficult to identify due to the small number of visible reflexes [64].

Im3m. The phase is described by the primitive (P) type of a minimal surface and body centered Bravais lattice (P). The Bragg reflexes are expected at ratios $\sqrt{2}$: $\sqrt{4}$: $\sqrt{6}$: $\sqrt{8}$: $\sqrt{10}$: $\sqrt{12}$: $\sqrt{14}$ etc.

3.3 LIPOLEXES

Lipoplexes morphologies as well as their other properties like charge or the molecular characteristic of cationic and helper lipids used for their formation have a great influence on the transfection efficiency. Also some practical requirements which are essential from the pharmaceutical point of view, like long-term stability for storage and in physiological conditions, must be met. The most important factors have been described below.

3.3.1 Structure

When the negatively charged nucleic acid is added to a cationic liposome dispersion, it attaches to the positively charged headgroups and induces liposomes fusion and rearrangement. The complexation is driven electrostatically. In most of the cases fluid sandwich-like (bilayer – DNA – bilayer) multilayer structures are formed (L_α). It has

been reported many times, that DNA strands can order within the complex into parallel rods with a defined spacing [65]. If the lipid aggregate to a hexagonal or cubic phase then DNA possesses spaces in which water is trapped and the whole system adopts structures related to the one without DNA [65,66]. Cubic phases though are very rarely observed. Some of possible structures are shown in Fig. 7. To date, non-lamellar phases are believed to give better transfection results due to better fusogenic properties with a cell and endosome membranes. They are also responsible for an endosome destabilization and nucleic cargo escape. Lamellar phases tend to remain stable in contact with negatively charged membranes [67]. But some authors also reported, that it does not necessarily improve the transfection rates but even makes it less effective [68].
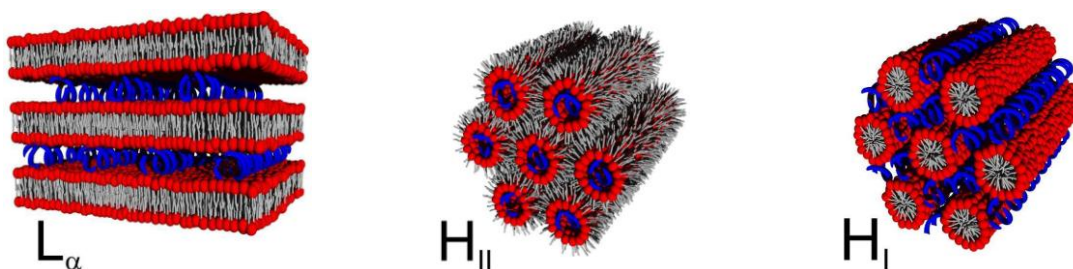

Fig. 7 Schematic representations of the phases of lipid-DNA complexes: complexed lamellar L_α, complexed inverted hexagonal H_{II}, and complexed micellar hexagonal H_I. The headgroups of lipid are in red, their chains in grey and the DNA rods are in blue. Adapted from [54]

3.3.2 Lipid to DNA ratio and zeta potential

The overall lipoplex charge density is controlled by its components ratios (cationic lipids, negatively charged nucleic acid and neutral helper lipid) and can be indirectly determined by zeta potential measurements of a vesicle surface charge. Zeta potential (ζ-potential) is a function of lipoplex structure and its composition. Since the attachment of lipoplexes to the negatively charged cell membranes is driven electrostaticaly, the lipoplex charge must remain positive. Fluid lamellar lipoplexes with too low membrane charge density have smaller tendencies to bind to the cell and were found to trap DNA and prevent its release into the cytosol. In contrast, high charge of lipoplexes seem to induce membranes fusion and DNA escape. The universal curve for the dependency between charge density of L_α lipoplexes and their transfection performance has been constructed and shows an exponential growth of efficacy with increasing charge up to the optimal value that equals efficiencies obtained for H_{II} complexes [69].

3.3.3 Helper lipid

Helper neutral lipids are added to cationic lipids to tune the liposomes/lipoplexes charge or structure [70]. DOPE (Fig. 48) is the most commonly used co-lipid. It has no charge and forms inverted hexagonal phase (H_{II}) in aqueous solutions. It is believed to improve transfection efficacies of cationic lipid systems by triggering the membranes fusion and endosome disintegration. Added to a lipid forming lamellar phase up to ~50% in physiological conditions, DOPE is fully integrated in the lamellar structure, but at low pH of the endosome it converts to inverted hexagonal phase and destabilizes the endosome enabling endosomal escape of a lipoplex load [71]. The second co-lipid that is often employed is cholesterol (Fig. 27). It was chosen due to its biocompatibility. It is one of the main cell membrane lipids, and lipoplexes containing high quantities are not recognized by body defense system as targets to degradation [72].

3.3.4 Size

The most commonly used formulations are 100 to 1000 nm big. It has been reported before that the increase of the lipid to DNA ratio increases the lipoplex size and heterogeneity. The optimal size of a lipoplex for the efficient transfection depends on the type of a target cell, the way of introduction to the cell or body and the experiment mode (*in-vivo* or *in-vitro*). There are no general-purpose rules, though, and the reports often stand in contradiction. However, the size of lipoplex definitely determines its post administration behavior and its entry pathway to the cell [73]. When administrated intravenously, large aggregates tend to accumulate in the lung capillaries which is desired when the liposomes are targeted to the pulmonary epithelium and can be an obstacle when they bring a risk of blockage. Cancer cells can be treated with very small vesicles that may enter through cancer cell specific gaps in the endothelium [50]. There is no doubt, that the size analysis is needed to determine the right lipofection system for a treatment of interest.

3.3.5 Stability

The stability of lipoplexes in terms of colloidal and chemical properties is important for long-term storage and administration process. The liposomes carrying nucleic acid cargo should remain unchanged (by means of particle size and load content) upon ionic

strength change or dilution which take place while entering the environment of a body. According to the DLVO theory (Derjaguin-Landau-Verwey-Overbeek), the colloidal system is stable if the repulsion between particles is higher than their van der Waals attraction which in practice is observed for systems with ζ-potential > +/-30 mV. Also the chemical inertness, especially between components of multicomponent systems, is of high importance. The helper lipid DOPE was reported to react with unprotonated amines of cationic lipids headgroups [74]. This kind of interactions has to be also taken into account when designing new formulation.

4. METHODS AND BASIC CONCEPT OF THEIR APPLICATION

4.1 LANGMUIR FILM MICROBALANCE

Langmuir film microbalance is a simple method to examine amphiphiles monolayers at the air-water interface. By the measurement of the surface pressure the phase state of the monolayer can be investigated and phase transitions detected. It is also an ideal model system for biological membranes. It allows easy adjustment of the lipid membrane content and charge as well as environmental experimental conditions like pH, ionic strength, temperature etc. Also the interaction of biological species with lipid monolayer can be checked easily by addition of given species to the subphase.

The technique allows to measure the surface pressure (π) being a difference of the surface tension of water (σ_{H2O}) and the film covered surface (σ_{film}).

$$\pi = \sigma_{H2O} - \sigma_{film} \hspace{4cm} eq.3$$

The setup consist of a teflon trough equipped with Wilhelmy plate connected to an electronic pressure sensor and a movable barrier allowing compression of the monolayer. The Langmuir monolayer of an insoluble compound is spread onto the water surface from an organic solvent solution. After the solvent is evaporated, the amphiphiles organize according to their hydrophilic-hydrophobic nature (hydrophilic part is immersed in water, while hydrophobic is facing air). A schematic representation of a set-up is shown in Fig. 8.
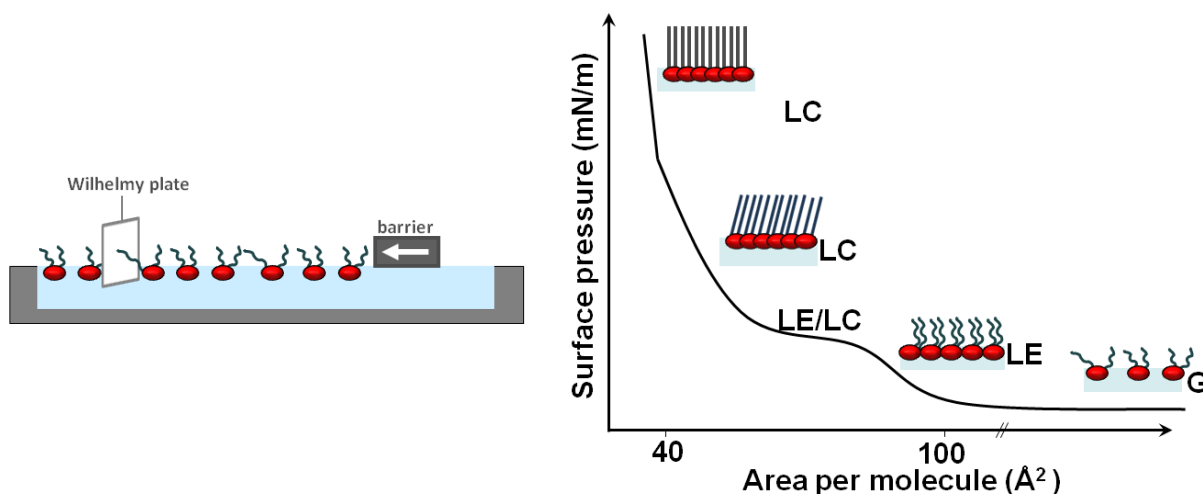
Fig. 8 Schematic representation of Langmuir trough (left panel) and an example Langmuir compression isotherm (right panel) with phase states: G – gaseous, LE – liquid expanded, LC – liquid condensed.

In this experiment lipid monolayers have been investigated. Fig. 8 shows a typical behavior of lipid monolayer along the compression isotherm. At large areas per molecule there are no interactions between molecules and they are in the gaseous-like state (G). Upon compression, they come closer together and start interacting forming the liquid-expanded phase (LE). Decrease of the area per molecule leads to a continuous increase of surface pressure. Further the lipid monolayer undergoes the structural change from *gauche* (LE) to *all-trans* conformers (LC) called the first order phase transition indicated by a characteristic plateau. Above the phase transition pressure (π_{tr}) the acyl chains order in a crystalline-like structure thanks to strong hydrophobic interactions and the liquid condensed phase (LC) is formed. The chains can be tilted or upright. Some lipids (or other long acyl chain molecules) can undergo the second order phase transition from the tilted to the untilted state which is indicated by a characteristic kink in the isotherm. At high pressure the lipid monolayer collapses and bilayers and other bulk structures (like liposomes) are formed.

This work focuses on cationic lipid monolayers spread at subphases of different temperature and pH values. Also the influence of the DNA presence in the subphase on the lipid monolayer structure has been investigated.

4.2   INFRARED REFLECTION-ABSORPTION SPECTROSCOPY

Infrared reflection-absorption spectroscopy (IRRAS) is a powerful method to investigate thin layers, especially at the air – water interface. Combined with the film balance, it can serve as a surface sensitive technique to investigate the structure of amphiphiles monolayers. The method provides information about the conformation and the orientation of amphiphiles as well as about hydrogen bonding and ionic interactions between molecules. It has been also widely used to determine proteins secondary structure. In this research it has been used to study lipid monolayers at the air-water interface.

For an experiment, the IR-beam of a Fast-Fourier-Transform IR-Spectrometer is focused at the air-water interface. IR light excites vibrational transitions in the molecules at the interface. The final spectrum is given as a reflectance absorbance as function of the wavenumber (wavenumber = $1/\lambda$).
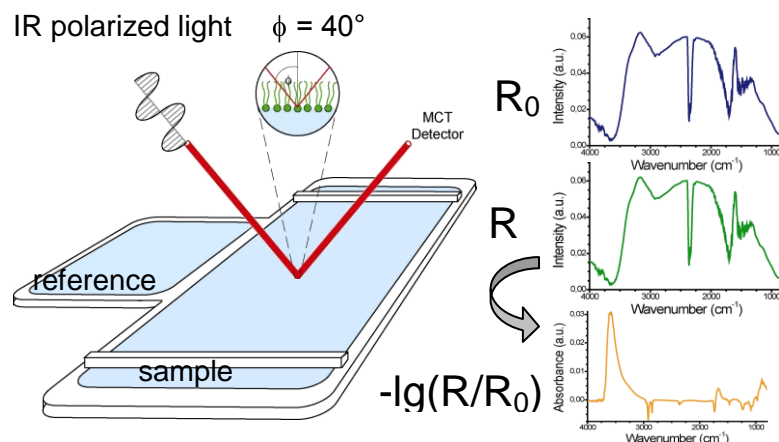

Fig. 9 Scheme of IRRAS setup: R_0 is a subphase reflectance, R is a sample reflectance and RA = -lg(R/R_0) is the final spectra; Φ is an incident angle; lipids are marked green.

Example spectra are shown in Fig. 10. The vibration frequencies are accompanied by changing molecular dipole moments and are sensitive to the molecule conformation. When parallel (*p*) and perpendicular (*s*) polarized light is used, also the orientation of molecular dipole moments can be detected and evaluated. The angle of the incident beam can be varied. The light penetration depth is equal few μm and is large enough to excite entire lipid molecule and some subphase underneath. To eliminate the signal of water from the subphase and water vapor in the optical path in the spectra, the sample reflectance *(R)* is corrected with the reflectance of the subphase (*R_0)* and the reflection

absorption spectrum $RA = -lg(R/R_0)$ is obtained For water signal elimination, the shuttle technique between two troughs is employed: the sample trough, where the sample is spread on the water/buffer surface and the reference trough filled with the pure subphase. To control the surface pressure of amphiphiles, the sample trough is equipped with two movable barriers and a Wilhelmy plate (Fig. 9) [75].
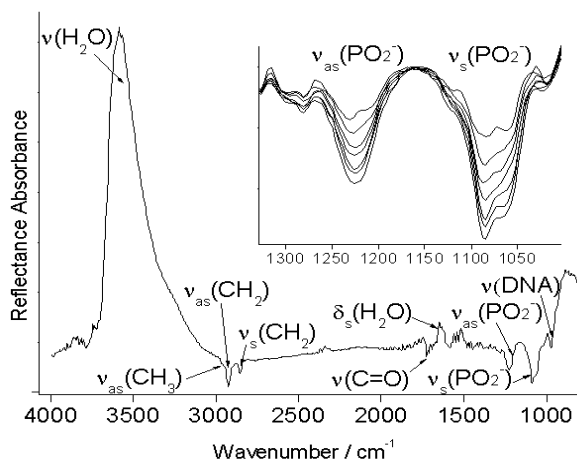

Fig. 10 IRRA spectra with magnified region of symmetric, ν_s (PO2), and asymmetric, ν_{as} (PO2), phosphate diester bands used for the quantification of DNA coupled to the lipid monolayer.
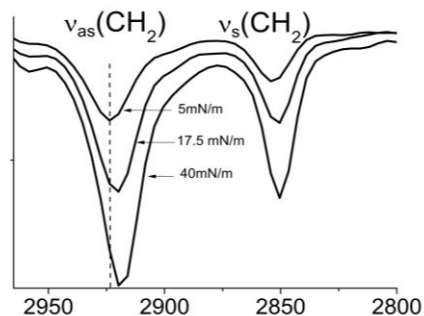
Fig. 11 The shift of CH$_2$ symmetric, ν_s (CH$_2$), and asymmetric, ν_{as} (CH$_2$), stretching vibration bands while LE/LC phase transition (IRRAS).

The structural information about lipid molecules (in the experiments described later cationic lipids are used) that can be obtained from IRRA spectra are summarized in Table 1 [76].

In this study, the conformation and orientation of lipid molecules spread at the air-water interface have been investigated (by defining the position of ν_{as}(CH$_2$) bands (Fig. 11 and Table 1). Also the adsorption of DNA present in the subphase to lipid monolayers was checked and the trial of DNA quantification was done. For all experiments both, s- and p-polarized light was used. The angle of the incident beam was adjusted at 40°.

Table 1 Positions of selected IR absorption bands characteristic for lipids and water [76].

Assignment	Wavenumber/ cm^{-1}	Structural meaning
H$_2$O		
ν_{as} (O-H)	≈ 3490	
ν_s (O-H)	≈ 3280	
δ (H$_2$O)	1645	
Lipids		
ν_s (CH$_3$)	2870	
ν_{as} (CH$_3$)	2956	
ν_{as} (CH$_2$)	2920	*all-trans* (condense phase)
	2924	*gauche* conformation (fluid phase)
ν_s (CH$_2$)	2849	*all-trans* (condense phase)
	2853	*gauche conformation* (fluid phase)
ν (C=O)	1730	
δ^c (CH$_2$)	1473	triclinic
δ^c (CH$_2$)	1468	hexagonal
δ^c (CH$_2$)	1472 and 1463	orthorhombic

ν_{as} - asymmetric stretching; ν_s - symmetric stretching; δ – bending; δ^c- scissoring

4.3   GRAZING INCIDENCE X-RAY DIFFRACTION (GIXD)

GIXD is a highly sophisticated method that allows detailed analysis of Langmuir films of long amphiphilic molecules. While Langmuir microbalance and IRRAS are used for macroscopic analysis of monolayers at the air-water interface, GIXD can deliver information about the dimensions of a unit cell of the lattice formed by condensed aliphatic chains, its distortion and chains tilt as well as the chain cross-sectional area [77-80].

The principal of the technique bases on the total reflexion phenomena. The X-ray beam hits the monolayer deposited at the air-water interface at the angle smaller than the total reflexion angle (for the monolayer/air medium equal $\alpha_c \sim 0.1^o$). The depth of the subphase penetration is very low (8 nm) and the X-rays travel as an evanescent wave on the monolayer. This way, the scattering of the subphase that is in a huge excess to the monolayer, is negligible. The schematic representation of diffraction geometry is shown in Fig. 12.
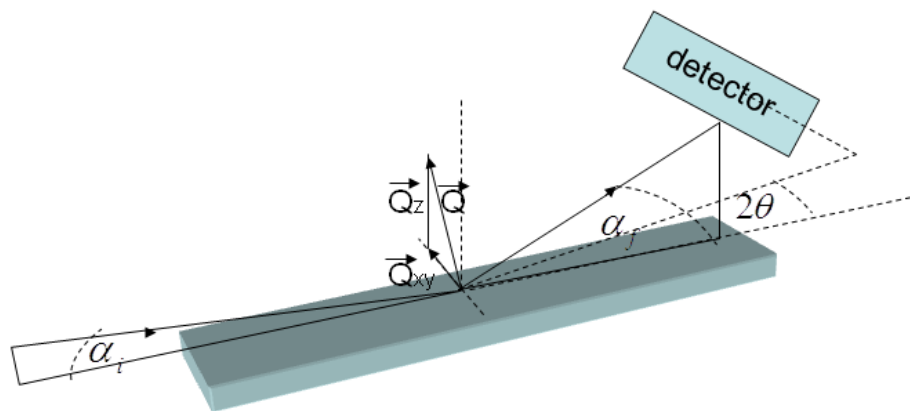
Fig. 12 Schematic representation of GIXD set-up and geometry of grazing-incidence diffraction.

A condensed Langmuir film is a pseudo crystalline structure formed by randomly oriented 2-D domains what in consequence gives a structure of a 2D powder. Any in-plane periodicity in the molecules positions gives rise to scattering intensity but since the orientation of powder domains is random, the diffraction is always averaged over all "crystals". The diffraction pattern is measured in dependence on three angles: the incident beam α_i, the vertical scattering angle α_f, and the scattering angle with respect to the subphase plane 2θ (horizontal) (Fig. 12). The scattering vector Q is composed of the in-plane (horizontal) component Q_{xy} and out-of-plane (vertical) component Q_z which are given by:

$$Q_{xy} = \frac{2\pi}{\lambda}\sqrt{\cos^2\alpha_i + \cos^2\alpha_f - 2\cos\alpha_i \cos\alpha_f \cos2\theta} \approx \frac{4\pi}{\lambda}\sin\theta \qquad \text{eq.4}$$

$$Q_z = \frac{2\pi}{\lambda}(\sin\alpha_i + \sin\alpha_f) \approx \frac{2\pi}{\lambda}\sin\alpha_f \qquad \text{eq.5}$$

where λ is the X-ray radiation wavelength.

The maximum of the intensity peak of the in plane component can be related to the lattice spacing parameter d:

$$Q_{xy} \approx \frac{4\pi}{\lambda}\sin\theta_{max} = \frac{2\pi}{d_{hk}} \qquad \text{eq.6}$$

The h and k are Miller indices used for reflexes indexing. The lattice parameter allows calculation of lattice unit cell dimensions (a, b, c) and angles between them (α, β, γ). Additionally the distortion of the elementary unit cell and the tilt angle t of aliphatic chains can be calculated. Those values allow to calculate the molecular in-plane area A_{xy} and the chain cross-section area A_o:

$$A_{xy} = \frac{a \cdot b \cdot \sin\gamma}{n}$$ eq.7

$$A_o = A_{xy} \cos t$$ eq.8

Where n is the number of molecules/chains in an elementary cell.

Full width at half maximum (FWHM) of the Bragg peak (Q_{xy}) can be used to define the finite size of the 2D crystals, called correlation length L_{xy}, and by the FWHM of the Bragg rod (Q_z) the length of the chain forming the layer L_z can be determine. To calculate the two lengths Scherrer formula is used:

$$L_{xy} = 0.88(2\pi / FWHM_{Q_{xy}})$$ eq.9

$$L_z = 0.88(2\pi / FWHM_{Q_z})$$ eq.10

In this experiment GIXD was used for the determination of the LC structure of monolayers of diverse lipids spread on water and buffers of different pHs, at various temperatures and surface pressures. The detailed analysis of GIXD patterns of lipids showed discrete differences that influenced the divergence of their macroscopic properties.

4.4 BREWSTER ANGLE MICROSCOPY (BAM)

Brewster angle microscopy has been first introduced in 1991 [81]. It is a simple technique to observe thin films spread at the air/water interface. Due to the Brewster law, when the light beam passes the interface formed by media of different refractive indexes, some of light is reflected. But there is a specific angle of incidence, called Brewster angle (θ_B), that the light of p-polarization is zero:

tan $\theta_B = n_1/n_2$ eq.11

where n_1 and n_2 are refractive indexes of media forming the interface. For air ($n_1 = 1$) and water ($n_2 = 1.33$) interface, the Brewster angle equals to $\theta_B = 53°$.

The Brewster angle microscopy uses this law for thin films visualization. When the incident beam of p-polarized light heats the clean air/water interface under the Brewster angle, no reflection can be observed. The thin organic film spread on the interface will cause the reflection due to a different refractive index. The reflected light is used to form an image of contrast that can be recorded by a camera (see Fig. 13).
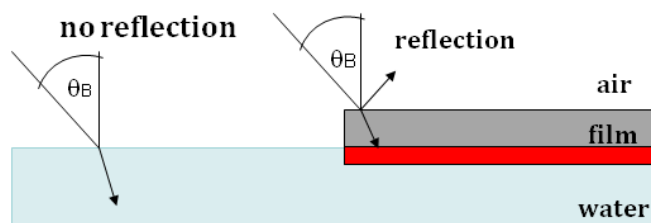
Fig. 13 Schematic representation of BAM.

In this work Brewster angle microscopy was used as a supporting method of the phase transition observation of cationic lipids films spread on the air/buffer interface.

4.5 SMALL- AND WIDE ANGLE X-RAY SCATTERING (SAXS/ WAXS)

Small and wide X-ray scattering are the most reliable methods for lipid phase identification. SAXS deliver information about long range ordering what can be translated to the global symmetry and architecture of lipid layers in lipid/water aggregates. If lipid layers are structured and show repeating distances, they give rise to the Bragg peaks in ratios characteristic to the type of phase. Moreover, when aliphatic chains within the layers are ordered (short range organization) then reflections in the wide angle region (WAXS) appear. Scattering data are represented usually as scattered intensity *I* versus the reciprocal spacings $s_{hkl}=1/d_{hkl}$, where *h, k* and *l* are Miller indices. The scattering intensity results from structure factor *S (q)* related to the "crystalline" lattice and form factor *F(q)* coming from the electron density profile of the layer and is given by:

$$I(q) = \frac{S(q)|F(q)|^2}{q^2}$$

eq.12

where $q = 4\pi sin(\theta)/\lambda$ is the scattering vector, λ is the wavelength of X-ray radiation and 2θ is the scattering angle. Knowing the maximum of Bragg peaks, the *d* value (thickness of the double layer with hydration layer) can be obtained in analogues way to GIXD (*d = $2\pi/q$*) [82-84]. The schematic representation of SAXS experiment is presented in Fig. 14.
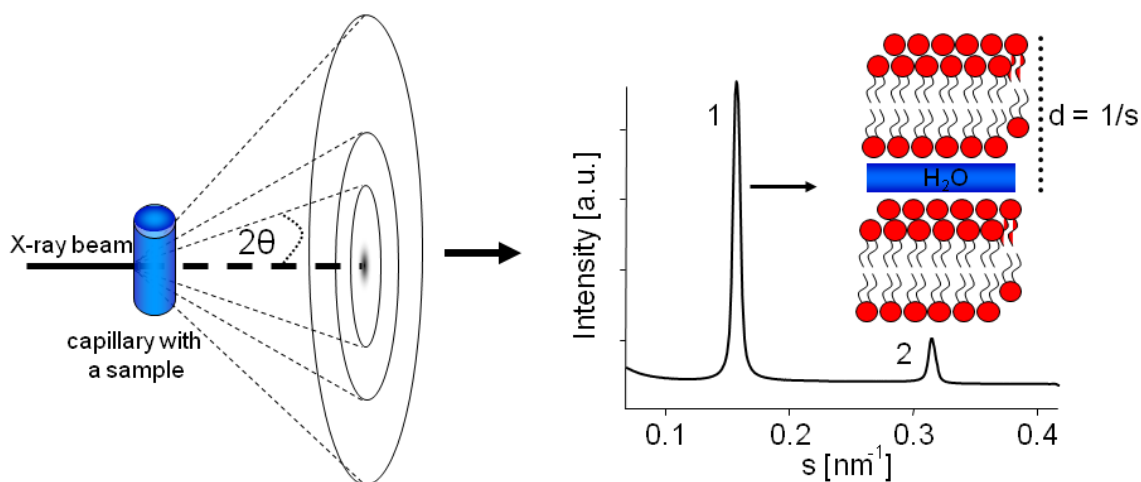
Fig. 14 Schematic representation of SAXS experiment (left panel) and its result – reflections characteristic for multilamellar structure (right panel). Adapted from [85].

Positions of the reflexes give direct information about the lipid phase structure. If reflections are found at ratios of 1: 2: 3: 4... they indicate a lamellar phase (L). Ratios of 1: $\sqrt{3}$: 2: $\sqrt{7}$... point to a hexagonal phase (H) with the lattice parameter describing the distance between rods equal to $a=2d_{10}/\sqrt{3}$. There is also a variety of cubic phases (Q), from which the most common are: primitive/simple (1: $\sqrt{2}$: $\sqrt{3}$: 2: $\sqrt{5}$...), face-centered ($\sqrt{3}$: 2: $\sqrt{8}$: $\sqrt{11}$...) and body-centered ($\sqrt{2}$: 2: $\sqrt{6}$: $\sqrt{8}$...). For details see Lindblom et. al. 1992 [86]. Moreover, the structures of phases and their relation with the symmetry of the single molecule have been described earlier in the text. SAXS enables also a fast phase transition temperature determination. The temperature scan allows pointing out the temperature at which the reflex positions describing the structure suddenly change due to melting or reorganization.

Below the phase transition temperature lipids in fully hydrated layers are in the gel phase. The chains are assumed to be in *all-trans* configuration and are ordered in a lattice comparable to the one observed by GIXD in monolayers. This organization can be detected by WAXS. For the detailed descriptions of existing structures see Marsh [87]. The structures of this research interest are L_{β} and $L_{\beta'}$ representing phases of untilted and tilted phases, respectively. L_{β} describes usually hexagonal packing characterized by one sharp Bragg peak in the WAXS region, $L_{\beta'}$ which is usually assigned to an orthorhombic unit cell, shows two peaks (s_{11} and s_{02}). The Bragg peaks positions allow calculating absolute area per chain and distortion of the unit cell. Above the transition temperature Bragg peaks disappear since fluid chains do not order and instead we can find a broad

halo in the whole WAXS region.

In this study SAXS and WAXS were used to determine the temperature dependent structures of cationic lipids dispersions in water and buffers of different pH values. Also mixes of lipids with helper lipids and DNA have been investigated. Moreover, the phase transition temperature of all systems was tracked and compared with data obtained from DSC.

4.6 DIFFERENTIAL SCANNING CALORYMETRY (DSC)

Differential scanning calorimetry (DSC) is a technique used to establish thermal properties of material. In the set-up the temperature of a sample (a solution of the molecule of interest) and a reference (only the solvent) is gradually changed. The difference in the amount of energy required to match the temperatures of both cells is measured as a function of temperature and time. The sample can either absorb or release excessive heat (in comparison to the reference) depending on the endo- or exothermic character of the transition that it undergoes. The measurement is usually presented as a curve of the heat-flow versus temperature or time. If the temperature increase induces any transition in the sample, it will be represented by a characteristic peak. The enthalpy change (ΔH) of the transition is then equal to the area under the peak (A) multiplied by the apparatus characteristic calorimetric constant (k):

$$\Delta H = kA \hspace{8cm} \text{eq.13}$$

The method is applied to determine various thermodynamic parameters of thermally induced changes in a sample. The basic one is the melting temperature (T_m). Also the glass transition, mixing processes or crystallization can be studied. DSC is also used to analyze various chemical reactions. The method is often applied for the construction of phase diagrams [88].

In this work, DSC was used for the determination of phase transition temperatures as a supporting method for SAXS/WAXS experiments. Also the homogeneity (mixing or demixing) of mixtures of cationic lipids with helper lipids and DNA has been investigated.

CHAPTER 1

THE INFLUENCE OF CHAIN PURITY ON THE PHYSICAL-CHEMICAL PROPERTIES AND TRANSFECTION EFFICIENCY

1. INTRODUCTION

The purity of the sample, understood as a defined composition, is one of the most important features of a potential drug. Nevertheless, many lipids that are perspective transfectants are synthesized from compounds of technical grade – often the only commercially available. The multicomponent character of the lipofectant system is known to improve transfection. Commonly used helper lipids mixed with the cationic lipid membrane improve the system lipofection efficacy by varying its structure, charge and fusogenic abilities. However, those are mixtures with designed composition. The situation changes, when one of the compounds used for the synthesis of a new lipid contains unknown substances. Recently, a novel class of cytofectines containing a malonic acid diamide backbone was described [89,90]. The most effective lipid of this class contains one oleyl chain. But due to the commercial accessibility and low cost, the oleylamine used as the chain precursor was of technical grade. Since oleyl chains are believed to improve transfection efficiency, the same precursor was used before by many groups worldwide [91-93]. Hence the question arose, how drastic is the impact of the alkyl chain purity on the transfection efficiency?

To study this problem I investigated the aforementioned most effective lipid of a new class as two samples. For the first, lipid **8**, the commercially available oleylamine was used as oleyl chain precursor. The second, lipid **8p**, was produced of self-synthesized oleylamine of analytical purity. In this study, the physical-chemical properties and transfection activities of both chemically the same lipid samples (N'-2-[(2,6-diamino-1-oxohexyl)amino]ethyl-2-hexadecyl-N-[(*9Z*)-octadec-9-enyl] propane diamide) differing in purity are compared (Fig. 15). Since lipid **8** has been already described earlier [23,24], this work will focus on the physical-chemical behavior of lipid **8p** and the differences between the two samples. The main aim is to screen the impact of only chain purity on the phase behavior and transfection rates. It is believed that cationic lipids with

unsaturated chains exhibit enhanced transfection efficacy [90,94]. Here, it will be clearly demonstrated that 15% of saturated cationic lipids in the cost-efficient technical mixture are not at all harmful for lipofection purposes but rather advantageous.

The physical-chemical properties and the interaction with DNA of both samples have been studied in monolayers (2D systems) using a Langmuir trough in combination with various analytical methods (Infrared Reflection-Absorption Spectroscopy (IRRAS) and Grazing Incidence X-ray Diffraction (GIXD)) as well as in bulk (3D systems) using Small- and Wide-Angle X-Ray Scattering (SAXS and WAXS). Obtained results were correlated with transfection efficiency of both systems.

2. EXPERIMENTAL DETAILS

The experimental details have been described in chapter "Experimental details" at the end of the document.

Materials

The synthesis of N´-2-[(2,6-diamino-1-oxohexyl)amino]ethyl-2-hexadecyl-N-[(9Z)-octadec-9-enyl]propane diamide (Fig. 15) and its analytical analysis were described earlier [89]. All materials and reagents were purchased from Sigma-Aldrich Co Ltd. unless stated otherwise. All solvents were analytically pure and dried before use. Sodium salt of calf thymus deoxyribonucleic acid (D1501) was purchased from Sigma-Aldrich and used in a concentration of 0.1 mM (refers to a monomer containing one charge per phosphate moiety, ∼370 g/mol) for monolayer experiments and 2 mg/ml for bulk experiments. For all experiments at pH 10 and pH 4 carbonate buffer (5 mM) and citric buffer (5 mM) were used, respectively. All other chemicals were of analytical grade and used without further purification.

3. RESULTS

3.1 COMPOUNDS CHARACTERISTICS

Technical oleylamine as the relatively inexpensive alternative has been used by many groups for lipid synthesis [89,91-93,95]. Carefull analysis shows though that this multicomponent system contains only 75% oleylamine. The other compounds are amines with saturated chains (1.7% tetradecylamine, 5.9% hexadecylamine, 0.8% heptadecylamine, 6.2% octadecylamine) and other unsaturated chains (5.5% (*9Z*)-hexadec-9-en-1-ylamine, 1.5% (*9Z*)-heptadec-9-en-1-ylamine), and 3.4% unidentified compounds. However, this product is a primary amine to 98%. Chains of both *trans* (∼20%) and *cis* (∼80%) conformations are present in the compound. A comparable *cis*/*trans*-ratio was also described for oleyl chain containing gemini surfactants for gene transfer by Johnsson et al.[96] that used the commercially available oleyl alcohol. Here it is important to note that *trans* isomers have been often described as better transfectants than *cis* isomers.[94,97] The technical oleylamine was used for lipid 8 synthesis [89]. Since pure (*9Z*)-octadec-9-en-1-ylamine (oleylamine) is not commercially available, it was synthesized by our cooperators from pure (*9Z*)-octadec-9-enoic acid (oleic acid) in

multiple time- and cost-intensive steps and further used for the synthesis of lipid **8p** (purity grade ≥ 99%). In the compound only *cis* double bonds are present and no other derivatives were detected.
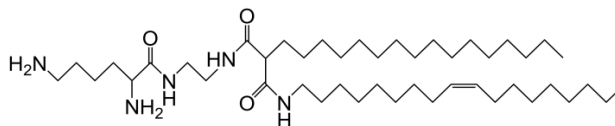

Fig. 15 Chemical structure of lipid 8. The difference between lipid 8p and lipid 8 is solely the degree of purity of the oleylamine moiety

3.2 MONOLAYER EXPERIMENTS (2D SYSTEMS)

3.2.1 On buffer solutions

3.2.1.1 Pressure-area isotherms

The π/A isotherms of lipids **8** and **8p** on the pH 10 buffer at 20 °C are presented in Fig. 16 A. Lipid **8p** undergoes a first-order phase transition from the liquid-expanded (LE) to a liquid-condensed (LC) state represented by the characteristic plateau region.[98] The beginning of the transition region of lipid **8p** at pH 10 is characterized by a small hump typical for an overcompression needed for the induction of the nucleation process. At pH 10, the molecules are considered to be deprotonated (uncharged). The charge is introduced by the possible protonation of the two primary amine groups in the headgroup of the molecules at lower pH values (pH 4). This leads to the expansion of the monolayer due to electrostatic repulsion (Fig. 16A). The same scenario can be observed for lipid **8**. However, the clear phase transition (plateau region) at pH 10 in the deprotonated state cannot be detected in the isotherm of lipid **8**. The missing plateau region is based on its multi-component character. Instead, a continuous change of molecular areas from values characteristic for an expanded phase to values typical for a condensed phase can be seen on compression (Fig. 16A). BAM images (Supporting Information, Fig. S1.2) show the coexistence of different phases in the multi-component lipid **8** monolayer. Even at pH 4, small condensed domains floating in the expanded phase of lipid **8** can be seen.
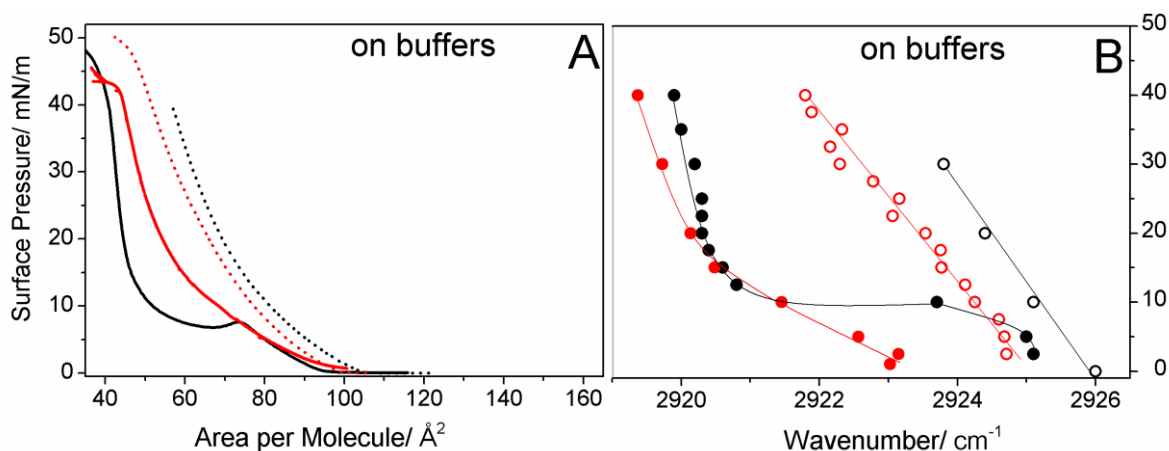
Fig. 16 Pressure/area isotherms (A) and positions of the asymmetric CH_2 stretching vibration band (B) along the compression isotherm at 20 °C of lipid 8p (black) and lipid 8 (red) on buffers: citric buffer pH 4 (A: dashed line, B: empty circles) and carbonate buffer pH 10 (A: solid line; B: filled circles). The lines in B are for eyes guidance only.

Since the first order phase transition of lipid **8p** at pH 10 is very well defined, the isotherms have been measured at different temperatures (Fig. 17) and the thermodynamical parameters of the transition have been extracted. The plateau characterizing the phase transition starts with an overcompression (hump at the beginning of the plateau region). The overcompression increases with increasing temperature. The temperature dependence of the transition pressure π_t, determined from the kink at the beginning of the plateau region (coexistence of LE and LC phases) but neglecting the overcompression, can be described by a linear function (Fig. 17). Extrapolation to zero transition pressure gives a T_0 value of 11.2 °C, which determines the lowest temperature of the existence of the liquid-expanded phase. Below this temperature, the transition into the condensed phase starts directly from the gas-analogous state. The slope $d\pi_t/dT$ of the linear function is 0.806 mN/(m·K). The two-dimensional Clausius-Clapeyron equation 14 representing a one-component approximation can be used for calculating the enthalpy change ΔH of the phase transition

$$\Delta H = (A_c - A_e)T \frac{d\pi_t}{dT}$$
eq.14

where A_e is the molecular area at the onset of the phase transition at the surface pressure π_t and A_c is the area of the condensed phase at this pressure.[36] The temperature dependence of the entropy change $\Delta S = \Delta H/T$ for the phase transition is presented in Fig. 17. Negative ΔS values are obtained according to the exothermic nature of the main

phase transition and an increase in the ordering of the system. The absolute ΔS values decrease as the temperature increases until reaching the critical temperature (T_c) of 45.4 °C above which the monolayer cannot be compressed to the condensed state. This value is considerably lower than the main transition temperature in bulk (57.1 °C), indicating that the packing in bilayers must be different compared to that in monolayers.
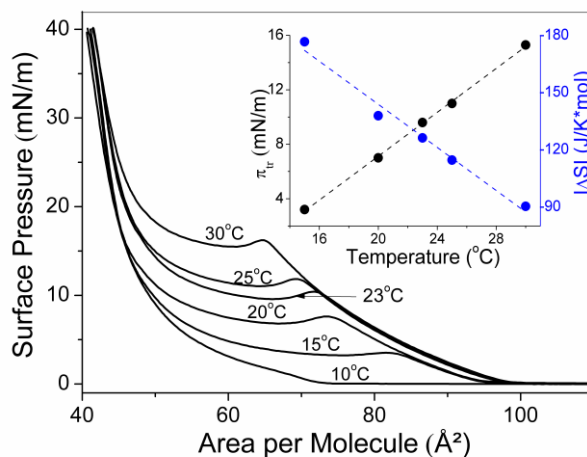

Fig. 17 Surface pressure/molecular area isotherms of lipid 8p spread on carbonate buffer, pH 10, at different temperatures (indicated). In the inset the transition pressure (black), π_t, and transition entropy (blue), ΔS, are plotted in dependence on temperature. The extrapolation of the presented linear fits (dashed lines) yields the characteristic temperatures (T_0 = 11.2 °C and T_c = 45.4 °C) described in the text.

The phase transition pressure does not only change in dependence on temperature but also on pH. At lower pH values, the transition pressure of lipid **8p** is shifted to higher values due to increasing electrostatic repulsion between the now charged headgroups. At pH 4 and 5 °C, the phase transition starts at $\pi_{tr} \sim 25$ mN/m (Figure S1.1). For comparison, the electrostatic repulsion at pH 4 has the same influence on the transition pressure as increasing the temperature to 43.5 °C at pH 10 when the headgroups are not charged.

3.2.1.2 *Infrared Reflection Absorption Spectroscopy*

The lipid phase state along the isotherms was checked by the position of the symmetric and asymmetric CH$_2$-stretching vibration band (Lorenzian curve fit). The LE phase is characterized by bands above 2854 cm^{-1} and 2924 cm^{-1}, respectively, while for the LC phase lower values (< 2850 cm^{-1} and < 2920 cm^{-1}, respectively) are observed [76]. The $v_{as}(CH_2)$ band positions of lipids **8p** and **8** on different buffers (pH 10 and pH 4) are

plotted as a function of the lateral surface pressure at 20 °C in Fig. 16 B. Both lipids are in the LE phase at pH 4 due to the protonation of the headgroups. For lipid **8**, the band is located at slightly smaller wavenumbers in comparison to lipid **8p**, which is the result of the presence of ~15% of saturated chains in the multi-component system, which remain in the condensed state even at low pH values (as shown by BAM). For this reason, lipid **8** exhibits a smooth LE/LC transition at basic pH, whereas the first order phase transition seen in the isotherm of lipid **8p** is characterized by a sharp decrease of the wavenumber of the $v_{as}(CH_2)$ band. The phase transition pressure amounts to ~10 mN/m, which is not the equilibrium value observed in the isotherm (~8 mN/m) at the same temperature but corresponds rather to the overcompressed state (hump in the isotherm) due to the experimental procedure (experiments are performed at a fixed pressure).

3.2.1.3 Grazing Incidence X-ray Diffraction

GIXD enables to determine the lattice structure in LC phases. Lipid **8p** and lipid **8** were studied at pH 4 and pH 10 at 5 °C and different surface pressures. As expected from isotherm and IRRAS experiments, lipid **8p** is in the LE phase and does not give a diffraction pattern at pH 4 below 30 mN/m (Fig. S1.1). Due to long-term instability of the layers, the diffraction has been not measured above this pressure. Monolayers of lipid **8** at pH 4 show a very weak diffraction pattern with two Bragg peaks even if the isotherm has the typical shape of an expanded layer. Obviously, the 15% of lipids with saturated chains create this weak diffraction pattern [85]. At high pH values (pH > 8), the headgroups are uncharged. Because of no electrostatic repulsion, the molecules form a condensed phase already at low surface pressures. Fig. 18 shows intensity contour plots of lipid **8p** and lipid **8** at pH 10 or pH 8, correspondingly. The Q_{xy} and Q_z values of the Bragg peaks, d, t and A_0 of lipid **8p** and lipid **8** are summarized in table S1.1 (Supporting Information).
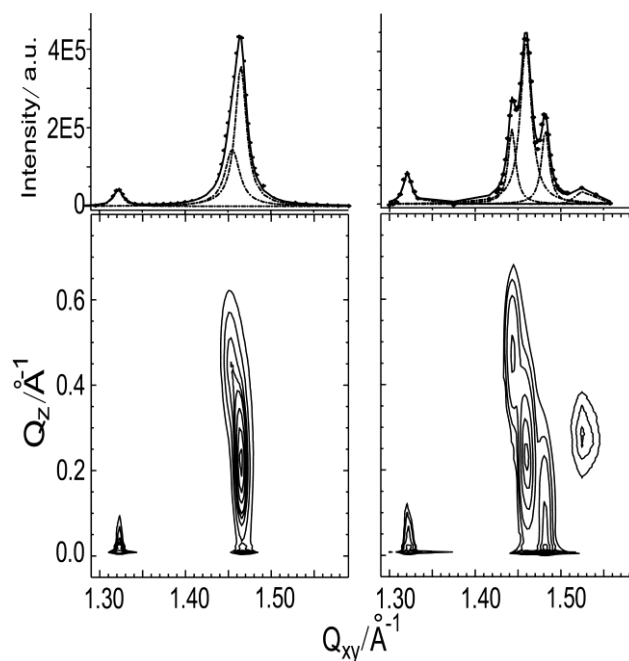
Fig. 18 Bragg peaks (top panel) and contour plots as a function of the in-plane scattering vector component Q_{xy} and the out-of-plane scattering vector component Q_z (bottom panel) of lipid 8p (left) and lipid 8 (right) monolayers on buffer, pH 10 or pH 8, correspondingly, at 5 °C.

The contour plot of lipid **8p** presents three well resolved diffraction peaks**.** The peak located at Q_{xy} = 1.322 Å^{-1} (corresponding to a *d*-value of 4.76 Å) and Q_z = 0 characterizes the formation of a hydrogen bond network which can be formed between the amide groups (NH as proton donor and C=O as proton acceptor). This Bragg peak does not change the position with increasing surface pressure, since the hydrogen bond length is well defined and fixed for a given type of interaction. The two other peaks can be assigned to the lipid chains lattice. Both Bragg rods are located above the horizon (Q_z^{nd} = 2·Q_z^d > 0). Such a diffraction pattern is typical for a rectangular unit cell with NNN (next-nearest neighbor) tilt of the chains (such a phase is typically called an Ov phase). Since the degenerated Bragg peak is located at higher Q_{xy} value, the unit cell is distorted in NNN direction [99]. Upon compression (from 5 to 30 mN/m), the two Bragg peaks change their relative position in Q_{xy}. This indicates a change in the distortion from NNN to NN (nearest neighbor). However, compression leads only to marginal changes of the chain tilt angle (17° at 5 mN/m to 14° at 30 mN/m, see Table S1.1, Supporting Information). The theoretical tilting phase transition pressure can be calculated by assuming that the molecular in-plane area (A_{xy}) depends linearly on the surface pressure and the chain cross-sectional area, A_0, is constant. The extrapolation of *1/cos(t)* versus π towards zero

tilt angle (*1/cos(t)* = 1) yields the transition pressure to the non-tilted state[100]. For lipid **8p**, this transition can be only expected above 75 mN/m, showing that the non-tilted state cannot be reached by compression due to the lattice immobilization by hydrogen bonds. For lipid **8** the calculated pressure is lower but also still too high to be reached (58 mN/m) (Fig. 19A). To distinguish between the effect of chain tilt and backbone ordering, one has to plot the lattice distortion *d* as function of $\sin^2 t$. A modified Landau theory of phase transitions in Langmuir monolayers [101,102] predicts a linear dependence (Fig. 19B). The extrapolation to zero tilt gives a d_0 value of -0.094 and 0 for lipid **8p** and lipid **8**, respectively. If d_0 is zero then only the tilt of the chains causes the lattice distortion. However, d_0 of lipid **8p** is clearly different from zero indicating that there are other contributions to the distortion. The value is very similar to the one observed in long-chain fatty acid monolayers in the 2D-crystalline S phase [103,104]. In the S phase, the unit cell is distorted in NN direction due to the ordering of the backbone planes (herringbone order). In such cases, the chain cross-sectional area A_0 is typically around 19 Å^2. Lipid **8p** has a chain cross-sectional area of ~20.4 Å^2, which is typical for freely rotating chains. Therefore, the reason for the unit cell distortion additionally to the chain tilt must be the rigid hydrogen bond network. This network, formed by linking headgroups of neighboring molecules, determines the shape of the unit cell with the observed distortion, but allowing the chain rotation and leading only to marginal changes of the chain tilt.
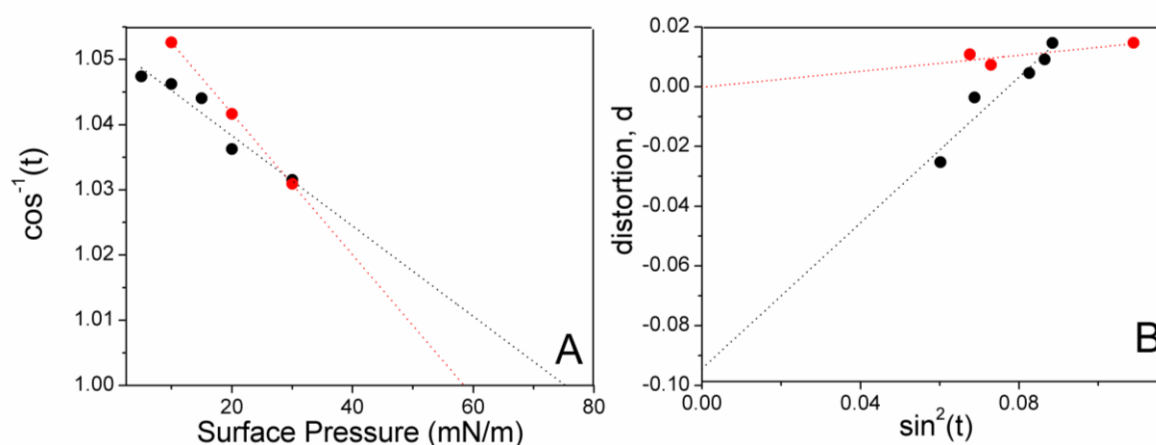

Fig. 19 Right panel: Plot of 1/cos(*t*) versus surface pressure for the lipid 8p (black) and lipid 8 (red) monolayers spread on carbonate buffer subphase, pH 10 and pH 8 respectively. Determined theoretical value of the pressure at which the tilt angle of lipid 8p and lipid 8 chains reaches 0 is π_{tr} = 75 and 58 mN/m, respectively. Left panel: Lattice distortion of the lipid 8p (black) and lipid 8 (red) monolayer versus $\sin^2(t)$ spread on carbonate buffer subphase, pH 10 and pH 8, respectively.

The FWHM of the Bragg rods can be directly translated into the length of the scattering unit L_z. L_z of lipid **8p** amounts to ~21 Å. This value can be compared with the theoretical length of the alkyl chains of lipid **8p** forming the hydrophobic part of the amphiphilic layer (1.26 Å per C-C in an *all-trans* conformation + 1.54 Å for the terminating CH_3 group[105]) of ~22 Å, showing that the whole chain is contributing to the scattering.

GIXD of lipid **8** shows a diffraction pattern originating from the superposition of two diffraction patterns of the multi-component system. The contour plot presented in Fig. 18 (left panel) shows five well resolved peaks. Two pairs of Bragg peaks belong to different lipid **8** chain lattices. One of them (Q_{xy} = 1.443 Å^{-1}, Q_z = 0.498 Å^{-1} and Q_{xy} = 1.459 Å^{-1}, Q_z = 0.249 Å^{-1}) is very similar to the one observed for lipid **8p** with only slightly different values giving rise to a slightly larger chain tilt angle (t = 19°, NNN) and a larger lattice distortion (d = 0.02, NNN) due to a partial miscibility with the other components of the mixture. The cross-sectional area per chain is not affected and equals 20.4 Å^2. The other two Bragg peaks (Q_{xy} = 1.481 Å^{-1}, Q_z = 0 Å^{-1} and Q_{xy} = 1.528 Å^{-1}, Q_z = 0.263 Å^{-1}) belong to a chain lattice of the saturated compounds. This lattice has a smaller cross-sectional chain area (A_0 = 19.5 Å^2) and tilt angle (t = 11.8°, NN) due to the tighter packing of saturated chains. The fifth peak at Q_{xy} = 1.321 and Q_z = 0 corresponds to the hydrogen bond network and is in the same position as that found in the lipid **8p** monolayer.

3.2.2 On DNA solutions

3.2.2.1 Pressure-area isotherms

On DNA containing subphases, the isotherms are characterized by an expansion effect (Fig. 20A). The reason for the pH dependent expansion could be electrostatic interaction between cationic lipids and anionic DNA as well as partial incorporation of DNA molecules into the lipid monolayer. The apparent areas per molecule (only the known number of lipids at the surface can be used for the calculation of molecular areas) are much larger at pH 4 than at basic pH. Lipid **8p** at pH 10 can be compressed to small areas per molecule (~55 Å^2), close to the ones characteristic for LC phases. However, the phase transition cannot be seen anymore in the isotherm. Since the headgroup is deprotonated at such high pH value, the interaction with DNA should be much weaker allowing an almost complete squeezing-out upon compression. Similar behavior can be observed for lipid **8**. There is also almost no difference in the strongly expanded

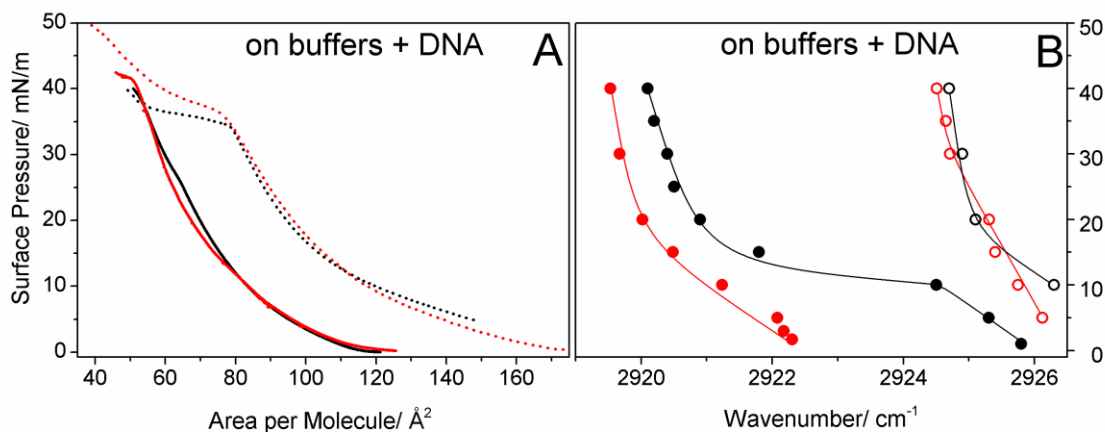isotherms of lipid **8p** and lipid **8** after DNA coupling at pH 4.

Fig. 20 Pressure/area isotherms (A) and the positions of ν_{as} (CH$_2$) band along the compression isotherm (B) at 20 °C of lipid 8p (black) and lipid 8 (red) on 0.1 mM solution of ctDNA in buffers: citric buffer, pH 4 (A: dashed line, B: empty circles) and carbonate buffer, pH 10 (A: solid line; B: filled circles). The lines in B are for eyes guidance only.

3.2.2.2   Infrared Reflection Absorption Spctroscopy

At pH 4, the electrostatic interaction with DNA leads to the expansion of both monolayers. The wavenumbers (Fig. 20B) indicate a completely fluid state of the alkyl chains at all pressures investigated. The influence of the components with saturated chains on the wavenumbers cannot be seen anymore, both lipids show identical wavenumbers on the DNA containing buffer at pH 4 indicating that all components in the multi-component mixture of lipid **8** are in the fluid state in contrast to the observation on the pure buffer. At pH 10, lipid **8p** shows the same wavenumber dependence as observed on the pure buffer. The first-order phase transition can be clearly seen at ~10 mN/m, indicating that there is no interaction between the uncharged lipids and DNA. The expanded isotherms show only that at low pressure (low lipid density at the air/buffer interface) a small amount of DNA molecules can penetrate into the liquid lipid film, but will be squeezed-out upon compression. The same is valid for lipid **8** with slightly lower wavenumbers and the more continuous transition due to the presence of components with saturated chains.

Quantification of bound DNA. Since DNA is the only compound having phosphate groups, the relative amount of DNA attached to the monolayer can be estimated by determination of the intensity of typical symmetric, ν_s *(PO$_2$)*, and asymmetric, ν_{as} *(PO$_2$)*,

phosphate diester bands at around 1082 cm^{-1} and 1238 cm^{-1}, respectively (example spectra Fig. 10). The presence of DNA can also be deduced from the DNA backbone band at 970 cm^{-1} [106-108]. To check a possible influence of the orientation of DNA molecules on the signal intensity, the dichroic ratio (DR) was calculated with $DR = A_p/A_s$ where A_p and A_s are the maxima of reflectance absorbance (RA) obtained with p- and s-polarized light, respectively. No changes of DR have been observed indicating that the amount of bound DNA can be quantitatively determined [24].

Fig. 21 shows the phosphate band intensity as a measure of the amount of DNA bound to lipid **8p** and lipid **8** monolayers at pH 4 and pH 10 plotted versus the area per molecule. It can be concluded that decreasing pH (increase of the protonation degree) increases the amount of attached DNA. At pH 10, the signal intensity in the phosphate region is in the order of baseline deviations caused by slightly different water heights in the reference and sample troughs. Therefore, we can conclude that only a non-measurable amount of DNA is attached to the lipid monolayers at high pH values. At pH 4, a considerable amount of DNA is bound to the lipid monolayers. There is no difference between the two samples (pure and mixed systems) concerning the amount of attached DNA. Compression of the lipid layers leads to an increase in the charge density and increases therefore the amount of attached DNA.
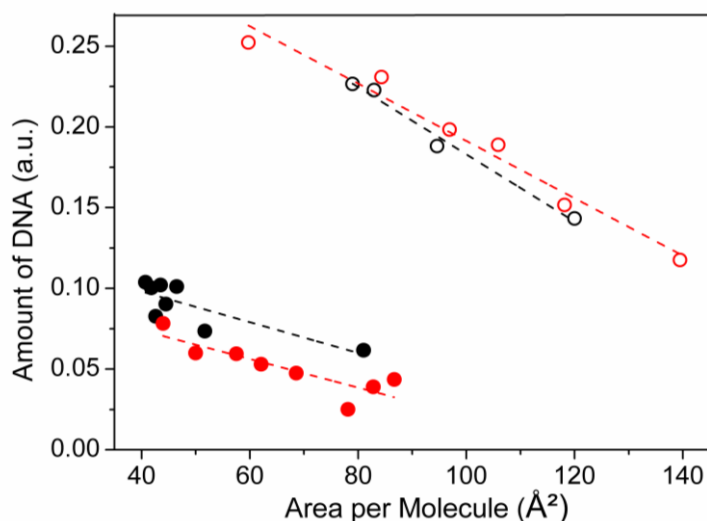

Fig. 21 Amount of DNA bound to lipid 8p (black) and lipid 8 (red) monolayers spread on 0.1 mM ctDNA in citric buffer, pH 4 (empty circles) and carbonate buffer pH 10 (filled circles) along the compression isotherm at 20 °C.

3.3 BULK EXPERIMENTS (3D SYSTEMS)

The lipids **8p** and **8** as well as their mixtures with cholesterol and DNA have been examined in bulk by DSC and SAXS/WAXS experiments. The mixing ratio of lipid to cholesterol of 1:1 was chosen based on the fact that this is the best transfecting mixture in a series of systematically designed transfection complexes with different ratios.

3.3.1 Pure lipids

3.3.1.1 Differential Scanning Calorimetry

Phase transitions in aqueous dispersions have been investigated by means of DSC (Fig. 22). By comparing the peak shape of the heating curves of lipid **8** and lipid **8p** it is obvious that the ones of lipid **8** are broader and less intense at all three investigated pH values, a typical phenomenon for lipid mixtures [109,110]. The two buffer systems exhibit defined pH values, the aqueous lipid dispersions show pH values between 7 and 8 due to the addition of the basic lipids. Both systems, lipid **8p** and lipid **8**, show a decrease of the T_m values with decreasing pH. Furthermore, both lipid systems exhibit the lowest ΔH and ΔS values as well as the largest FWHM values in citric buffer (pH 4). This behavior is in accordance with the increased protonation degree (increasing electrostatic repulsion) leading to the destabilization of the gel phase [111]. At the same pH, the T_m values of lipid **8** are higher compared to those of lipid **8p** due to the presence of 15% amines with saturated chains. Detailed analysis of the DSC curves of lipid **8** shows additional peaks/shoulders due to de-mixing processes in the multi-component sample.
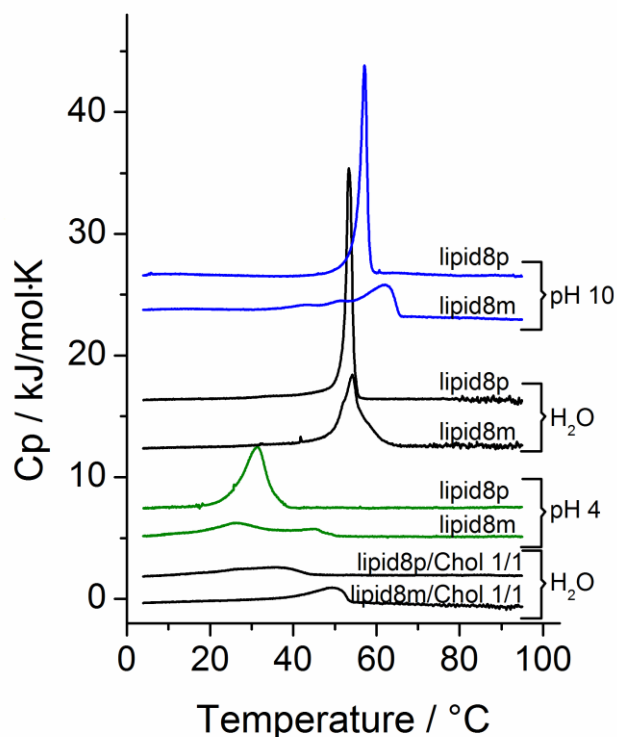
Fig. 22 DSC heating scans of aqueous dispersions of lipid 8p and lipid 8 (c = 1 mg·mL⁻¹) and their mixtures with cholesterol (n/n 1/1) (c = 3 mM) (media: carbonate buffer 10 mM, pH 10, water, citric buffer 5 mM, pH 4). The heating rate was 60 K·h⁻¹. Curves are shifted vertically for clarity.

3.3.1.2 Small- and wide angle X-ray scattering

Fig. 23A shows SAXS patterns of 20 wt% of lipid **8p** in carbonate buffer, pH 10, below and above the main phase transition temperatures. The gel phase is characterized by two Bragg peaks with a $s_1{:}s_2$ ratio of 1:2 indicating a multilamellar structure. The gel phase WAXS pattern of lipid **8p** (Fig. 23B) in carbonate buffer is characterized by two Bragg peaks corresponding to an orthorhombic lipid chain lattice (s_1 = 2.415 nm⁻¹ and s_2 = 2.469 nm⁻¹ at 30 °C) perpendicular to the chain axis typical for lamellar gel phases with tilted chains, $L_{\beta'}$.[67] The cross-sectional area of the chains amounts to A_0 = 19.5 Å², and is therefore smaller than the one determined by GIXD in monolayers (A_0 = 20.3 Å²). Above T_m, only a broad halo characteristic for fluid chains can be seen. Therefore, lipid **8p** shows the typical transition from a lamellar gel phase ($L_{\beta'}$) to a lamellar liquid-crystalline phase (L_α) at pH 10. This transition is accompanied with a shift of the Bragg peaks to larger s-values (from d = 70.9 Å at 30 °C to d = 59.5 Å at 70 °C) (Fig. 23A). The observed decrease of ~11 Å in the bilayer thickness can be solely explained by the

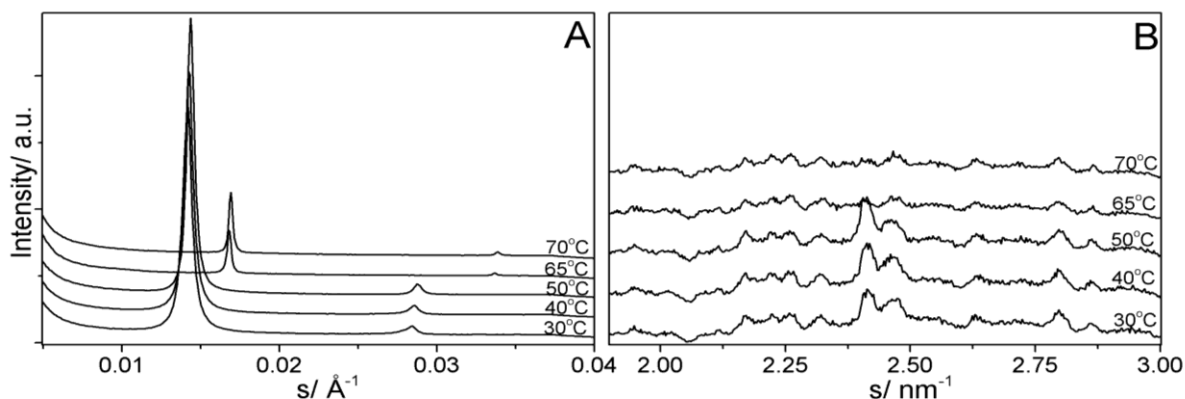melting of the chains keeping the water layer between the lipid bilayers almost constant.

Fig. 23 SAXS (A) and WAXS (B) of lipid 8p dispersion in carbonate buffer, pH10 at different temperatures.

The diffraction peaks from the gel phase observed in water are broader indicating smaller correlation length between the bilayers (Fig. 24A). The gel phases in water of both lipid **8p** and lipid **8** are characterized by the same *d*-values. The *d*-value of lipid **8p** decreases slightly with increasing temperature from 72.5 Å at 30 °C to 71.2 Å at 55 °C (Fig. 24A). The gel phase WAXS patterns of lipid **8p** (Fig. 24B) in water are again characterized by two Bragg peaks ($L_{\beta'}$). The additional weak Bragg peak at s = 2.15 nm^{-1} (*d* = 0.465 nm) is typical for hydrogen bonds which can be formed between amine and carbonyl oxygen in the hydrophilic headgroup region. The packing density is lower in the lipid **8** bilayers (larger A_0 values) compared to the pure lipid **8p**. In both cases, A_0 increases slightly with increasing temperature. The melting in water is connected with the appearance of a lamellar L_α phase (*d* = 63.6 Å at 60 °C), but several other Bragg peaks in a ratio characteristic for a cubic phase appear additionally (Fig. 24A). The cubic phase has been identified as body-centered cubic with Im3m symmetry. Fig. 25 presents the *s* values as function of $(h^2+k^2+l^2)^{1/2}$ with *h, k, l* as the corresponding Miller indices of the Bragg peaks. The dependence is linear and the extrapolation goes through zero what proves the correctness of the structure identification [60]. The calculated cubic unit cell parameter, *a = 1/slope* of the linear fit, amounts to 265 Å. At 70 °C, only the Q_α phase is present in the system.
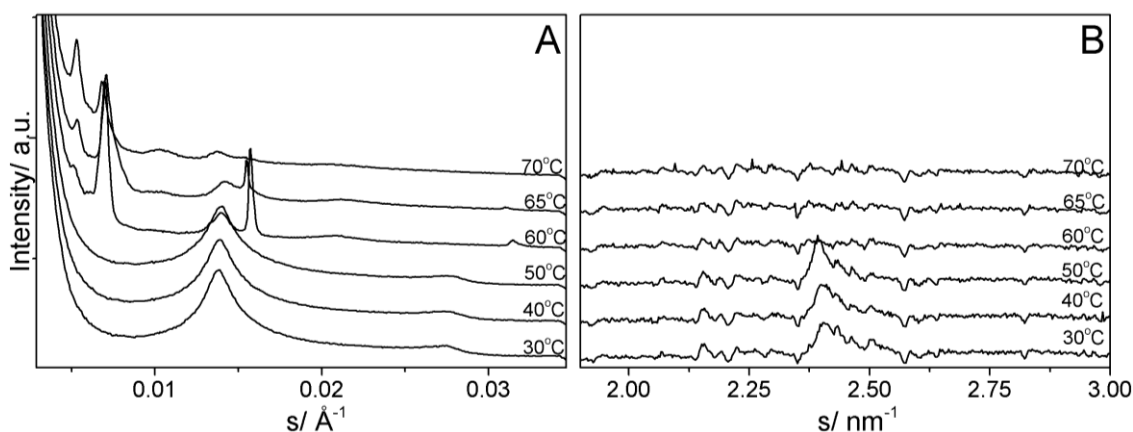
Fig. 24 SAXS (A) and WAXS (B) of lipid 8p dispersion in water (20 wt-% lipid)
at different temperatures.

Fig. 25 Indexed reflexes of body-centered cubic phase of lipid 8p disspersion in water at 70°C
versus their *s* positions.

At pH 4, a similar behavior has been observed. A reasonable scenario is therefore the formation of a lamellar L_α phase at high pH in the non-protonated state, which transforms into the Q_α phase at elevated temperatures, and a cubic phase at low pH in the fully protonated state.

Fig. 26 Comparison of SAXS patterns of lipid 8p: A - in water at 30 °C (below the main phase transition); B – in water at 70 °C (above the main phase transition). The Bragg peaks belonging to the cubic phase are indexed a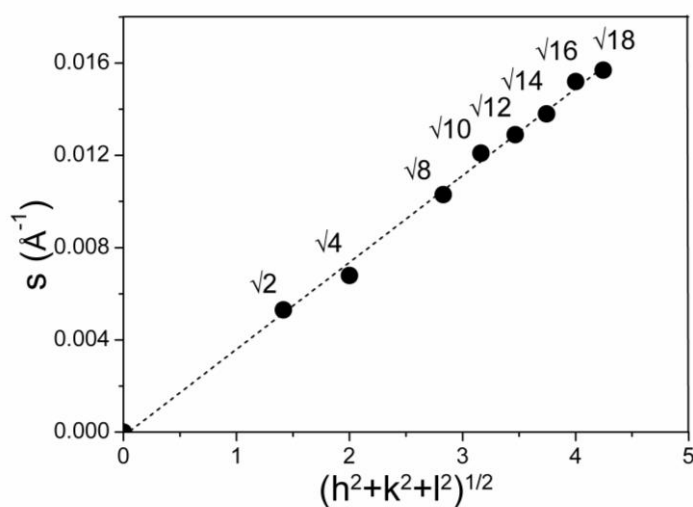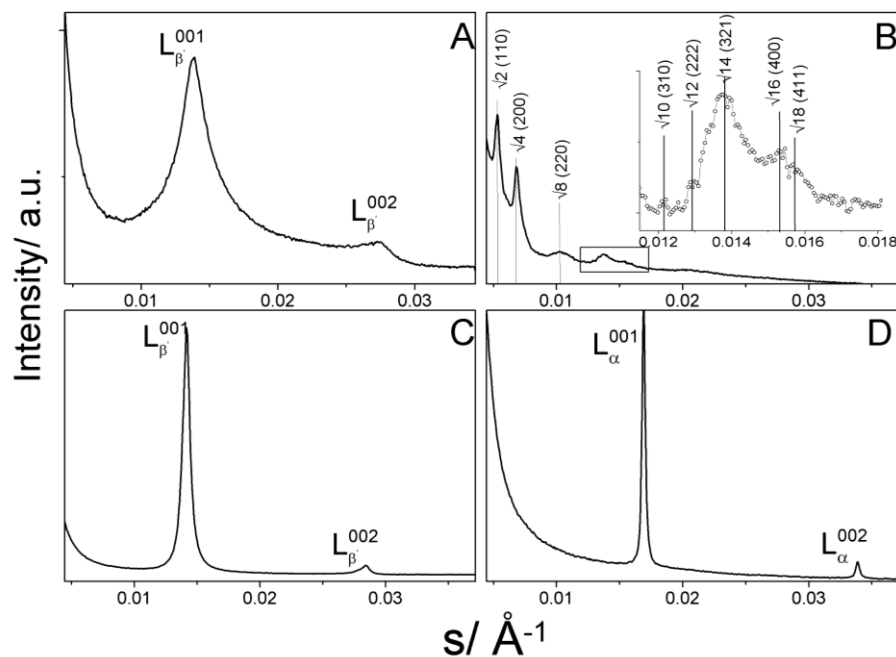nd indicated with lines (the √6 peak is missing); C – in pH 10 buffer at 30 °C (below the main phase transition); D - in pH 10 buffer at 70 °C (above the main phase transition).

3.3.2 Lipid/cholesterol 1:1 mixtures

3.3.2.1 Differential Scanning Calorimetry

Additionally, mixtures of lipid **8p** and lipid **8** with cholesterol (50 mol%) have been investigated in water. Addition of cholesterol decreases T_m and increases the FWHM (lipid **8p**/chol 1/1: T_m = 35.2 °C; lipid **8**/Chol 1/1: T_m = 49.3 °C) (according to DSC, Fig. 22). This phenomenon is also described for other phospholipid/cholesterol mixtures.[69] But in contrast to phospholipid/cholesterol mixtures, in which the main transition disappears at 40-60% cholesterol, we clearly see a phase transition in the 1/1 mixtures. This could indicate that only a small part of cholesterol is incorporated into the lipid gel phase. The lipid **8**/chol mixture undergoes the phase transition between 40 and 55 °C, lipid **8p**/ chol between 25 and 45 °C.
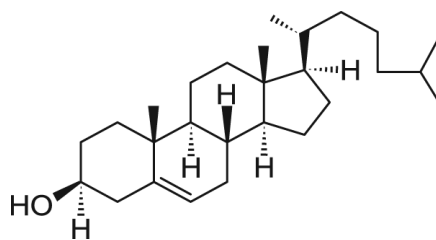
Fig. 27 The chemical structure of cholesterol

3.3.2.2 Small- and wide angle X-ray scattering

SAXS and WAXS patterns of the 1:1 lipid **8p** and cholesterol mixture are shown in Fig. 28. Below the main phase transition, lipid **8p**/chol exhibits a lamellar structure. The Bragg peak at $s_{001} = 0.014$ Å^{-1} shows that the incorporation of cholesterol leads only to a small decrease of the *d*-value by ~1 Å. Only some cholesterol is incorporated into the lipid gel phase, a large amount of cholesterol stays phase separated as anhydrous crystals (L$_c$) indicated by a Bragg peak at $s = 0.029$ Å^{-1}. This anhydrous crystals show a low enthalpy transition at 37 °C in water, which is much below the melting point around 148 °C, in accordance with literature data [112,113]. The lipid **8p**/chol mixture forms an L$_\alpha$ phase with similar *d*-values as lipid **8p** alone and the body-centred cubic phase above the main phase transition temperature (the broad transition range is finished at ~45 °C). The small percentage of incorporated cholesterol lowers the T_m value by changing the in-plane packing in the gel phase without noticeable change of the interlamellar repeat distance *d*. The appearance of two coexisting phases (L$_\alpha$ and Q$_\alpha$) just above the main phase transition is not influenced by the incorporated cholesterol. At higher temperatures (50 °C), no Bragg peaks of cholesterol crystals can be seen in the diffraction patterns indicating that now all cholesterol is incorporated into the two liquid-crystalline phases L$_\alpha$ and Q$_\alpha$.
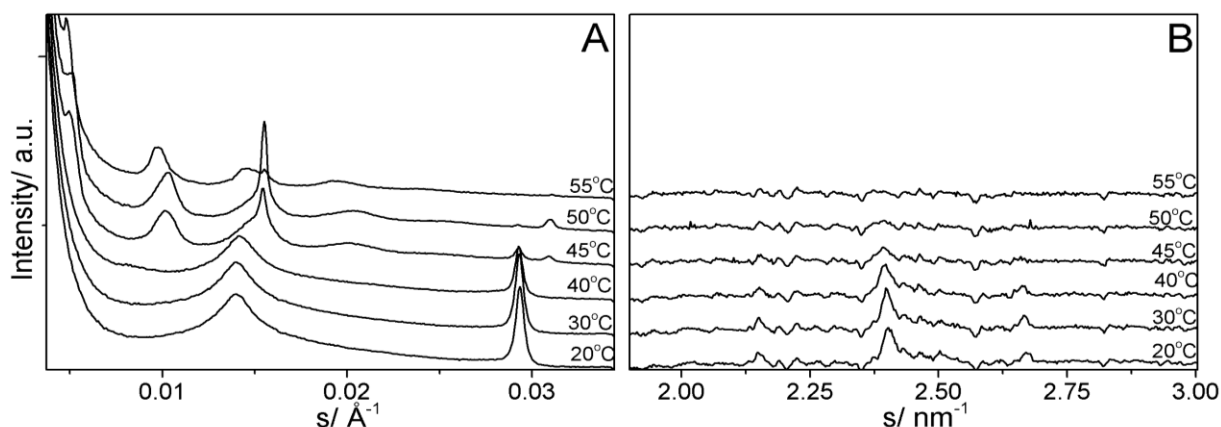
Fig. 28 SAXS (A) and WAXS (B) of lipid 8p/chol (1:1) dispersion in water at different temperatures.

The cooling DSC scan (Figure S1.3) shows a larger hysteresis with two exothermic transitions. The first one at higher temperature (35 °C) with the much lower enthalpy change must be connected with the Q_α-L_α transition. The second transition with the much larger ΔH value at 28 °C is then the transition into the gel state connected with the formation of phase-separated crystalline cholesterol.

For lipid **8**/chol, only one SAXS measurement at 20 °C has been performed [23] showing that the gel phase structure is also unchanged, except a small decrease of the d value by ~1.5 Å, and a large part of cholesterol is phase-separated. WAXS experiments to detect a possible in-plane phase separation between the saturated and unsaturated components have not been performed.

3.3.3 Lipid/cholesterol 1:1 mixtures complexed with DNA

3.3.3.1   *Small- and wide angle X-ray scattering and Differential Scanning calorimetry*

Fig. 29 shows SAXS patterns of lipid **8p**/chol (1:1) mixed with DNA (N/P ratio 3:1, where N refers to the amino groups of the lipid, which can be protonated, and P to the negatively charged phosphate groups of DNA). At lower temperatures (gel phase) three diffraction peaks can be observed. The Bragg peak at s = 0.029 Å^{-1} belongs to the phase-separated crystalline anhydrous cholesterol. The two other peaks (s_{001} = 0.0118 Å^{-1} and s_{002} = 0.0236 Å^{-1} at 20 °C) are in a ratio of 1:2 and belong to the lamellar phase of the lipid **8p**/chol/DNA complex with an increased d value (84.7 Å). It has been reported that incorporated DNA can exhibit a one-dimensional periodicity between aligned strands

located between the lipid layers[66], but in the present case no additional DNA peak was observed. The *d* values of the lipoplex are approximately 12 Å larger compared to the *d* values of the gel phases of the pure lipid **8p** and the lipid **8p**/chol mixture. However, the diameter of a double-stranded DNA is ~20 Å [65,66,114] Comparing these two *d* values leads to the conclusion that the incorporation of DNA induces a partial squeeze-out of water between the lipid bilayers or a changed orientation of the lipid headgroups connected with changes in the tilt angle of the chains [115]. The absence of any other diffraction peak in the SAXS pattern proves that the lipoplex forms a homogenous gel phase, in contrast to lipid **8**/chol/DNA, which shows the coexistence of two lamellar phases: one with incorporated DNA (s_{001} = 0.0117 Å^{-1}, *d* = 85.5 Å) and one without DNA (s_{001} = 0.0133 Å^{-1}, *d* = 75.2 Å) (Fig. 30) [23].
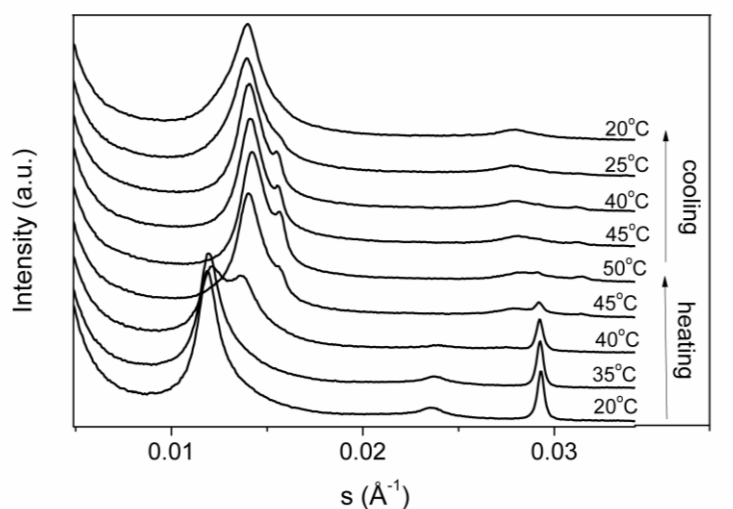
Fig. 29 Heating and cooling SAXS scans of lipid 8p/chol (1:1)/ DNA (N/P 3:1) dispersion in water.

Heating of the sample leads to the main phase transition at ~40 °C with the appearance of a lamellar phase with a *d*-value of 73 Å. This value is only by 8 Å larger compared with the L_α phase in the lipid **8p**/chol mixture without DNA. Even if the increase in *d* is quite small, this liquid-crystalline phase should contain DNA. Further heating leads to another Bragg peak at the position expected for the pure L_α phase (*d* ~ 65 Å) with no DNA incorporated. It is very interesting to note that the appearance of the Q_α phase is completely suppressed by the presence of DNA. Cooling the sample from 50 °C to 20 °C shows that the L_α phase containing the DNA can be markedly supercooled (Fig. 29). Additionally, it is interesting to compare the DSC cooling curves of lipid **8p**/chol mixture

without DNA (Figure S1.3) and with DNA (Figure S1.4). After adding the DNA, the supercooling effect is much smaller and the small transition attributed to Q_α-L_α is not present in accordance with the X-ray results showing the absence of the Q_α phase in the DNA containing mixture.

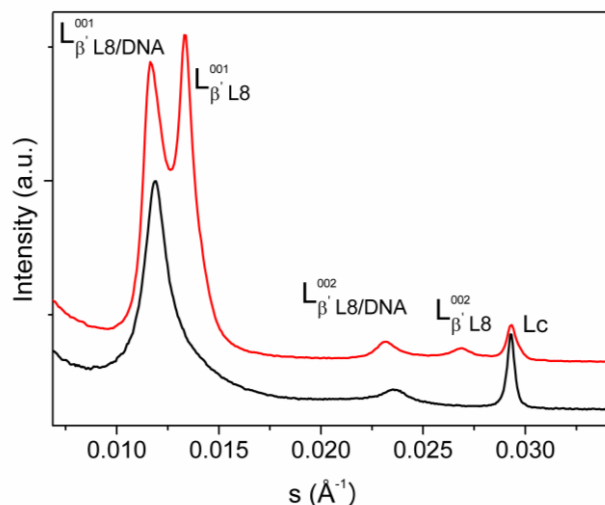Fig. 30 Comparison of SAXS patterns of water dispersions of lipid 8p/chol/DNA (black) and lipid 8/chol/DNA (red) complexes at 20 °C. The diffraction pattern of the lipid 8/chol/DNA mixture shows phase separation into two phases: with ($L_{\beta' L8/DNA}$) and without DNA ($L_{\beta' L8}$), while the lipid 8p/chol/DNA mixture exhibits one homogeneous phase filled with DNA. In both cases, phase separated cholesterol can be observed (L_c).

3 CONCLUSIONS

There are many features that influence the transfection efficiency of a given cationic lipid system (lipoplex structure, charge, type of the cell etc.). Nevertheless, several common theories on the properties of the lipofection systems have been established. This work shows that they do not apply for each system and cannot be taken as a recipe for a perfect nucleic acid carrier lipid. The first commonly known rule says that systems which tend to form non-lamellar structures are better transfectants due to better fusogenic properties that enable their mixing with a cell and endosome membrane. Here though, lipid **8p** that forms cubic phases transfects very poorly in comparison with lamellar lipid 8. Additionally, its oleyl chain is a pure *cis*-conformer which is believed to improve transfection compared with its *trans-* analogue. By contrast, technical grade lipid **8** is a mixture of *cis* and *trans* conformers. Also the limited miscibility of the lipid **8** with DNA seems to be advantageous in relation to the perfect mixture of lipid **8p**/ chol/ DNA.

Supporting Information can be found in the appendix. The details of monolayer experiments: pressure/area isotherms and IRRAS at different temperatures, table of parameters derived from GIXD; and bulk experiments: additional DSC scans are described there.

CHAPTER 2

THE INFLUENCE OF THE LIPID HEADGROUP STRUCTURE ON PHYSICAL-CHEMICAL PROPERTIES AND TRANSFECTION EFFICIENCY

1. INTRODUCTION

Cationic lipids are composed of a hydrophobic core represented by one of two types of moiety: cholesterol or two long hydrocarbon chains, a cationic headgroup accountable for the binding of DNA, and a so-called linker which connects the hydrophobic part with the polar headgroup region. Whereas the "classic" transfection lipids like DOTMA[15], DOSPA or DOGS[116], which have the glycerol backbone to connect the hydrophobic chains with the polar region, other lipids are derivatives of cholesterol or aromatic interfaces (SAINT)[117]. Due to the fact that ether bonds present in linker possess high toxicity[118] and ether formulation is a synthesis yield limiting procedure (especially with double bonds) a new biodegradable backbone based on malonic acid amides was developed [119]. By the introduction of spacers and lysine residues as polar headgroup constituents these lipids show better or just as good transfection efficiency compared with the commercial available transfection agents like Lipofectamine®2000, Lipofectamine®, and Superfect® [90,120].

Since it was already shown that the hydrophobic core has an eminent effect[46] on transfection efficacy, the main focus in this research has been put on the importance of the polar moiety structure. Three compounds of a new class of transfecting lipids with two hydrophobic chains structurally apart from glycerol containing substances were studied. The hydrophobic molecule part of each of the lipids is represented by two acyl chains (14:0 and 16:0) connected via a spacer with a basic headgroup. The structure of the headgroup for each of the compound differs by size and possible charge (Fig. 31). For purpose of the study, the monolayer phase behavior of the three lipids **E14/16**, **E14/16Lys** and **T14/16diLys**, have been examined and compared. Their monolayer properties at the air-water interface in presence and absence of model DNA in the

subphase have been investigated using Langmuir Microbalance combined with Infrared Reflection-Absorption Spectroscopy (IRRAS) and Grazing Incidence X-ray Diffraction (GIXD). The two dimensional binding of the monolayers with model DNA has been also examined. Experimental results have been correlated with transfection efficiencies and the structure/function relationship has been discussed.

It has been shown that the transfection efficiency *in-vivo* can be correlated to the headgroup size and possible protonation. Those two properties influence the membrane fluidity and amount of DNA that the molecule is able to bind. It will be shown that the most fluid and most protonated lipid, **T14/16diLys,** is far better for transfection than its analogues with smaller hydrophilic parts. Nevertheless, the monolayer experiments do not give an unambiguous answer to the direct correlation between the headgroup charge and amount of attached DNA.

2. EXPERIMENTAL DETAILS

The experimental details have been described in chapter "Experimental details".

Materials
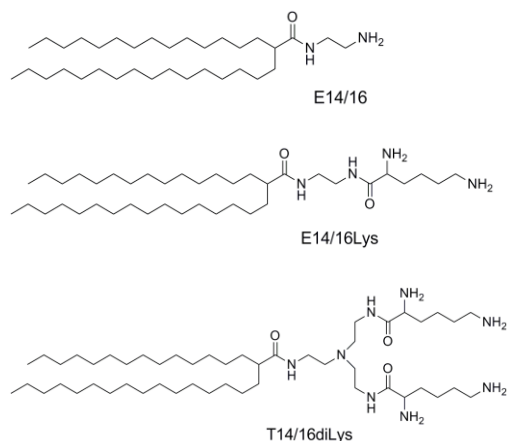
Fig. 31 Chemical structures of E14/16, E14/16Lys and T14/16diLys.

The three lipids, **E14/16, E14/16Lys** and **T14/16diLys** (Fig. 31) were synthesized by the cooperators from the Department of Pharmacy, Martin Luther University in Halle. If not mentioned otherwise, chemicals were purchased from Sigma-Aldrich. All solvents were analytically pure and dried before use. Sodium salt of calf thymus deoxyribonucleic acid (D1501) was purchased from Sigma-Aldrich and used in a concentration of 0.1 mM (refers to a monomer containing one charge per phosphate moiety, ~370 g/mol) for monolayer experiments. For all experiments at pH 10 and pH 4 carbonate buffer (5 mM) and citric buffer (5 mM) were used, respectively. All other chemicals were of analytical grade and used without further purification.

3. RESULTS AND DISCUSSION

3.1 PRESSURE-AREA ISOTHERMS AND THERMODYNAMICS OF THE PHASE TRANSITION

The π_{tr} /A isotherms of **E14/16** and **E14/16Lys** monolayers spread on the water subphase at different temperatures and lipid **T14/16diLys** spread on water at 20 °C are presented in Fig. 32.
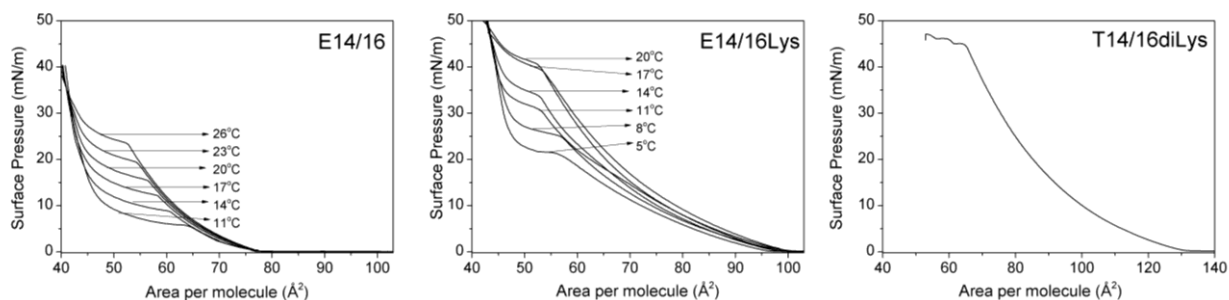
Fig. 32 Pressure/area isotherms of A -E14/16, B- E14/16Lys monolayer on water subphase in different temperatures and C- E14/16diLys at 20 °C.

In the analyzed range of temperatures, during compression lipids **E14/16** and **E14/16Lys** show the first order phase transition from liquid expanded (LE) to liquid condensed (LC) phase. At 20 °C **T14/16diLys** remains expanded up to the pressure of ~45 mN/m, when the monolayer collapses and no phase transition can be seen. For **E14/16** a second order phase transition (LC/LC$_{t=0}$) can be also observed, and is indicated by a characteristic kink resulting in change of slope of isotherm in the LC lipid state (for all isotherms it is around 26 mN/m). The kink corresponds to the transition from the tilted to the non-tilted state and is shown in Fig. 33.

Fig. 33 The second order phase transition from tilted to untilted state of the chains of the E14/16 monolayer on water at 11 °C. The graph shows magnified transition region and and the inset presents a complete isotherm.

Using two-dimensional Clausius – Clyperon eq. 15 a quantitative thermodynamic analysis of both lipids LE /LC first order phase transitions can be evaluated:

$$d\pi_{tr}/dT = (S_{LC} – S_{LE}) / (A_{LC} – A_{LE}) = \Delta S_{tr} / \Delta A_{tr} \qquad \text{eq.15}$$

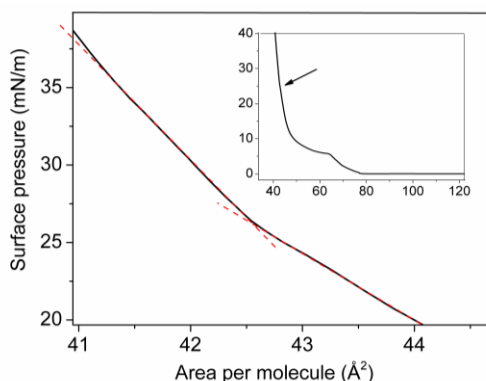where T is a temperature of measurement, π_{tr} is the phase transition pressure, understood as a kink being a beginning of characteristic plato (coexistence of LE and LC phase) on the π/A isotherm, $\Delta S_{tr} = S_{LE} - S_{LC}$ is the transition entropy which equals the difference of the entropies in liquid-expanded and liquid-condensed phase and $\Delta A_{tr} = A_{LE} - A_{LC}$ is the change in molecular area. A_{LE} corresponds to the molecular area at π_{tr} and A_{LC} was taken as the extrapolated value of the isotherm to π_{tr}. Exact determination of A_{LC} have been described elsewhere[121,122].

Using ΔS_{tr} one can determine the heat of transition which can be calculated by eq. 16

$$\Delta Q_{tr} = \Delta S_{tr} T \qquad \text{eq.16}$$

As mentioned before, lipid **E14/16** shows the first order transition from LE to LC phase of all measured temperatures (11 – 26 °C). Its isotherms are very regular. π_{tr} equals 5.5 mN/m at 11 °C and shifts 3 – 4 mN/m towards higher values for each 3 degrees increase of temperature what yields in the linear π_{tr}/T dependence with a slope of $d\pi_{tr}/dT = 1.19$ mN/m K (Fig. 34A). Extrapolation of this dependence towards $\pi_{tr} = 0$ allows to estimate T_0, which is the temperature below which the LE phase no longer exists. In this case $T_0 \approx$ 5 °C. As expected, ΔA_{tr} decreases linearly with temperature increase (from 16 to 6 A^2 per molecule for 11 and 26 °C, respectively). Knowing the $d\pi_{tr}/dT$ and ΔA_{tr} at given temperature one can calculate ΔS_{tr} value. The subsequent application of eq. 15 for each temperature leads to $\Delta S_{tr}(T)$ dependence which is linear for **E14/16**. The transition heat ΔQ_{tr} can be determined with eq. 16 by substitution of ΔS_{tr}. By extrapolation of ΔQ_{tr} (T) to $\Delta Q_{tr} = 0$, the critical temperature (T_c) can be obtained (Fig. 34B). Above T_c, LC state cannot be reached by further compression, phase transition vanishes and there is no distinction between LC and LE two-dimensional phases. For **E14/16** on the water subphase $T_c \approx 36.6$ °C.
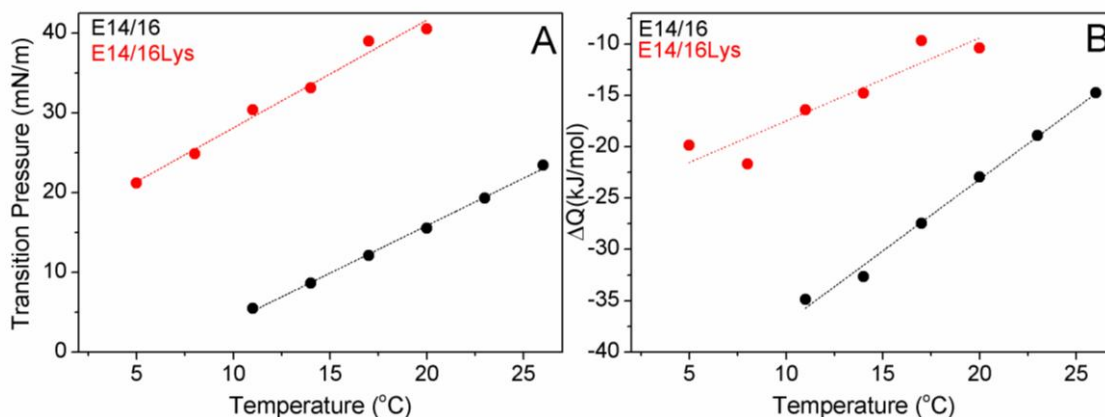
Fig. 34 Transition pressure (A) and enthalpy (B) of E14/16 (black) and E14/16Lys (red) as a function of temperature and their linear fits (dotted lines).

In comparison to **E14/16**, the LE/LC phase transition of lipid **E14/16Lys** is shifted to higher pressures (for example for T= 11 °C, π_{tr} of **E14/16** and **E14/16Lys** equal 5.5 and 30.4 mN/m respectively). This difference is an effect of a bigger size of the **E14/16Lys** headgroup which does not allow carbon chains to align at lower pressures. Moreover, **E14/16Lys** has two primary amine groups in the headgroup (while **E14/16** has only one) which are assumed to be mostly protonated in CO_2 saturated pure water (pH≈ 5.5), so there is an electrostatic repulsion between positively charged headgroups, that leads to the additional expansion of the monolayer. The isotherms of **E14/16Lys** measured at temperature between 5 – 20 °C, are not arranged very regularly, but still the $\pi_{tr}(T)$ dependence is linear ($d\pi_{tr}/dT$ = 1.35 mN/m K). The rest of the derived values (ΔA_{tr} ΔS_{tr}, ΔQ_{tr}) can be also presented as the linear function of T. Two characteristic temperatures of **E14/16Lys** on the water subphase can be determined: T_0 and T_c equal -11.8 and 31.6 °C, respectively, which are both lower than the corresponding temperatures of **E14/16** and also here the difference can be explained by the larger size and charge of the **E14/16Lys** headgroup. All ΔS and ΔQ values for both lipids are negative what indicates increase of order in the layer and heat evolution while phase transition. Data used to evaluate thermodynamics of both lipids are summarized in the Table 2.

Table 2 Thermodynamic parameters of LE/LC first order phase transition of E14/16 and E14/16Lys monolayers spread on water.

T [K]	π_{tr} [mN/m]	A_{LC}	A_{LE} [A² / molecule]	ΔA_{tr}	ΔS_{tr} [J/ mol*K]	ΔQ_{tr} [kJ/ mol]
E14/16						
284	5.5	47.2	64.4	-17.1	-122.8	-34.9
287	8.6	44.8	60.7	-15.9	-113.7	-32.6
290	12.1	45.2	58.4	-13.2	-94.7	-27.5
293	15.5	45.3	56.2	-10.9	-78.3	-22.9
296	19.3	45.4	54.3	-8.9	-63.9	-18.9
299	23.4	45.6	52.5	-6.9	-49.3	-14.7
E14/16Lys						
278	21,2	47.5	56.3	-8.8	-71.4	-19.8
281	24,9	47.5	56.9	-9.5	-77.1	-21.7
284	30,4	46.1	53.2	-7.1	-57.7	-16.4
287	33,1	46.9	53.2	-6.3	-51.5	-14.8
290	39,0	49.4	53.5	-4.1	-33.3	-9.7
293	40,5	48.1	52.5	-4.3	-35.4	-10.4

3.2 ELASTICITY OF MONOLAYERS

Using eq.17 the elasticity, ε_0, that is a value defining monolayers capacity for energy storage, was calculated for the three lipids at 20 °C [123-125].

$\varepsilon_0 = -A (d\pi/dA)$ eq.17

In the equation *3*, *A* is a molecular area at given pressure and *dπ/dA* is the slope of isotherm at the given *A*. At 20 °C both, **E14/16** and **E14/16Lys** monolayers undergo the first order phase transition, while the monolayer of **T14/16diLys** remains liquid up to the collapse. Fig. 35A shows that monolayers of all lipids have very similar elastic properties in the LE phase which are comparable with those reported for DOPC[126] (zwitterionic lipid with two oleyl chains).
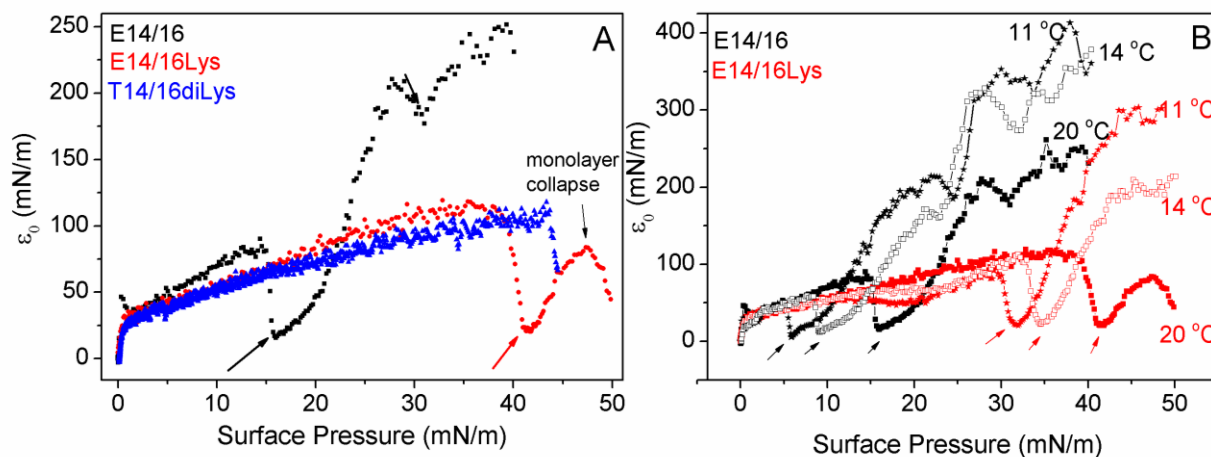
Fig. 35 Elasticity of E14/16 (black), E14/16Lys (red) and T14/16diLys (blue) monolayers on water subphase at 20 ℃ (A) and of E14/16 and E14/16Lys monolayers on water subphase at different temperatures (B).

For **E14/16** and **E14/16Lys** elasticity drops at the phase transition pressure and then rises again when the lipids organize in the LC phase. This kind of behaviour is typical for phase transitions and have been already described in literature[127]. In case of **E14/16**, apart from the elasticity drop occuring at the main phase transition, the second local minimum at around 30 mN/m can be observed. This one can be assign to the second order phase transition ($LC/LC_{t=0}$) detected also in the isotherm (change of slope of isotherm in LC phase caused by the transition of chains from the tilted to the untilted state) and by GIXD (discussed later). Comparison of the elastic properties of **E14/16** and **E14/16Lys** in the LC phase based on Fig. 35A is difficult, since the monolayer of **E14/16Lys** collapses shortly after the phase transition that is why the additional plot with elasticity calculated also for monolayers at lower temperatures (11 and 14 ℃) is presented in Fig. 35B. It is clearly seen that in LC phase, **E14/16** monolayer is more elastic than **E14/16Lys**. **E14/16Lys** has bigger headgroup and the molecules occupy more area at the interface. Moreover, its headgroups form stiff hydrogen bonding network between amino and carbonyl groups (as shown later by GIXD) what, in comparison to rigid but not interconnected **E14/16**, makes the monolayer less resistance to stress. In the ideal case, all elasticity curves of the same substance in different temperatures should meet in the LC phase. In case of **E14/16** and **E14/16Lys** the values are different, especially of 20 ℃. These deviations are due to solubility of the substance in the subphase at higher temperatures which causes a loss of the compound

from the interface and changes the slope of isotherms as a consequence. But still, all elasticity curves of **E14/16** show local minima at approximately 30 mN/m corresponding to the LC/LC$_{t=0}$ transition. As described in literature, the change of chains from the tilted the to untilted state of chains is very weakly dependent on the temperature.

3.3   INFRARED RESFLECTION ABSORPTION SPECTROSCOPY

3.3.1 Phase state (on water and DNA)

In the experiment, the combination of IRRAS with Langmuir trough with two movable barriers was used. Recording IRRA spectra at different pressures is the alternative (to Langmuir film microbalance) method which enables the determination of change of the molecular lipid monolayer structure by position of CH$_2$ symmetric, ν_s *(CH$_2$)*, and asymmetric, ν_{as} *(CH$_2$)*, stretching vibrations. The LE phase characteristic bands are around 2853 cm^{-1} and 2924 cm^{-1}, respectively, while for LC they are shifted to lower values around 2849 cm^{-1} and 2919 cm^{-1}.[76,128-130] The example spectra showing the shift of both bands during lipid monolayer compression resulting in LE/LC phase transition are presented in Fig. 11. In this experiment, the phase state of all of the three lipids along the compression isotherm at 20 °C has been checked on water and 0.1 mM ctDNA/water subphases. The positions of ν_{as}*(CH$_2$)* band in dependence of π, are shown in Fig. 36.
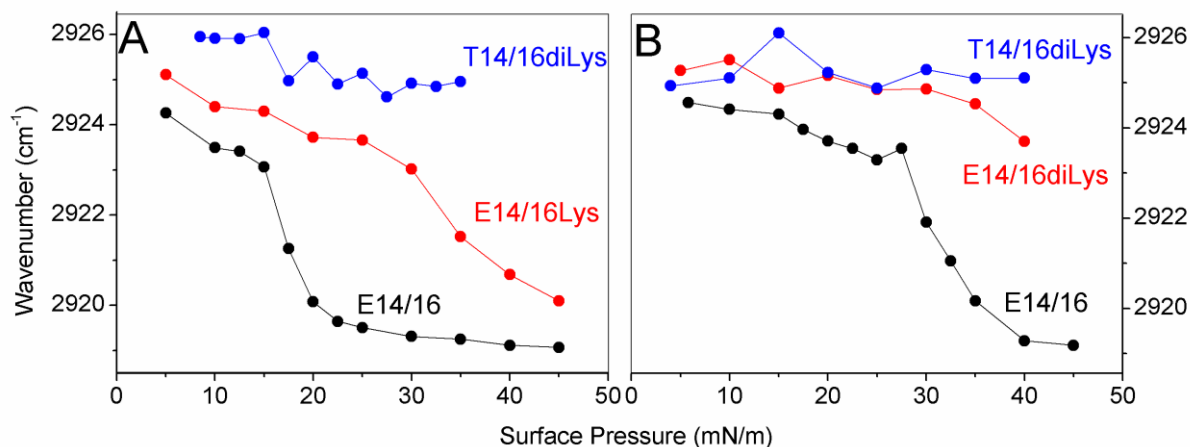

Fig. 36 The positions of ν_{as} (CH$_2$) band of E14/16, E14/16Lys and T14/16diLys on water (A) and 0.1mM ctDNA solution in water (B) along the compression isotherm at 20 °C (IRRAS).

For **E14/16** the characteristic shift of the ν_{as} *(CH$_2$)* band from ~ 2923 cm^{-1} to ~ 2919 cm^{-1} indicating the LE/LC phase transition can be clearly seen on both, water and DNA subphases. On water, the conformation of chains changes between 15 and 22.5 mN/m. The estimated phase transition pressure, $\pi = 18$ mN/m, is in a good agreement with the one determined by Langmuir isotherms (15.5 mN/m, T = 20 ^{o}C). The phase transition of the lipid on the subphase with addition of DNA is shifted to higher pressures (between 30 and 40mN/m) due to the partial incorporation of attached negatively charged DNA strands into monolayer what causes its expansion. However, the position of ν_s *(CH$_2$)* peak of **E14/16** on water and DNA become the same above 40 mN/m what indicates that DNA is squeezed out from the monolayer at higher pressures. Also **E14/16Lys** on water shows the phase transition (~ 40 mN/m) which equals the one measured by the film microbalance (39 mN/m). DNA present in the subphase drastically increases the disorder of the monolayer. Since the lipid molecule has two positive charges in the headgroup, DNA is bound much stronger than in case of **E14/16** and up to 40mN/m no DNA-squeezing out and so no phase transition can be observed. Monolayer of **T14/16diLys** is fluid in the whole range of measured pressures (0 – 40 mN/m) and the addition of DNA does not change the lipid phase state.

Results of the IRRAS experiments are in a good agreement with the film microbalance mesurments: fluidity of the monolayer increases with the headgroup size and charge. When a headgroup occupies a big in-plane area, because of steric reasons or electrostatic repulsion, it is difficult for chains to align. In this situation higher values of the –*CH$_2$* vibrations wavenumbers are expected for lipids with bigger than for lipids with smaller headgroups at the same pressures. The same applies to the phase transition. For lipids with smaller headgroups it is easier to bring the chains together so under the same conditions, less pressure has to be applied to **E14/16** than to **E14/16Lys** monolayer to reach the phase transition. In case of **T14/16diLys** it is impossible to overcome the size of the headgroup by pressure. Also the charge of a headgroups influences the fluidity of monolayers. Protonation of headgroups increases electrostatic repulsion between single molecules what additionally hinders the ordering of the lipids chains. In this study, the **T14/16diLys** that has four potentially protonable amine groups is the most fluid lipid of the three. In contrast, the chains of **E14/16**, with only one amine group in the headgroup, can relatively easy order in the *all-trans*

conformation.

3.3.2 Amount of DNA

IRRAS delivers information in the range of μm in the direction normal to the analyzed surface so substances present beneath the surface (here monolayer) in the concentration within detection limit can be seen[131]. Since DNA is the only compound with phosphate groups in all examined systems, the relative amount of DNA attached to the monolayer can be estimated by the intensity of typical symmetric, ν_s (PO_2), and asymmetric, ν_{as} (PO_2), phosphate diester bands at around 1082 cm^{-1} and 1238 cm^{-1}, respectively. DNA can be also detected by the presence of DNA the backbone band at 970 cm^{-1} [106,107]. Negatively charged DNA strands attach to lipid monolayer due to the electrostatic interactions with positively charged headgroups. Here, all cationic groups are represented by primary amines that can be protonated at low pH. Since pK_a of the new compounds is unknown, protonation state could be deducted by analogy to lipids studied elsewhere [132]. Water saturated with CO_2 has pH of approximately 6.5. Thus, theoretically, **E14/16** can have one, **E14/16Lys** two and **T14/16diLys** four charges per molecule. The amount of DNA detected in the IRRAS footprint is expected to be dependent mainly on the charge density in the headgroup region of monolayer. Fig. 36 presents the relative amount of DNA bound to one molecule of lipid at a given pressure.
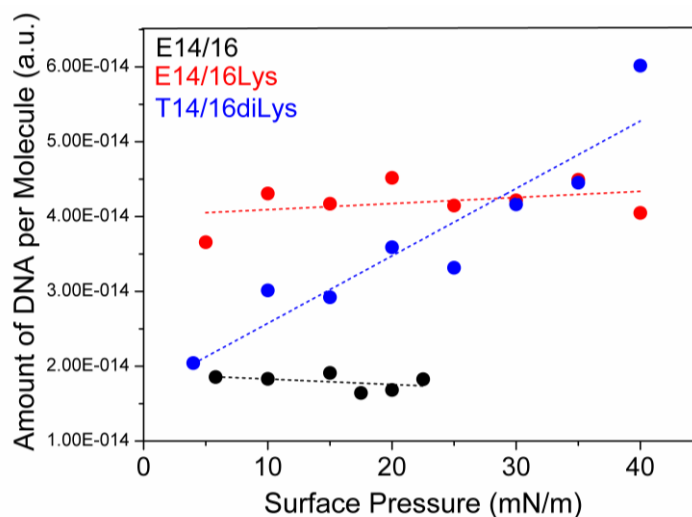

Fig. 37 Relative amount of DNA bound to E14/16, E14/16Lys and T14/16diLys monolayers spread on 0.1mM ctDNA solution in water (IRRAS).

To determine this dependency, the number of molecules in IRRAS footprint (2 mm^2) has been calculated using the area per molecule at a given pressure from the corresponding isotherm (only for the LE phases, since DNA fluidizes monolayers). Next, the intensity of phosphate bands has been divided by the number of molecules for each measured pressure. As seen in the plot, for lower pressures **E14/16Lys** binds higher amount of DNA than the two other lipids. At the same time the value is more or less stable for **E14/16** and **E14/16Lys** over all pressures range what means that DNA is strongly attached and moves along with the lipid molecules while compressing. No squeezing out for **E14/16** deduced from the phase state can be observed here so probably DNA strands are removed from the monolayer but still crowd under it. Moreover, approximately two times more DNA is attached to **E14/16Lys** than to **E14/16** what could be expected since **E14/16Lys** has two times more charges per molecule. Even though the exact percentage of charged groups is unknown, the ratio between **E14/16** and **E14/16Lys** is constant at all pressures. The situation is different for **T14/16diLys**, where the amount of DNA increases linearly with pressure, to reach values equal or higher than for **E14/16Lys** at pressures above 30 mN/m. If the ratio between protonated amino groups was constant, then the amount of DNA would be four times higher than for **E14/16** and two times higher than for **E14/16Lys**. But this is not the case. It could be that not all of amino groups of **T14/16diLys** are charged at a given pH and the protonation increases during compression. Different protonation degrees for different phases of the same monolayer have been observed before but usually number of charges decreases with increasing packing density of the monolayer [132]. The other possibility is that independently on the charge, the area per headgroup is not big enough to fit two times more DNA than in case of **E14/16Lys**. Upon compression the conformation of headgroups changes and allows DNA to attach in bigger number. Nevertheless, **T14/16diLys** has been found the most effective for the gene transfection among the three lipids so it is clear that effectiveness is not a linear function of the amount of DNA attached to the complex but depends also on other factors.

3.4 GRAZING INCIDENCE X-RAY DIFFRACTION

GIXD is a powerful tool to study chain packing of lipids monolayers in condensed phases at the air-water interface. X-ray diffraction pattern gives information about dimensions of chain lattice unit cell, its distortion (d), tilt angle of chains (t) and cross-sectional area of chains (A_0) [80]. **E14/16** and **E14/16Lys** were studied at pressures above their LE/LC phase transitions pressure on water subphase at 10 and 5°C respectively. **T14/16diLys** does not diffract X-rays since it does not form a gel phase under the analyzed conditions. Fig. 38 shows selected contour plots of GIXD intensities as a function of the in-plane (Q_{xy}) and the out-of-plane (Q_z) scattering vector components in various surface pressures. Maxima of Q_{xy} and Q_z peaks, values of d, t, A_0 and correlation lengths (L_{xy} and L_z) of both lipids are summarized in Table 3.
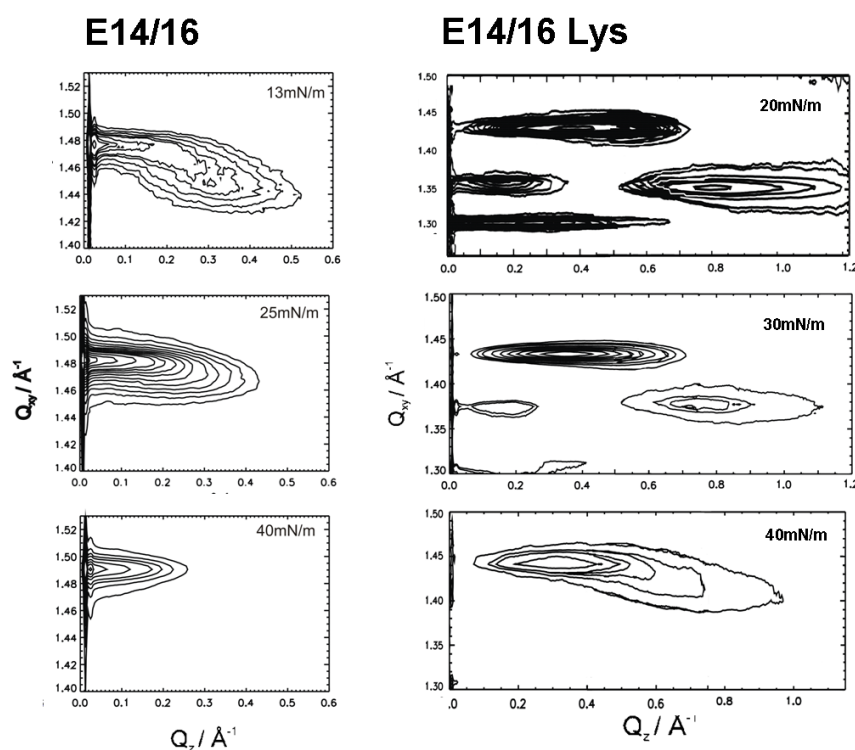
Fig. 38 Contour plots of GIXD intensities as a function of the in-plane scattering vector component Q_{xy} and the out-of-plane scattering vector component Q_z of monolayers of lipids spread on water: E14/16 at 10 °C (at 20, 30 and 40 mN/m) and E14/16Lys at 5 °C (at 13, 25 and 40mN/m).

The contour plot of **E14/16** at lower pressures (13 mN/m) presents two resolved peaks (Fig. 38). One of the peaks is located in the water plane ($Q_z = 0$, non-degenerated peak) while the second can be observed at higher Q_z and lower Q_{xy} values (degenerated peak). Such positions of peaks are characteristic for a distorted towards nearest neighbor (NN)

centered rectangular chain lattice with NN-tilted chains [99]. Upon further compression, the degenerated peak moves to smaller Q_z values what indicates a decrease of aliphatic chains tilt and of the unit cell distortion. At 30 mN/m the peaks are still slightly resolved while at 40 mN/m their positions coincide giving one well defined peak in the water plane which corresponds to the untilted and not distorted hexagonal phase. The determined by GIXD pressure of the transition from the tilted to the untilted phase (32.7 mN/m, described later in the text) is in a satisfying agreement with the one obtained from the **E14/16** Langmuir isotherm at 11 ºC where characteristic a kink being a change of slope was observed at pressure of 26 mN/m. **E14/16Lys** contour plot at 20 mN/m exhibit four well resolved peaks where only two are considered to be corresponding to the aliphatic chain lattice: at Q_z = 0.396 Å^{-1} (degenerated) and Q_z = 0.815 Å^{-1} (non-degenerated). A peak at the same Q_{xy} value as the non-degenerated one is an effect of signal intensity modulation and does not correspond to any structure. A peak at Q_{xy} = 1.3 Å^{-1} is characteristic for hydrogen bonds that can be formed between the lipid head-groups. Even though **E14/16** headgroups also have moieties that can form hydrogen bonds (primary amines, amides and carbonyl groups) the hydrogen bond peak was not observed and it is due to the different head-group structure and its steric alignment. For **E14/16Lys**, the hydrogen bond peak does not change its position with increasing surface pressure, since its length is well defined and fixed for a given type of interaction. Although, the intensity of the peak decreases due to the hydrogen bonds break caused by compression. Location of the degenerated and non-degenerated peaks indicates the centered rectangular lattice distorted towards next nearest neighbor (NNN) with the NNN-tilted chains. As shown in contour plots, while increasing the pressure both peaks decrease the distance between each other and move in the direction of smaller Q_z values what indicates a decrease of lipids chain tilt angle and the unit cell distortion. Up to surface pressure of 40 mN/m no transformation into the non-tilted hexagonal phase can be observed. The theoretical phase transition from the tilted to the untilted phase, $\pi_{t'}$, can be calculated assuming that along the isotherm the molecular area (A_{xy}) depends linearly on the surface pressure and the cross-sectional area A_0 is constant. The extrapolation of π plotted versus *1/cos(t)* towards zero tilt angle *(1/cos(t) = 1)* yields the theoretical $\pi_{t'}$ (Fig. 39A) [101]. For **E14/16**, $\pi_{t'}$ = 32.7 mN/m and for **E14/16Lys** $\pi_{t'}$ = 77.7 mN/m. The obtained $\pi_{t'}$ of **E14/16** stays in a good agreement

with the experimental data, where the untilted phase has been reached between 30 and 40 mN/m. In the case of **E14/16Lys**, the theoretical pressure is impossible to obtain before monolayer collapse.
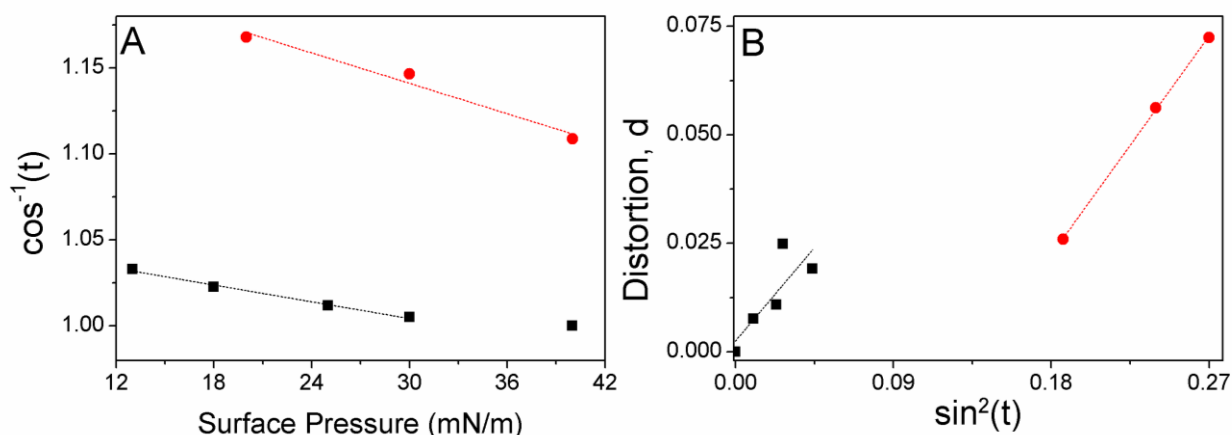

Fig. 39 A: Plot of $\cos^{-1}(t)$ versus surface pressure for lipids monolayers spread on water, E14/16 at 10 °C (black squares) and E14/16Lys at 5 °C (red circles), with linear fits. The point at the highest surface pressure for E14/16 has not been taken into account for a fit because it is already at $\cos^{-1}(t) = 1$; B: Lattice distortion of the lipids monolayers spread on water as a function of *sin* of the tilt angle, *t*: E14/16 at 10 °C (black squares) and E14/16Lys at 5 °C (red circles) with linear fits.

As expected from the isotherm, the in-plane areas A_{xy} (a real area at the interface occupied by chain) are larger for **E14/16Lys** (e.g. 22.9 Å^2 at 30 mN/m) than for **E14/16** (e.g. 20.8 Å^2 at 30 mN/m) and it is due to a bigger headgroup size and consequently bigger tilt of chains. At the same time, cross-section area of a single chain (A_0) of **E14/16** is bigger than A_0 of **E14/16Lys** and equals to 20.7 Å^2 and 19.9 Å^2, respectively. The headgroups of **E14/16Lys** are linked with each other via hydrogen bonds what increases the rigidity of a monolayer and at the same time limits free rotation of chains. On the other hand, ν_{as} *(CH$_2$)* wavenumbers for **E14/16** in the LC phase determined by IRRAS are around 2919 cm^{-1} what is typical for freely rotating chains of LC phase with A_0 around 20 – 20.6 Å^2 and at the same time ν_{as} *(CH$_2$)* in LC phase of **E14/16Lys** are around 2921 cm^{-1} what indicates that the chains are slightly less packed and there is a certain percentage of LE phase in the monolayer. According to IRRAS, **E14/16Lys** would be expected to have bigger A_0. But on the other hand, GIXD detects only chains in LC phase so the share of LE should not matter for the measurement. According to the Landau theory of phase transition in Langmuir monolayers [102], dependence *d = f(sin^{2}t)* should be linear what is true for both examined lipids (Fig. 39B). If only the tilt of chains causes

the unit cell distortion, the extrapolation of the linear fit to d_0 ($d = 0$) is reached at $sin^2 t = 0$. In this case this condition is met for **E14/16**. For **E14/16Lys** $d_0 \neq 0$ what indicates that not only the tilt but also other things like hydrogen bonds that cause differences in lipids chain packing, may influence the distortion. The thickness of both lipids monolayers (L_z) understood as a length of a single chain organized in crystalline-like structures above the water surface was also calculated. L_z values for both lipids differ even though they represent the same chain length and structure. L_z equals to 17 Å and 15 Å for E14/16 and E14/16Lys, respectively. Both values are smaller than theoretical length of chains ($\sim$ 20 Å). The difference in the lengths obtained from GIXD can be caused by the fact, that only crystalline-like organized structures with repetitive distances can be seen by GIXD. Both aliphatic chains of analyzed lipids are linked to the same carbon atom. Most probably this is a steric barrier for the few first methylene groups to align regularly so in the case of **E14/16** GIXD can detect only around 12 – 13 C long chain. Bigger head-group of **E14/16Lys** and its higher positive charge leads to the expansion of the monolayer so, in comparison to **E14/16**, the chains of **E14/16Lys** are more loosely packed. Due to that interactions between chains are weaker and shorter part of the molecule is well organized (around 10-11C).

Table 3 Bragg Peaks (Q_{xy}) and Bragg rods (Q_z) maxima, corresponding to them correlation lengths (L_{xy} and L_z), tilt angle (t), distortion (d) and cross-section area (A_0) of E14/16 and E14/16Lys monolayers at different surface pressures (π) (where the superscript *d* means degenerated and *n-d*, non-degenerated peak).

	π [mN/m]	Q_{xy}^d [Å^{-1}]	L_{xy}^d [Å]	Q_{xy}^{n-d} [Å^{-1}]	L_{xy}^{n-d} [Å]	Q_z^d [Å^{-1}]	L_z [Å]	Q_z^{n-d} [Å^{-1}]	L_z [Å]	t [°]	d	A_0 [Å^2]
E14/16 on water 10°C	13	1.447	118	1.474	325	0.323	17	0	16.8	14.5	0.025	20.8
	18	1.457	122	1.478	351	0.285	17	0	17	12.1	0.019	20.7
	25	1.470	156	1.482	492	0.196	17	0	17	8.8	0.011	20.7
	30	1.476	115	1.485	492	0.130	17	0	17	5.8	0.008	20.7
	40	-	-	1.490	346	-	-	0		0	0	20.5
E14/16Lys on water 5°C	20	1.429	552	1.354	291	0.396	15	0.815	15	31.1	0.072	19.9
	30	1.433	195	1.373	552	0.383	14	0.770	14	29.3	0.056	19.9
	40	1.442	250	1.414	203	0.340	14	0.676	14	25.6	0.026	20.0

3. CONCLUSIONS

The three newly synthesized lipids designed for gene transfection, **E14/16**, **E14/16Lys** and **T14/16diLys** were investigated in order to improve knowledge of transfection efficiency/cationic lipid structure correlation with special emphasis put on the importance of the headgroup structure. In this study their monolayer properties at the air-water interface have been investigated using the Langmuir trough in combination with Infrared Reflection-Absorption Spectroscopy (IRRAS) and Grazing Incidence X-ray Diffraction (GIXD). The two dimensional binding of these monolayers with model DNA dissolved in the water subphase has been also investigated by quantifying the amount of DNA attached to a monolayer using IRRAS. Also the transfection efficiency in formulations of the lipids with helper lipid, DOPE, has been check in comparison to commercially available Lipofectamine™ (data not shown). All lipids show different structures and affinity to DNA due to different size and charge of the headgroup. Monolayer of the lipid with the biggest headgroup and highest charge, **T14/16diLys**, is fluid, while the other two, **E14/16** and **E14/16Lys,** remain fluid only up to the certain pressure and then undergo the first order phase transition (LE/LC) to a gel phase. **E14/16Lys**, the second lipid by size and possible charge of the headgroup and second by fluidity, cannot though reach the non-tilted state and **E14/16** reaches it already at pressures close to 30 mN/m. As expected, the most fluid and most charged lipid, **T14/16diLys** is the best transfection agent while **E14/16** shows the lowest efficiency (data not shown). Nonetheless, for Hep-G2, the cell line used for the transfection experiment, all lipids perform better than lipofectamine with significant improvement in the case of **T14/16diLys**. However, the transfection efficiency cannot be easily correlated with the amount of DNA that attaches to the lipid organized in a monolayer at the air/water interface, where up to pressure of 25 mN/m the highest amount of nucleic acid is bound to **E14/16Lys**. At 30 mN/m, that is the pressure in layers building a liposome, the amount of attached DNA is equal for **E14/16Lys** and **T14/16diLys**. Summarizing, the transfection efficiency in a given set of lipids increases with the fluidity of lipids and fluidity increases with the size of the headgroup and number of possible charges.

Supporting Information can be found in the appendix. The phase transition observed by BAM is shown.

CHAPTER 3

THE INFLUENCE OF CHAIN STRUCTURE ON THE PHYSICAL-CHEMICAL PROPERTIES AND TRANSFECTION EFFICIENCY

---

1. INTRODUCTION

The structure of a lipid molecule used to form a nucleic acid carrier system is one of the most important factors that influences gene delivery efficiency. There is a huge variety of lipids that has been designed and synthesized as DNA or RNA vectors. All of the lipids, though, consist of a hydrophilic headgroup, nonpolar domain (tail) and a linker connecting those two. A headgroup is usually positively charged. In the majority of cases the charge is introduced by amino groups that can be protonated at given pH conditions. The most common linker groups are amino acids, or moieties consisting of ether or ester bonds. Hydrophobic domains can be composed of steroids or hydrocarbon chains. Though transfection efficiency is considered to be a function of a good balance of all of the lipid structure components, it is very difficult to separate the importance of each of them. This chapter focuses particularly on the influence of the hydrophobic chain. Steroid groups are not of concern. The general structure – function relationship for gene transfectants has been described in the introduction of this work.

The first important property of the chain structure is its length. The lengths of lipid chains synthesized for transfection vary considerably. The use of 25C as well as 5C long tails has been reported. Nevertheless, the most common lengths are C12 to C18. Very short chains fluidize the lipid membrane, which improves the fusogenic properties when it comes to interaction with the cellular membrane, but at the same time decrease the liposome stability. On the other hand, chains that are too long due to their rigidity do not tend to form liposomes which are used for lipoplex formation. The majority of lipids used for transfection have two aliphatic chains. Their one-, three- or more-chain analogues are more likely to form micelles and are more toxic due to their surfactant character. However, there are a lot of reports describing one- or three-tailed lipids that have been successfully used for transfection experiments in-vivo. Also, the chain saturation plays a big role in transfection performance [133]. It has been known that

unsaturated chains increase membrane fluidity by the disturbance of chain alignment and therefore enhance the fusion of the lipoplex with the cellular membrane. Fluid membranes are also less stable than the more rigid ones what enables DNA release from the lipoplex. Very fluid membranes though, which are usually formed by relatively short unsaturated, are much less suitable for storage due to the ease of oxidation. Moreover, some rigidity is needed for the liposome stabilization [47]. Both, *cis* and *trans* isomers have been studied in means of transfection efficiency and research in favor of both can be found. So far no pronounced tendency can be enunciated. However, as reported by many researchers, the presence of *cis*-oleyl chain (C 18:1) in a given lipid usually enhances the transfection efficacy significantly [23,24,134].

In this study two lipids with the same headgroup but different chain pattern have been examined. One, **TT10**, has two saturated tetradecyl chains (14:0, 14:0) and is of analytical purity. The second, **TO10**, has one tetradecyl and one oleyl chain (14:0; 18:1) and consists of 25 mol% of different lipids of the same headgroup and one chain (14:0) and differing with the structure of the other chain. The "impurities" of TO system come from the commercially available oleylamine used for the synthesis. The synthesis has been described in detail by Woelk [119]. The chemical structures of the lipids are shown in Fig. 40. The influence of the small difference in the structure of the two chains will be checked. As mentioned in Chapter 1, also the purity of the lipid may have the influence on its physical- chemical properties and transfection performance, so this factor will be also taken into account.

2. EXPERIMENTAL DETAILS

The experimental details have been described in chapter "Experimental details" at the end of the text.

Materials

The **TT10** and **TO10** lipids have been synthesized by Woelk as described earlier [119]. **TT10** is a compound of analytical purity and **TO10** has been synthesized from commercially available oleylamine (Sigma-Aldrich) and due to the purity of this compound **TO10** consists of other lipids with the same headgroup pattern and C14:0 chain but differing in the other chain structure (C18:1 - 81 mol%, C18:0 - 6 mol%, C16:0 - 10 mol% C14:0 3mol%). For all inorganic solutions, the MiliQ water of 18.2 mΩ was used. 5 mM citric buffer was used for experiments at pH 4 and 5 mM carbonate buffer was used for experiments at pH 10. Sodium salt of deoxyribonucleic acid from calf thymus (in the text refered as ctDNA) was purchased from Sigma-Aldrich and used as 0.1 mM solution in MiliQ water. 1,2-dioleoyl-*sn*-glycero-3-phosphoethanolamine (DOPE) was purchased from Avanti Polar Lipids. For monolayer experiments, the lipids were dissolved in 3: 1 chloroform: methanol solvent. Methanol and chloroform were purchased from Sigma-Aldrich and used without further purification.
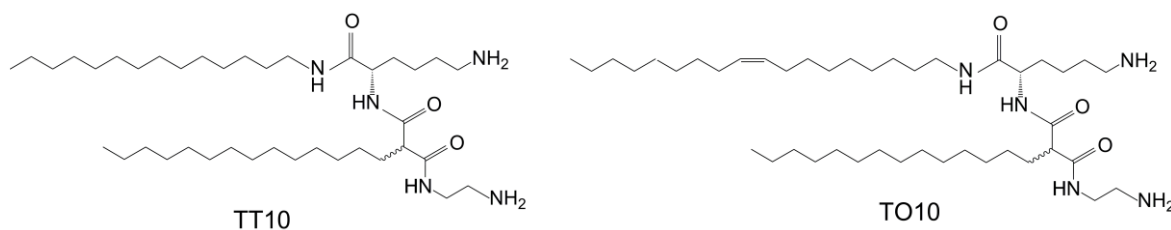

Fig. 40   Chemical structures of TT10 and TO10.

3. RESULTS OF DISCUSSION

3.1 LANGMUIR ISOTHERMS

The Langmuir pressure-area isotherms provide basic information about amphiphiles monolayer phase state. Fig. 41 shows Langmuir isotherms of **TT10** and **TO10** monolayers spread on water and buffers of pH 10 (carbonate buffer) and pH 4 (citrate buffer) at 20 °C and 5 °C. **TT10** has almost equal areas per molecule on water and pH 10 and behaves as a typical condensed monolayer (areas per molecule < 55 Å^2, high slope). The similarity between isotherms on water and pH 10 can be also observed for **TO10** with the shift of areas to larger values typical for coexistence of condensed and expanded phase. **TO10** has one double bond in one of the chains what is known to increase the fluidity of the monolayer. It seems that for both lipids their charge at CO_2 saturated water of pH ~6.5 is similar to one at pH 10. The design of the lipids allows controlling the charge of their headgroups by the protonation of primary amine moieties at different pHs of the environment (see Fig. 40 for the structure). In completely deprotonated state lipid molecules can come close together so the phase state at higher pHs is more condensed while at low pH values amino groups gain a charge what causes electrostatic repulsion between the headgroups and leads to the monolayer expansion. That is why at pH 4, when most of amino groups are protonated, the slope of the isotherm of both lipids gets smaller and the area per molecule grows drastically to the values typical for a liquid expanded phase (higher than 100 Å^2 at the beginning of the isotherm). Moreover, at pH 4 amines loose their ability for hydrogen bonds formation which are known as additional stiffeners of monolayers. For **TO10** the area changes continuously up to very high pressures and the exact pressure of the monolayer collapse cannot be easily defined. It is very difficult especially at 20 °C where the isotherm slope is very low. It can be an effect of a high solubility of **TO10** in these conditions of the temperature and pH. In this case, upon loss of material, the presented areas per molecule are not real values since less substance than expected is forming the monolayer. The isotherm at 5 °C is typical for an expanded phase with the high collapse pressure of 65 mN/m (not shown). **TO10** does not perform the phase transition in any of measured conditions. By contrast, **TT10** at pH 4 undergoes the phase transition from expanded to condensed phase. At 5 °C there are two phase transitions, the first at about

15 mN/m and the second at about 30 mN/m. The phenomenon is really interesting and indicates presence of two different species or two different types of transitions in the same monocomponent monolayer. The answer can come only from **TT10** structure. It is possible that at lower pHs the headgroups of all molecules in the monolayer are not equally protonated – some have two protonated amino groups and some only one charge. These two species may have different transition pressure, more protonated at higher and less protonated at lower pressure. It is interesting that at 20 °C only one phase transition can be seen (π_{tr} = 52 mN/m). Probably at this temperature protonation of molecules is more equal or the two species mix with each other better and the transitions cannot be distinguished anymore. Despite the same structure of the headgroup, **TO10** does not show this effect, since the double bond fluidizes the layer.
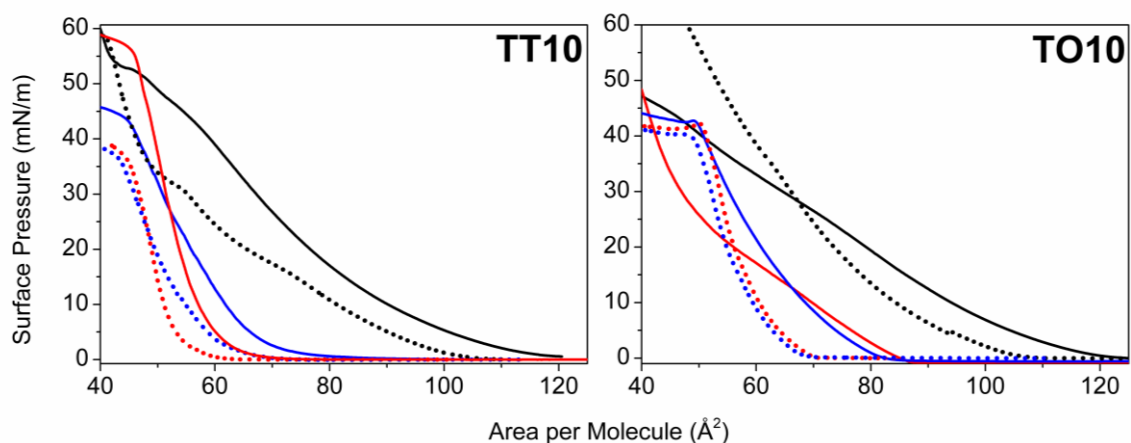

Fig. 41 Langmuir isotherms of TT10 (left panel) and TO10 (right panel) at pH 4 at 20 °C (black solid line) and 5 °C (black dotted line), water at 20 °C (red solid line) and 5 °C (red dotted line) and pH 10 at 20 °C (blue solid line) and 5 °C (blue dotted line).

3.2 INFRARED REFECTION ABSORPTION SPECTROSCOPY

3.2.1 On buffers

In this experiment a phase state of the two lipids on different subphases has been checked. The **TT10** and **TO10** monolayers have been spread on MiliQ water, pH 10 (carbonate buffer), pH 4 (citrate buffer) and 0.1 mM solution of ctDNA in water. Then the monolayer was compressed along the isotherm and at given pressures the spectra were taken. The results, the positions of ν_{as} (CH$_2$) band in dependence of π, are shown in Fig. 42.
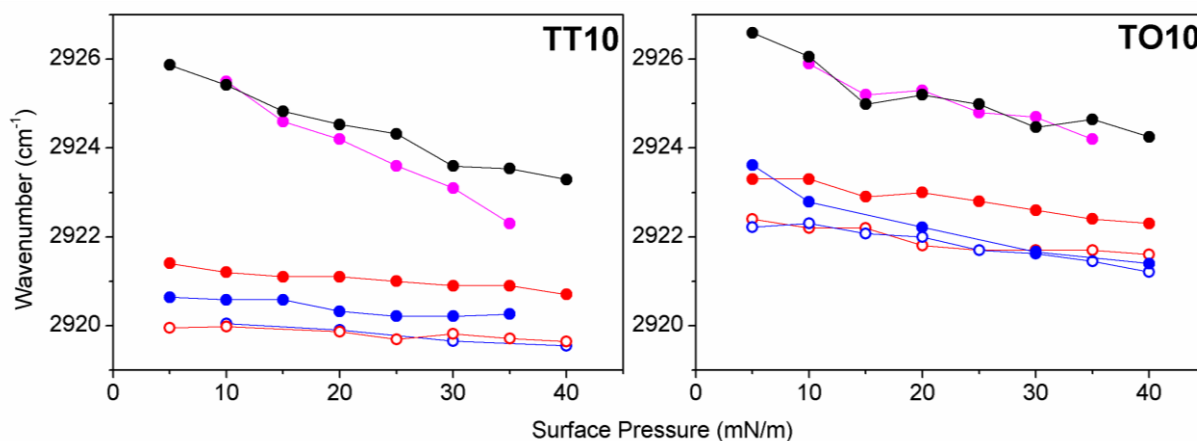
Fig. 42   The positions of $\nu_{as}(CH_2)$ band of TT10 (left panel) and TO10 (right panel) at pH 4 at 20 °C (black full circles), water at 20 °C (red full circles) and 5 °C (red empty circles), pH 10 at 20 °C (blue full circles) and 5 °C (blue empty circles) and 0.1mM ctDNA solution in water (pink) along the compression isotherms. Lines are for eye guidance only.

As can be seen in the figure, the wavenumbers of **TT10** at the same conditions are lower than for **TO10**, what means that chains of lipid **TT10** have less space for free vibrations what indicates closer packing. Nevertheless, the wavenumbers at 20 °C are above 2920 cm^{-1} what means that not all chains are packed in all-trans conformation and there is a certain amount of fluid chains. This is in a good agreement with the isotherms measured under the same conditions. The fact, that the fluidity of **TO10** is higher than for **TT10** was expected, since double bond in the chain is known as one of factors that increase fluidity due to steric reasons. At 20 °C for both lipids, the wavenumbers at pH 4 are the highest and the lowest at pH 10. This observation can be explained by the controlled charge of lipid headgroups that varies in dependence of pH. At low pH, primary amino groups are protonated and they loose their charge at pH higher than 8 (data not shown). Charged headgroups repulse each other what causes expansion of the monolayer. Moreover protonated amino groups loose their ability for hydrogen bond formation, that can connect neighboring molecules and additionally stiffen the monolayer at higher pHs. Temperature also influences the phase state of lipids in the monolayer. For presented measurements it is clear that on water, as well as on pH 10, both monolayers are more condensed at 5 °C than at 20 °C. What is interesting, is that at 5 °C it does not matter if the monolayer is spread on water (pH ~ 6.5) or on buffer of pH 10, vawenumbers and so the average fluidity are the same. It is possible that at low temperature pH of CO_2 saturated water is already enough to maximally deprotonate amino groups of the headgroups. At pH 4 both lipids remain fluid in the measured range

of pH (we cannot observe the **TT10** phase transition present in isotherm at π = 52 mN/m). The IRRAS data are in a good agreement with results obtained with Langmuir film microbalance.

3.2.2 On DNA

Phase state: Addition of DNA to the subphase increases the monolayers fluidity. At 20 °C on 0.1 mM solution of ctDNA in water, the phase state of both lipids is almost the same as at pH 4. The reason for the expansion is the attachment of negatively charged DNA strands to the partially protonated headgroups of the lipids. Strands do not only bind but also partially incorporate in between lipid molecules and occupy some area at the air-water interface separating lipid chains and not allowing them to align. It seems that in case of **TT10**, under growing pressure DNA is being squeezed out from the monolayer - the wavenumbers are decreasing (more lipid molecules can align).

DNA quantification: Since DNA is the only molecule in the system that contains phosphate groups, the relative amount of DNA could be calculated by the integration of symmetric, ν_s (PO_2), and asymmetric , ν_{as} (PO_2), phosphate diester bands at around 1082 cm^{-1} and 1238 cm^{-1}, respectively. Presence of DNA can be also detected by the characteristic DNA backbone band at 970 cm^{-1}, which is at the very end of the measured range and the results obtained by the intensity integration of this band can be erroneous. Fig. 43 shows the relative amount of the attached DNA to both, **TT10** and **TO10** monolayers.
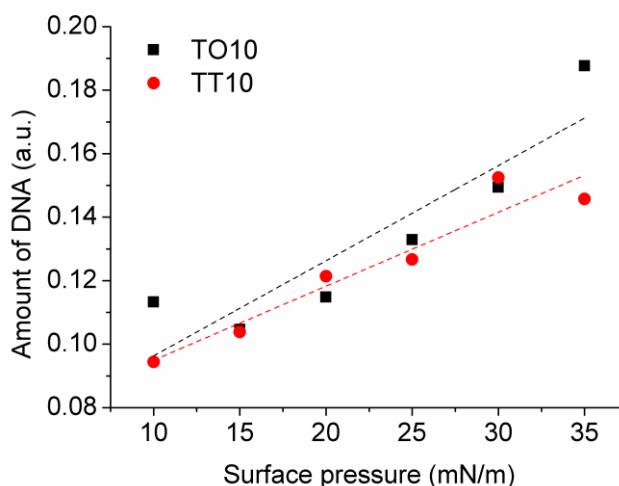

Fig. 43 The relative amount of DNA attached to TO10 (black) and TT10 (red) monolayer spread on 0.1 mM ctDNA in water and the linear fits to data points.

As shown, the calculated values are almost identical for both lipids in the same conditions. Even for **TT10** at high pressures, when DNA squeezing out appears, the amount of the DNA seems to grow with surface pressure, what means that in spite of lack of space at the interface DNA molecules crowd underneath the lipid. A clear conclusion can be made from the experiment - the headgroup structure and its charge is the most important factor for the DNA attachment. The initial phase state and chains configuration do not play a big role in the process, since DNA fluidizes the chains and at the moment of the measurement **TO10** as well as **TT10** are in the same state.

3.3 GRAZING INCIDENCE X-RAY DIFFRACTION

TT10 have been examined by GIXD at pH 4, on water and at pH 10. Due to the fluid character of **TO10,** the method was not used for the lipid investigation. For all measurements the monolayers have been compressed to the surface pressure of 10 mN/m. To keep the films stability, the measurements were performed at 5 °C. The chain lattice unit cell parameters, like shape, dimensions and distortion have been obtained. Also the chain tilt angle and its cross-section area were calculated.

TT10 at pH 10 and on water shows very complicated pattern consisting of many reflexes (Fig. 44). As for IRRAS and Langmuir microbalance, the results for the two environments look alike since most probably the protonation of lipids headgroup is very similar at pH 10 and on water. That is why the figure shows only the pattern at pH 10.
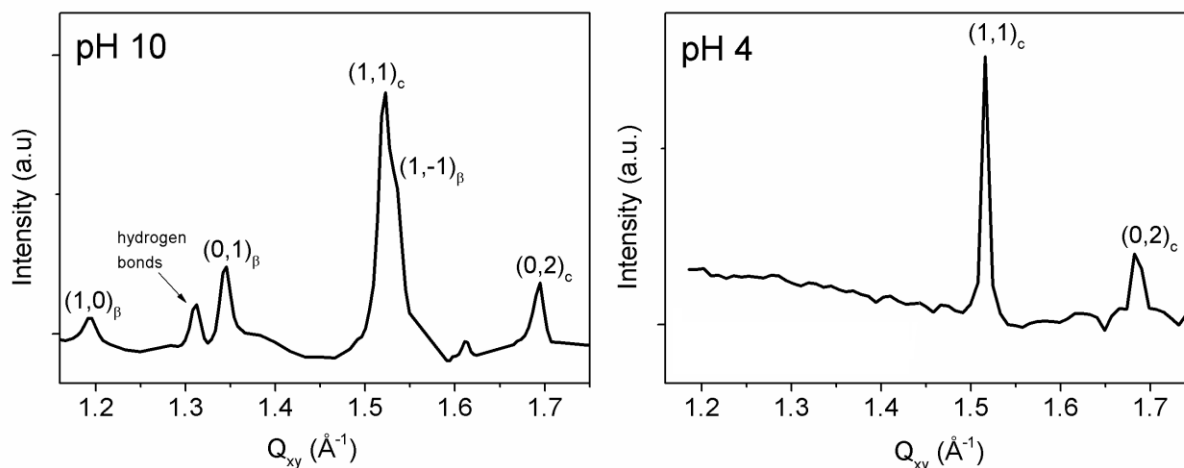

Fig. 44 GIXD pattern of TT10 spread onto buffer of pH 10 and pH 4. Bragg peaks indicated with β subscript belong to the monolayer lattice and marked with C come from lipid TT10 crystal diffraction. Not indexed small peak at $Q_{xy}=1.62$ Å^{-1} at pH 10 is an artifact.

Careful analysis of the width of obtained Bragg rods of **TT10** at pH 10 and water led to division of the reflexes into two groups: Bragg rods with FWHM values of 0.3 Å^{-1} which belong to the lipid chain lattice (indicated by β in the figure) and Bragg rods of FWHM = 0.17 Å^{-1} (indicated by C in the figure). The significantly lower width indicates that apart from the chain lattice, there must be other repeating distance of much higher length. If one uses Sherrer formula [L_z=0.88(2π/ FWHM)] to calculate the length of the molecule contributing to the signal, the first group of peaks will give the lengths of 15 Å. **TT10** has 14C in each chain. The theoretical length of the single 14C chain is equal 13*1.26 Å $_{(for}$ $_{trans\ -CH2)}$ + 1.54 Å $_{(for\ -CH3)}$ = 18 Å [105]. The obtained value of 15 Å is relatively low in comparison to theoretical value, but still acceptable since methylene groups may start ordering just in some distance from the headgroup. L_z calculated for the second group of Bragg rods with FWHM of 0.17 Å^{-1} is equal 32.5 Å and is too high for the lipid molecule length. The high value of L_z indicates that the source of the scattering is a thicker layer. There are several possible explanations. The first is to assume that the chain lattice is a sublattice of the superlattice formed by, for example, headgroup ordering. This theory can be proved only by finding a lattice in the frame of which all Bragg peaks could be indexed. However the indexing of all peaks within one network was not possible. According to the second theory, there are completely different specie not related anyhow to the lipid layer, as salt, that could crystallize under the lipid film template, as reported many times earlier [135]. But in this case the monolayer spread on highly pure water should not give any other reflexes that the ones belonging to the chain lattice and the pattern from lipids on MiliQ water looks almost identically with the one of the lipid spread on the buffer subphase (NaHCO$_3$/ Na$_2$CO$_3$). The third theory is the assumption that the lipid was not completely dissolved in the solution (it was spread from chloroform/ methanol 3:1). In this case microcrystals of lipid may have been present at the surface and diffracted X-rays. The crystals are most probably made of lipid layers and double layers. Since GIXD is sensitive to the in-plane structure, it is impossible to estimate the numbers of layers in a crystal contributing to the signal. Since we do not see the Scherrer rings or any bending of contour plots, the signal have to come from oriented crystals (that give spots like signal) rather than from a powder like structure (where the rings are expected). Probably only the in-plane cross-section of the double layer can be seen so no 3D structures contribute to the signal. Presence of crystals is the

most reasonable explanation so it was assumed that the peaks that do not belong to the chain lattice arise from the in-plane lattice of lipid multilayers.

Following this theory, all peaks observed for **TT10** at pH 10 and water were divided into two groups: indexed chain lattice peaks (1,-1), (1,0) and (1,1) plus hydrogen bond peak and two peaks of the crystal (2,0) and (1,1).

The chain lattice is described by three peaks (Fig. 44) what indicates oblique shape of a unit cell. The distortion of the unit cell calculated from peaks Q_{xy} values equals 0.3. According to the rules of symmetry there are some dependencies between parameters that must be full-filled. The first is that all Bragg rods (describes by Q_z) belonging to the same lattice must have the same FWHM. In this case it is equal to 0.3 Å^{-1} and corresponds to the L_z of 15 Å (explained earlier in the text). The relationship between Q_z values, $Q_{z1} + Q_{z2} = Q_{z3}$ (where Q_{z1} is the lowest and Q_{z3} the highest value) is also full-filled. The obtained tilt angle of chains equals to 39.4°. The relatively large tilt is in agreement with quite high wavenumbers ($\sim$ 2920 cm^{-1}) of **TT10** at pH 10 in the LC phase measured by IRRAS (expected values for *all-trans* chains are in the range of 2918 - 2919 cm^{-1} and the observed ones are slightly above these values). Tilted chains have more freedom for vibrations than the ones standing up-right so wavenumbers increase slightly with the tilt. The area per chain, A_o, determined with GIXD is also a bit higher than typical free rotating chain area ($\sim$19-20 Å^2) and equals 20.7 Å^2 what is also characteristic for strongly tilted chains since they occupy more space while rotating. The in-plane area A_{xy} = 25.6 Å^2, that describes the real in-plane area occupied by one chain at the surface, is consistent with the area per molecule determined by Langmuir isotherm: area per molecule at pH 10 and 10 mN/m equals 54 Å^2 what gives 27 Å^2 per chain. Since areas measured by isotherms are averaged over the whole monolayer surface (with possible packing defects) they are usually slightly higher, never smaller, than the ones measured by GIXD that gives only the values of the well-ordered parts. Apart from the three peaks of the **TT10** chain unit cell, there is also the hydrogen bond peak at characteristic Q_{xy} = 1.31 Å^{-1} and Q_z = 0 Å^{-1} corresponding to d = 4.8 Å. The hydrogen bonds can be formed in the headgroup area between amino and carbonyl groups, what leads to additional packing constrains for the chains.

The other two peaks at Q_z = 0 Å^{-1} and Q_{xy} = 1.52 Å^{-1} (degenerated peak) and Q_{xy} = 1.69 Å^{-1} (non-degenerated peak) have been assigned to the lipid crystal reflection (see Fig. 44).

Two peaks are a sign of the rectangular unit cell. Both of the peaks are laying at the horizon what denotes lattice of non-tilted chains. The calculated distortion of the cell equals 0.15. The two Bragg rods have the same FWHM = 0.17 Å^{-1} and the calculated from this value length of the diffraction unit is 32.5 Å what corresponds to interdigitated chains of two layers. Since they are interdigitated, they are not tilted and have no rotation freedom so A_0 is very small (~18.5 Å^2). Such small area per chain and calculated dimensions of the chain unit cell point to the herringbone chain packing mode. The lack of the rotation freedom cannot be seen by IRRAS because the free rotating *all-trans* chains of the monolayer are in huge excess to the microcrystals.

The GIXD pattern of **TT10** on water has been resolved in the same way. Since values are very similar, they have not been described here.

The signal of **TT10** changes significantly at the surface of pH 4 (citrate buffer). The chain lattice and hydrogen bond peaks disappear and only the crystal reflexes at the exact same positions as for pH 10 (1.52, 0) and (1.69, 0), can be seen. At pH 4 primary amino groups of the headgroups gain charge what precludes hydrogen bonds formation. Moreover, protonated headgroups repulse each other what causes expansion of the monolayer and only LC phases can be examined with GIXD. However, the pH does not influence the crystal structure that much since the buffer only surrounds them but does not penetrate inside layers.

3.4 SMALL AND WIDE ANGLE X-RAY SCATTERING

TT10 and **TO10** have been examined with SAXS in form of suspensions: in buffers of pH 10 and pH 4 and water. Since the lipids have been designed as carriers of DNA in various complexes with helper lipids and genetic material, further also their mixes with DOPE as well as DOPE and ctDNA in water have been investigated.

3.4.1 SAXS of the pure lipids at pH 10, water and pH 4

Fig. 46 shows SAXS pattern of 20 wt% of lipids **TT10** and **TO10** in buffers of different pHs and water.

At pH 10 both lipids show two reflexes in characteristic ratio s_1: s_2 of 1: 2 what points to the lamellar phase (**TT10**: s_1= 0.0195 Å^{-1}, s_2 = 0.0387 Å^{-1} and **TO10**: s_1= 0.0190 Å^{-1}, s_2 = 0.0380 Å^{-1}). The characteristic repeat distance, $d = 1/s$ describing the thickness of a

double lipid layer with hydration layer of water at pH 10 for **TT10** and **TO10** equal 51.3 and 52.6 Å, respectively. The values are very similar and are both relatively small. The theoretical length of the single 14C chain (both chains of **TT10**) is equal 13*1.26 Å (for trans -CH2) + 1.54 Å (for -CH3) = 18 Å, so the double layer of not tilted chains should be 36 Å thick. That leaves ~15-16 Å for the double size of the headgroup and water layer (usually 8-16 Å) [55] what seems a bit too little. It is possible that the chains are tilted what shortens the monolayer. This theory is supported by GIXD results for monolayers, which show very high tilt of ~39°. Monolayer experiments have also shown the presence of hydrogen bonds that may keep headgroups of neighboring double layers very close to each other and allowing only minimal content of water. The amount of water may also be low since experiment has been performed at pH 10 when all headgroups are expected to be free of charge, and as a consequence, less polar. One of scenarios is also the interdigitation of chains or headgroups and that seems the most reasonable, since crystals detected by GIXD were made of the interdigitated monolayers. According to DSC curves (not shown) the melting temperatures for **TT10** and **TO10** are 92.9 °C and 82.5 °C, respectively. At temperature of 25 °C at pH 10 **TT10** as well as **TO10** are in the gel phase (L_β). Lower melting temperature of **TO10** is an effect of the double bond that disturbs *all-trans* alignment of chains and so increases the layer fluidity. In agreement with DSC findings, SAXS of **TO10** shows change in the structure between 80 and 85 °C: apart from not molten gel lamellar phase (peak at $s = 0.019$ Å^{-1}), we can also observe several other peaks at small s values that result from the coexisting fluid phase (Fig. 45 and Fig. S3.1). The unambiguous identification of the fluid phase was not possible but most of reflexes could belong to a cubic phase of Ia3d symmetry type [60,63,136]. The reflexes are indexed in the figure. Apart from cubic and gel lamellar phase, there are also two peaks identifying a lamellar fluid phase of **TO10** (marked with arrows in the Fig. S3.1). Their positions match the ones of the fluid lamellar phase detected for **TO10** in water (read below). Coexistence of many different phases of the same compound at one temperature is most probably caused by the short time window between measurements at 80 and 85 °C that could affect detection of the "after transition phase" because it may have not be completed while the signal was recorded. The observed peaks may temporarily show up while on-going transition or belong to a metastable phase. Unfortunately, SAXS of **TT10** was not measured above 60 °C so no phase transition
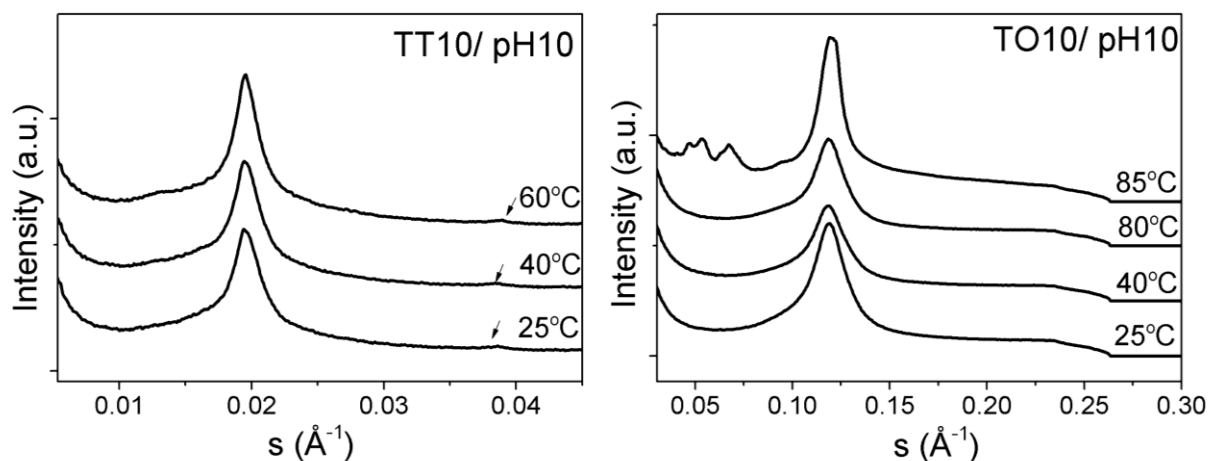
could be observed with this method.

Fig. 45 Temperature SAXS scans of TT10 and TO10 at pH 10.

In contrast to the monolayer experiments, the SAXS measurements **in water** show different structures than the ones at pH 10. Positions of peaks in case of **TT10** remain in 1: 2 ratio but move to smaller s values (s_1 = 0.0179 Å^{-1} => d = 55.8 Å). The thickness of the double layer gains 4.3 Å (Fig. 46). Apparently, **TT10** bilayer in water is more charged what attracts more water between double layers. More charge in the headgroup region leads also to the molecules repulsion what loosens the chain packing what also decreases the layers thickness. While heating d value increases insignificantly (up to d = 56.2 Å at 90 °C) and between 90 and 95 °C **TT10** undergoes the phase transition to a fluid phase. The structure remains lamellar (L$_\alpha$) but positions of peaks move drastically to lower s (higher d). Three orders of peaks can be seen in SAXS pattern (s_1 = 0.007 Å^{-1}, s_2 = 0.015 Å^{-1} and s_3 = 0.020 Å^{-1}) (Fig. 46 and Fig. S3.4). The quality of the scattering is not good but sufficient for the phase identification. The d of **TT10** lamellar fluid phase equals 143 Å what is 2.5 times more than for the gel phase. Since flexible molten chains are shorter than the elongated chain in gel phase, the large increase of the d value is usually assigned to the increase of water content between layers due to thermal effects. Typically the maximum water thickness for uncharged L$_\alpha$ phases is in the range of 10 - 30 Å but swelling to very large spacings has been already reported in the literature [137]. Moreover, the additional charge of headgroups can attract a lot of water. It is possible that the protonation degree of headgroups is strongly dependent on temperature, and the ratio of protonated to unprotonated species grows while heating. It has been also

reported before that lipids in the gel phase tent to be less charged than in the fluid phase [138]. Additionally, protonation of amine groups causes breaking of hydrogen bonds linking headgroups of the neighboring double layers. It cannot be forgotten that if the small d value of **TT10** in L$_\beta$ is caused by the chains interdigitation, then the melting of chains affects their strong hydrophobic interactions and interdigitation disappears, what also increases the double layer thickness.

In contrast to **TT10**, we can observe a complete change of the phase structure of **TO10** at low temperatures in water in comparison to L$_\beta$ at pH 10. In Fig. 46 (left panel, **TO10**/water) and Fig. S3.2 we can see three peaks. They can be assigned to the cubic phase of Ia3d symmetry and space group Q^{230}, where s_{221} = 0.016 : s_{220} = 0.019 : s_{321} = 0.024 is like $\sqrt{3} : \sqrt{4} : \sqrt{7}$ [60,63] and a parameter equals to 153 Å. If the identification is correct, then it would mean that **TO10** at low temperatures is in the fluid phase (gel phase does not form cubic structures). Unfortunately, no DSC or WAXS have been performed on that sample to confirm this finding. SAXS results cannot be compared to the monolayer experiments, where phase behavior of **TO10** is very similar on water and pH 10. The temperature scan of **TO10** suspension in water can be found in Fig. S3.2. As for **TT10**, also here the phase transition can be observed. The fluid structure observed for lower temperatures undergoes a change into a fluid lamellar phase between 85 and 90 ^{o}C. In Fig. 46 (right bottom panel) three very well defined reflexes in ratio of 1: 2: 3 (s_1 = 0.0064 Å^{-1}, s_2 = 0.0130 Å^{-1} and s_3 = 0.0196 Å^{-1}) can be seen. Their positions are shifted to a bit smaller s values in comparison to **TT10.** The calculated d equals 156 Å what is similar to the value calculated for **TT10** at the same conditions (d = 143 Å). The difference of 13 Å comes from the molecule structure. **TO10** has one chain which is 18C long with theoretical length of 23 Å, 5 Å longer than the 14C of **TT10.** The double layer of **TO10** could be then maximally 10 Å thicker than that of **TT10**. In this case though it is very unlikely since chains are fluid but still some space can be gained. Moreover, the other components of the TO complex may influence the structure and attract more water.
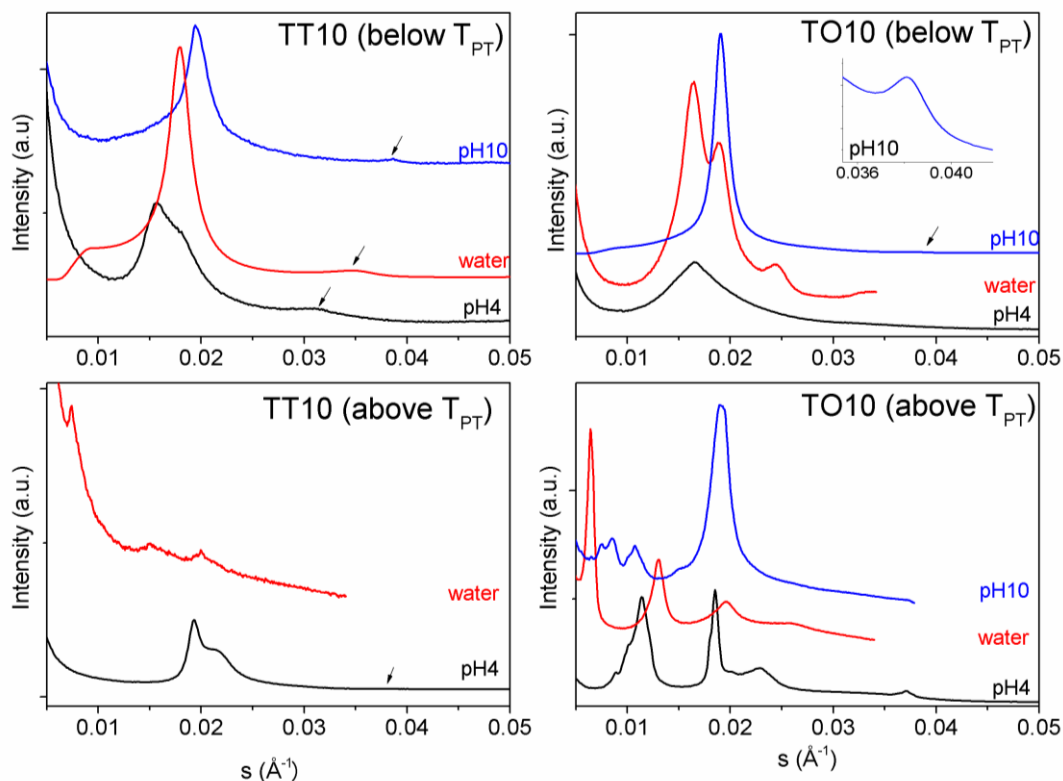
Fig. 46 SAXS patterns of TT10 and TO10 at 25 °C (below the phase transition) and above the phase transition (the exact temperature is indicated in the text) at different pHs. Arrows indicate reflections that are difficult to see due to the scale. Additionally the inset in the left top panel shows a magnified second order peak of TO10 at pH10. T_{PT} is the phase transition temperature.

At pH 4, the structure of **TT10** is not homogeneous. At 25 °C we can observe a phase separation: there is a lamellar phase characterized by two peaks in the ratio 1: 2, $s_1 = 0.0157$ Å^{-1} and $s_2 = 0.0311$ Å^{-1} and an additional shoulder to the first peak at $s = 0.0183$ Å^{-1} (Fig. 46, right top panel). The shoulder-peak is not followed by the second order reflection or the reflection is too weak to be observed. There is no physical explanation for a pure substance to form two different phases in the same conditions so it must be assumed here, that for some reason there are two different species in the suspension. One of theories is based on the assumption, that at pH 4 molecules are unequally protonated. Double layers of more protonated lipids give rise to the peak at lower s (higher d) due to additional water attracted between layers. The less protonated lipids are in minority (the peak is less intense) and give a reflex at the position close to the one in water ($s_{1H2O}= 0.0179$ Å^{-1}). The assumption is supported by the results of monolayer experiments were TT10 at pH 4 shows two phase transitions. Other possibility that could explain the presence of the peak at $s = 0.0183$ Å^{-1} is unequal

hydration, but this one is unlikely since the suspension has been prepared in an excess of buffer. The *d* calculated for the first reflex at 25 °C equals 63.7 Å and remains constant up to 50 °C to go through the intermediate value of 57.8 Å at 60 °C and become 52.2 Å at 70 °C and higher. Above the transition temperature the L_α phase is formed. The phase transition temperature at around 60 °C is in a good agreement with the melting temperature of 58 °C at pH 5 determined by DSC (SAXS was measured at pH 4). The second phase undergoes the phase transition together with the main lamellar structure and the Bragg peak changes position from 0.0183 Å^{-1} at 25 °C to 0.0213 Å^{-1} at 90 °C (Fig. 47, right panel). Unlike in water, the *d* value decreases after the phase transition. The 11.5 Å thickness loss can be assigned to the chain melting. The interesting fact is that at pH 4 the effect of transition is much less drastic than for water, where *d* suddenly grows 2.5 times. Maybe breaking intermolecular hydrogen bonding while the phase transition in water, which are absent in case of pH 4, and sudden separation of interdigitated molecules give more perturbations that allow more dynamic water hydration. Moreover, the pH 4 buffer, citric acid/ sodium citrate, can be responsible for complexation of headgroups in the network of hydrogen bonding. This kind of buffer – headgroup interaction may not let bilayers separate during the phase transition.
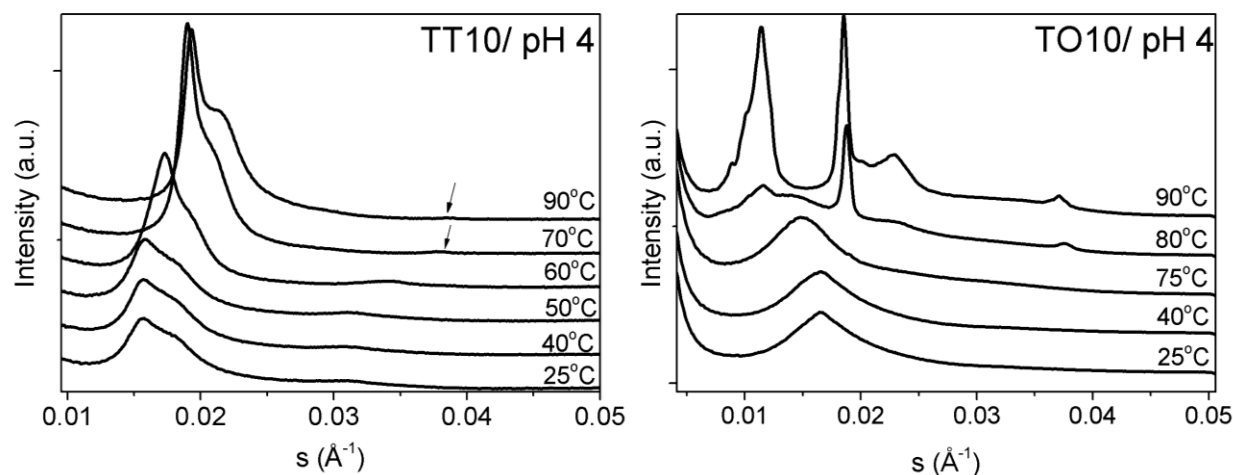

Fig. 47 Temperature SAXS scans of TT10 and TO10 at pH 4.

TO10 at low temperatures at pH 4 forms weakly correlated layer structures which give characteristic diffused Bragg peak of high FWHM (Fig. 46, top left panel). No second order peak can be observed. At pH 4 headgroups are assumed to be fully protonated what repulses them from each other and fluidizes the membrane. If we assume that the

observed structure is lamellar, than at 25 °C d = 60.6 Å, what is a bit smaller than the adequate d of **TT10**. DSC of **TO10** at pH 5 shows no phase transition (not shown). These facts allow conducting, that **TO10** is fluid. Nevertheless, SAXS temperature scan clearly show the phase transition between 75 and 80 °C T (Fig. 47, left panel). Since the thermal effect of the transformation is too small to be detected by DSC, it must be a fluid to fluid transition. At 90 °C there are many reflexes. Like for pattern at pH 10, also here we can assign them to coexisting phases. The magnified SAXS pattern of **TO10** at pH 4 at 90 °C is shown in Fig. S3.3. The peaks identified with arrows belong to **TO10** lamellar phase *(s_1 =* 0.0185 Å^{-1}, s_2 = 0.0371 Å^{-1}). Since no phase transition was observed by DSC, the phase must be fluid. It is very different then the lamellar fluid phase observed in water. It may be an effect of citric acid molecules of the buffer that hold lipid layers complexed and do not allow their separation. The peaks marked with the rectangle seem to belong to the fluid phase of **TT10** that is formed at pH 4 (see Fig. 47, right panel). Here it must be remarked, that **TO10** is a multicomponent compound and by amount, **TT10** is the second compound in the system. Apart from these phases, many peaks at small s values can be clearly seen (marked by ratio indexes in Fig. S3.3). As for the measurement at pH 10, also here they can be assigned to the Ia3d cubic phase. The first order reflex ($\sqrt{3}$) cannot be seen due to the q range used for the measurement.

3.4.2 Mixtures of TT10 and TO10 with DOPE

Both lipids, TT10 and TO10, have been used as transfection agents in complexes with a helper lipid, DOPE. The structures of these mixtures have been studied by SAXS. DOPE is a lipid that is commonly used for gene transfection complexes due to its ability to form inverted hexagonal structures that are believed to improve the transfection efficiency. The chemical structure of DOPE is presented in Fig. 48 and its structure at 20 °C in water is shown in grey in Fig. 49.
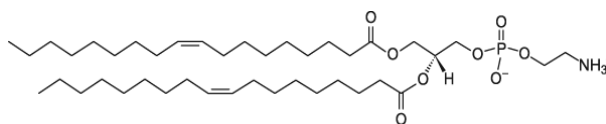

Fig. 48 The chemical structure of DOPE (1,2-dioleoyl-*sn*-glycero-3-phosphoethanolamine).

For both lipids three different molar ratios have been investigated, lipid to DOPE 1:4, 1:1 and 2:1. As seen in Fig. 49B, mixtures of **TO10**, where the amount of the lipid is higher or

equal to the amount of DOPE, form weakly organized structures that could be uncorrelated bilayers. The change of the structure in comparison to a pure DOPE and pure **TO10** indicates, that both lipids mix well. **TT10** mixed with DOPE in ratios 1:1 and 2:1 gives a well defined Bragg peak. Due to the short range of measured *s* the second order peak cannot be observed. If we assume the multilamellar structure, the peak for both ratios corresponds to a *d* value of 49 Å, what is 7 Å smaller than for a pure **TT10** lipid in water at the same temperature. The lack of the hexagonal phase observed for pure DOPE and the change of the *d* value of **TT10** proves, that DOPE is integrated in the lipid bilayers. At 20 ºC, the chains of pure DOPE are fluid and a hexagonal superstructure is formed. In contrast, pure **TT10** is in the lamellar gel phase with ordered alkyl chains. Previously it was assumed that pure **TT10** forms thin bilayers of interdigitated chains. After addition of DOPE the *d* value is even smaller, so it must be assumed, that **TT10** in the mixture remains interdigitated, and the layer thickness shrinks due to chain fluidization. DOPE is a well known fluidizing agent. In this case the fluidization is not caused by the temperature so the lipid headgroups remain linked via hydrogen bonds and the thickness of the layer does not change drastically. The FWHM of the Bragg peak of **TT10**/ DOPE (2:1) complex is smaller than for the ratio of 1:1 what indicates that the bilayers of the first complex are better correlated than for the mixture with the higher amount of DOPE. High percentage of DOPE may not only fluidize but also destabilize the **TT10** structure.
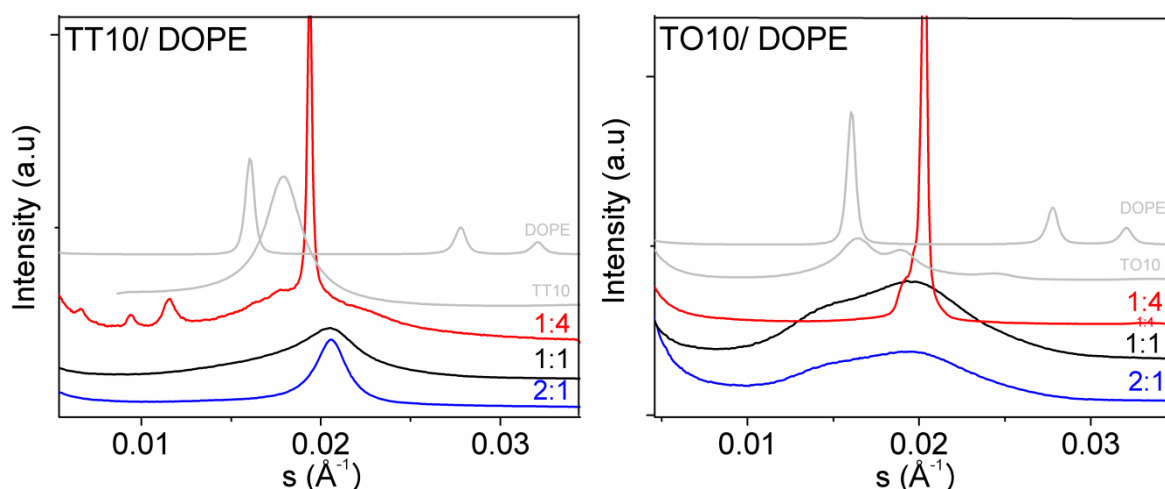

Fig. 49 SAXS of mixtures of TT10 and TO10 with DOPE at 20 ºC in water in various molar ratios: lipid/DOPE (1:4) (red),lipid/DOPE (1:1) (black) and lipid/DOPE (2:1) (blue). The pure DOPE and pure TT10 and TO10 in water at 20 ºC have been shown in grey for comparison.

For both lipids a completely different structure is observed when the amount of DOPE increases to the ratio of 1:4 (lipid:DOPE). In Fig. 49A we can clearly see that a new structure has been formed. What is interesting, despite a big excess of DOPE, the H_{II} phase has not been released from the complex. In exchange of it a few peaks at low s values appeared. The peaks can be assigned to a body centered cubic phase of Im3m symmetry. The detailed indexing has been presented in the supporting information in Fig. S3. 5. The formation of Im3m cubic phase has been already observed for other PE lipids (phosphatidylethanolamines). In the literature, the presence of sodium salts and polycarbohydrates is believed to induce the H_{II} to Im3m phase transition [139]. Other researches claim, that DOPE tends to form stable Pn3m cubic phase upon many heating and cooling scans [140]. In the case of this work, no heating, cooling or salts have been used. Addition of **TT10** must have induces the transition. The phase structure of **TO10**/DOPE (1:4) is difficult to identify due to the small amount of peaks that additionally are not well resolved.

3.4.3 Mixtures of TT10/ DOPE (1:4) and TO10/ DOPE (1:4) with DNA

Both lipids have been also examined as mixtures with a helper lipid, DOPE, and model ct-DNA. The physical-chemical investigation was carried out for the complexes that have shown the best transfection results. Here, it is worth to mention, that neither of the tested combinations/ratios of the lipid, DOPE and DNA have performed well in transfection. All analyzed systems were very ordinary and none of them showed promising results. Nevertheless, the SAXS analysis has been performed. The SAXS curves of **TT10**/DOPE (1:4) and **TO10**/DOPE (1:4) complexes with ctDNA in N/P ratio 2:1 are shown in Fig. 50.
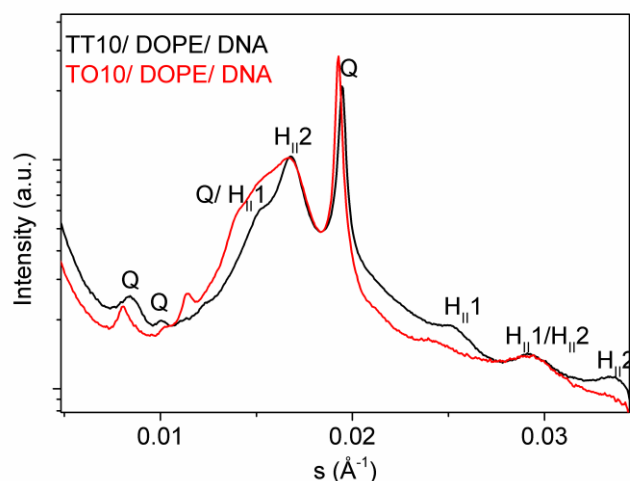
Fig. 50 SAXS pattern of water suspensions of TT10/DOPE (1:4) (black)and TO10/DOPE (1:4) (red) mixed with ct DNA in N to P ratio of 2:1 at 20 °C.

The SAXS pattern after DNA addition changes drastically for both mixtures. **TT10**/ DOPE (1:4) shows Im3m cubic phase. Addition of DNA releases some of DOPE and hexagonal phases can be observed. Pure DOPE forms the inverted hexagonal phase, so here it can be assumed the same. However, in the system, not only one, but two coexisting hexagonal phases are present. Additionally, the cubic phase of Im3m symmetry is still there. The DNA triggers the phase separation. But none of the compounds is fully separated from the others and mixtures of various ratios are formed. The phases are indexed in Fig. 50. The two hexagonal phases are most probably formed by mixtures with a big excess of DOPE and different amounts of integrated **TT10** and DNA. Higher quantity of the cationic lipid should attract more DNA and d of the phase should increase as more of DNA is trapped inside the inverted micelles-like rods. In this case it is true for the phase marked as $H_{II}1$ in the figure. d of DOPE and $H_{II}1$ phase equal to 62.5 and 66.6 Å, respectively. The Bragg peaks corresponding to the other inverted hexagonal phase, $H_{II}2$, are shifted to higher s (d = 59.5 Å) in comparison to pure DOPE, so the phase is assumed not to consist of DNA. Nevertheless, some **TT10** must be integrated into the phase, and moreover, **TT10** must be responsible for the decrease in the rod diameter a (the macro structural unit of hexagonal phase). The parameter a can be calculated using $d = \sqrt{3}/2a$. For the 20 wt% dispersion of pure DOPE in water at 20 °C a equals to 72 Å. For the two hexagonal phases identified here, $H_{II}1$ and $H_{II}2$, the a parameter equals to 76 and 68 Å, respectively. It is difficult to say which exactly feature of **TT10** tightens the

DOPE structure in $H_{II}2$. The cubic phase can be identified by peaks at smaller s values (indexed with Q in Fig. 50). We can see reflexes starting from the second peak at $s = 0.0084$ Å^{-1}. The characteristic a parameter (for Im3m $s = \sqrt{2}/a$) of the TT10/ DOPE (1:4) was equal to 211 Å. After DNA addition a increased to 239 Å. The 28 Å of difference comes from DNA trapped in the structure – the double helix diameter is 20 Å.

Very similar structure can be observed for the **TO10**/DOPE (1:4) complex with ct-DNA in the N/P ratio of 2:1 (see Fig. 50). As for **TT10**, also here we can observe a formation of two coexisting hexagonal phases. Also the cubic phase, that has not been observed for the **TO10**/DOPE (1:4) complex, can be identified. The structure is almost identical with the structure observed for the analogous **TT10** mixture, what makes it clear that Bragg peaks of **TO10**/DOPE (1:4) that could not be assigned to any structure in the previous chapter must belong to the Im3m cubic phase. The phase though is not pronounced as well as in the case of **TT10**. It may be due to differences in the lipids chemical structure. The double bond present in **TO10** molecule generally disturbs the alignment of lipid chains and even with a big excess of DOPE precludes ordering. That could be a proof that in this case, the headgroup of the cationic lipid plays a bigger role in the cubic phase formation than its hydrophobic moiety.

The fact, that the structures of the analogous complexes of both lipids with DOPE and ct-DNA are almost identical, is probably a reason for the very similar transfection results. As mentioned before, both lipids are very ordinary lipofectants.

4. CONCLUSIONS

Two lipids with the same headgroup but different chains, **TT10** (14:0, 14:0) and **TO10** (14:0, 18:1) have been examined in monolayers and bulk systems. Even though they have different physical-chemical properties due to the different chain structure and the resulting from it fluidity, their transfection performance does not vary considerably. **TT10** forms a stiff condensed monolayer of molecules interconnected with a hydrogen bond network. The lipid aggregates in water develop multilamellar gel structures with relatively small d values (51 – 64 Å in dependence of pH) and undergo the phase transition at high temperatures to the fluid lamellar structures (L_α) with different d values. In contrast, due to the presence of a double bond in one of the chains, the

monolayers of **TO10** are rather fluid. Hydrated lipid aggregates are lamellar at low temperatures (apart from dispersion in water, where an undefined structure has been found) and turn into cubic ones at higher temperatures. Nevertheless, even though **TO10** has a tendency to non-lamellar structure formation and consists of an oleyl chain in the structure (parameters that are known to improve transfection efficiency), it has been identified as a very ordinary lipofection compound. Moreover, the investigation of the best transfection performance complexes of both lipids, **TT10**/DOPE (1:4) and **TO10**/DOPE (1:4) mixed with ct-DNA in the ratio of N/P 2:1 shows, that these systems form a mixture of coexisting cubic and inverted hexagonal phases. Though, the transfection results are very poor for both lipids. As proven by this research, the tendency to non-lamellar phase formation and the presence of the oleyl chain are not sufficient to create a well performing transfection system. Transfection is a complicated process and a lot of factors must be taken into account when designing a potential lipofectant.

Supporting Information can be found in the appendix. Details of SAXS experiments are presented.

GENERAL CONCLUSIONS

There are many factors that influence the transfection efficiency of a given cationic lipid system (lipoplex structure, charge, type of the cell, etc.). Some of them are believed to be more important than others. There is a common conviction, that complexes that form non-lamellar phases are better than those that order in bilayers, since they fuse better with a cellular membrane and then destabilize the endosome and enable the nucleic acid escape. That is why DOPE, forming the inverted hexagonal phase, is the most commonly used helper lipid. This research shows though, that this is not necessarily the complete truth. In chapter one, that describes the comparison of two samples of the same cationic lipid that differ only in purity. It is clearly shown that the analytically pure sample, that forms even cubic phases, does almost not transfect, in contrast to the second sample of technical grade, in which the cubic phase formation is suppressed by the other components (mainly with saturated chains) of the system. The same can be observed for the two lipids analyzed in chapter 3. When complexed with DOPE and DNA, both of them form mixtures of coexisting cubic and hexagonal phases, but also both transfect very badly in comparison to the commercially available transfection compounds.

Another feature that is believed to improve the transfection efficiency is the oleyl chain presence in the cationic lipid molecule. Both lipids compared in chapter 1 consist of the oleyl chain, but only one performs well as lipofectant. In chapter 3, there is no improvement in the transfection efficiency for the molecule with one oleyl chain in comparison to its analogue that has two saturated chains. For a change, chapter 2 presents three molecules with the same hydrocarbon moiety (without oleyl chain) and differing in the headgroup structure, and they all show better transfection efficiencies than the systems available on the market.

The transfection – structure relationship studies show, that it is very difficult to define the main properties of the lipid that could assure good transfection efficiency. The process is very complex. Apart from a careful systems design based on the state of art, the extensive *in vitro* and *in vivo* experiments are always needed to check the lipofectant efficacy.

Apart from the lipoplex structure correlation with the transfection efficiency, the research described in this thesis was focused also on the physical-chemical properties of

the new lipids. The described dependencies are expected and concurring with the common knowledge in the field. For lipids with the same headgroup structure, the fluidity increases with the number of double bonds in the chain region: TO10 (18:1, 14:0) was more fluid than TT10 with two saturated chains (14:0, 14:0) (chapter 2). The fluidity also increased with the size and charge of the headgroup of the lipids with the same chain pattern (chapter 2). For monolayers of cationic lipids measured at different pH, the expansion was observed on the acidic solutions, due to the electrostatic repulsion of protonated headgroups, while at higher pH values the monolayers were more condensed. GIXD showed, that the formation of hydrogen bonds between the headgroups can tighten the lipid chains packing (chapter 2), and that for multicomponent systems, the structures are a resultant of the ordering of all system components (chapter 1). The analysis of the lipids in bulk proves that the protonation of the lipids in layers lowers the melting temperatures due to the electrostatic repulsion between molecules and the consequent layer expansion. The protonation influences also the structures formed by lipids in bulk. When at pH 10 the analyzed systems tend to order in multilamellar stacks, at pH 4 they show a great variety of mainly cubic structures (chapter 1 and 3).

EXPERIMENTAL DETAILS

1. MONOLAYER EXPERIMENTS

The cationic lipid in chloroform (0.5 mM) was spread onto the buffer subphase with a micro-syringe and left for 10 minutes before compression for complete solvent evaporation. For DNA experiments, 0.1 mM ctDNA in the relevant buffer was used as subphase. The lipid monolayer was spread onto the DNA containing subphase and left in the uncompressed state for one hour to equilibrate DNA adsorption. Two different buffers were used for the experiments: acidic citric buffer of pH 4 and basic carbonate buffer of pH 10.

1.1 FILM BALANCE MEASUREMENTS

The pressure/area (π/A) isotherms were measured on a computer-interfaced Langmuir trough (R&K, Potsdam, Germany) equipped with a Wilhelmy type surface pressure microbalance. The films were compressed at a rate of 2.1 Å^2/(molecule·min). All measurements were performed at constant subphase temperature (indicated) with an accuracy of 0.1 °C.[31]

1.2 INFRARED REFLECTION ABSORPTION SPECTROSCOPY (IRRAS)

Infrared reflection-absorption spectra (IRRA spectra) were recorded on a Vertex 70 FT-IR spectrometer (Bruker, Ettlingen, Germany) equipped with Mercury Cadmium Telluride (MCT) detector cooled with liquid nitrogen. The IR beam was polarized by a KRS-5 wire grid polarizer in the plane of incidence (p) and perpendicular to this plane (s). Spectra were recorded with a resolution of 8 cm^{-1} and a scanning velocity of 20 kHz. For each single beam spectrum 200 scans of s-polarized light and 400 scans for p-polarized light were collected. The angle of incidence normal to the surface was set to 40°. The Langmuir trough used for the IRRAS measurements has two movable barriers allowing symmetric compression of the monolayer [141-143].

1.3 GRAZING INCIDENCE X-RAY DIFFRACTION (GIXD)

All measurements were performed using the liquid surface diffractometer at the undulator beamline BW1 (HASYLAB, DESY, Hamburg, Germany). The Langmuir trough

was located in a thermostated, hermetically closed container flushed with He. The synchrotron beam was monochromated by a beryllium (002) crystal to a wavelength of 1.304 Å. The incidence angle at the liquid surface was 0.11°, which is ~85% of the critical angle for total external reflection from water at this X-ray energy. A MYTHEN detector system (PSI, Villigen, Switzerland) was used to record the intensity of the diffracted beam as a function of the vertical scattering vector component ($Q_z \approx$ $(2\pi/\lambda)sin\alpha_f$) and the horizontal scattering vector component ($Q_{xy} \approx (4\pi/\lambda)sin(2\theta/2)$), where α_f is the vertical and 2θ the horizontal scattering angle. The horizontal resolution (0.008 Å^{-1}) was determined by a Soller collimator (JJ X-RAY, Denmark) located in front of the detector. The intensities were corrected for polarization, effective area, and Lorentz factor. Model peaks, taken as Lorentzian in the in-plane direction (Bragg peak, Q_{xy}) and as Gaussian in the out-of-plane direction (Bragg rod, Q_z), were fitted to the corrected intensities. The Q_{xy} and Q_z values were used to calculate lattice unit cell parameters, unit cell distortion (*d*), chain tilt angle (*t*) and chain cross-sectional area (A_0). The finite size L_{xy} of crystalline domains in a monolayer can be determined with the Scherrer formula $L_{xy} = 0.88 \cdot (2\pi/\Delta Q_{xy})$ where ΔQ_{xy} is the full-width at half-maximum (FWHM) of the Lorenzian peak corrected with the detector resolution. The thickness of the scattering unit (length of a chain contributing to the signal) can be calculated using $L_z = 0.88 \cdot (2\pi/\Delta Q_z)$, with ΔQ_z being the FWHM of the Gaussian peak [77,78,80].

1.4   BREWSTER ANGLE MICROSCOPY (BAM)

For the experiments, Brewster Angle Microscope BAM2plus from NanoFilm Technologie, Goetingen, Germany was used. The microscope was connected with a film balance (NIMA Technology) that was set on antivibrational table. The imagining systems consisted of a frequency-doubled Nd: YAG laser (532nm; 50mW), a polarizer, an analyzer and a CCD camera. The angle of incidence was set to 53.1°. The image was taken from the monolayer spread on the air/water interface. The LC phase was observed as bright spots on the dark background of water or LE phase. The image size is 355 x 470 μm and the lateral resolution is ~2 μm.

2. BULK EXPERIMENTS

2.1 SYNCHROTRON SMALL- AND WIDE-ANGLE X-RAY SCATTERING EXPERIMENTS (SAXS/WAXS)

SAXS enables the determination of long-range organization of fully hydrated lipids in bulk. WAXS gives information about the layer in-plane structures reflecting the lipid packing. SAXS/WAXS experiments were performed at the Soft Condensed Matter beamline A2 (HASYLAB, DESY, Hamburg, Germany). Aqueous dispersions of the lipids or their mixtures (with cholesterol and model DNA) were prepared (20 weight-% lipid), heated up to 80 °C and placed into glass capillaries. SAXS and WAXS patterns of samples were measured simultaneously by a MAR CCD detector (Evanston, Illinois, USA) and a linear detector with delayline, respectively. The incoming beam had a wavelength of 0.15 nm. Exposure time was 30 s. All data were recorded in the temperature range between 20 °C and 70 °C in 5 °C steps. The Bragg peak maxima were determined by Lorenzian fit. The obtained s-values were translated into the spacing of lattice planes, d, using $s = 1/d$ [144-146].

2.2 DIFFERENTIAL SCANNING CALORIMETRY (DSC)

The corresponding lipid was dispersed to a concentration of 1 mg/mL using different media (5 mM carbonate buffer (pH 10, $Na_2CO_3/NaHCO_3$), 5 mM citric buffer (pH 4, $C_6H_8O_7/Na_3C_6H_5O_7$), water). Mixtures with cholesterol were prepared in a final concentration of 3 mM. Before film rehydration, the lipids were dissolved in $CHCl_3$/methanol (7:3 v:v), the organic solvent was evaporated under a nitrogen stream, and the film was dried 12 h in vacuo. The hydrated samples were heated two times to 80 °C and vortexed followed by 20 min sonication at 60 °C. Finally, the samples were degassed for 15 min.

The DSC measurements were performed on a MicroCal VP-DSC (MicroCal Inc. Northampton, MA, USA). The heating rate was 60 °C/h in the temperature range between 2 °C and 95 °C. Each heating and cooling scan was repeated confirming reproducibility, the first scan was abolished. The reference cell was filled with the pure solvent. The buffer-buffer baseline was subtracted from the thermograms of the samples, and the DSC scans were evaluated using MicroCal Origin 8.0 software. The DSC

measurments were carried out by Christian Woelk at the Pharmacy Department of Martin Luther Iniversity in Halle.

3. BIOLOGICAL EXPERIMENTS

The biological experiments were carried out by Patrick Kreideweiß from Martin Luther University in Halle.

REFERENCES

(1)   Friedmann, T.; Roblin, R. *Science* **1972**, *175*, 949.

(2)   Fibison, W. J. *Nursing Clinics of North America* **2000**, *35*, 757.

(3)   Fischer, A.; Hacein-Bey-Abina, S.; Cavazzana-Calvo, M. *Nature Immunology* **2010**, *11*, 457.

(4)   Cartier, N.; Aubourg, P. *Brain Pathology* **2010**, *20*, 857.

(5)   LeWitt, P. A.; Rezai, A. R.; Leehey, M. A.; Ojemann, S. G.; Flaherty, A. W.; Eskandar, E. N.; Kostyk, S. K.; Thomas, K.; Sarkar, A.; Siddiqui, M. S.; Tatter, S. B.; Schwalb, J. M.; Poston, K. L.; Henderson, J. M.; Kurlan, R. M.; Richard, I. H.; Van Meter, L.; Sapan, C. V.; During, M. J.; Kaplitt, M. G.; Feigin, A. *The Lancet Neurology* **2011**, *10*, 309.

(6)   Ylä-Herttuala, S. *Molecular Therapy* **2012**, *20*, 1831.

(7)   Kamimura, K.; Suda, T.; Zhang, G.; Liu, D. *Pharmaceutical Medicine* **2011**, *25*, 293.

(8)   Kim, T. K.; Eberwine, J. H. *Analytical and Bioanalytical Chemistry* **2010**, *397*, 3173.

(9)   Walther, W.; Stein, U. *Drugs* **2000**, *60*, 249.

(10)   Zhang, X.; Godbey, W. T. *Advanced Drug Delivery Reviews* **2006**, *58*, 515.

(11)   Robbins, P. D.; Ghivizzani, S. C. *Pharmacology & Therapeutics* **1998**, *80*, 35.

(12)   Yin, H.; Kanasty, R. L.; Eltoukhy, A. A.; Vegas, A. J.; Dorkin, J. R.; Anderson, D. G. *Nature Reviews Genetics* **2014**, *15*, 541.

(13)   Wang, W.; Li, W.; Ma, N.; Steinhoff, G. *Current Pharmaceutical Biotechnology* **2013**, *14*, 46.

(14)   Guo, X.; Huang, L. *Accounts of Chemical Research* **2012**, *45*, 971.

(15)   Felgner, P. L.; Gadek, T. R.; Holm, M.; Roman, R.; Chan, H. W.; Wenz, M.; Northrop, J. P.; Ringold, G. M.; Danielsen, M. *Proceedings of the National Academy of Sciences of the United States of America* **1987**, *84*, 7413.

(16)   Caracciolo, G.; Amenitsch, H. *European Biophysics Journal* **2012**, *41*, 815.

(17)   Audouy, S.; Hoekstra, D. *Molecular Membrane Biology* **2001**, *18*, 129.

(18)   Samad, A.; Sultana, Y.; Aqil, M. *Current Drug Delivery* **2007**, *4*, 297.

(19)   Rehman, Z. u.; Zuhorn, I. S.; Hoekstra, D. *Journal of Controlled Release* **2013**, *166*, 46.

(20)   Wrobel, I.; Collins, D. *Biochimica et Biophysica Acta - Biomembranes* **1995**, *1235*, 296.

(21)   Xu, Y.; Szoka Jr, F. C. *Biochemistry* **1996**, *35*, 5616.

(22)   Ma, B.; Zhang, S.; Jiang, H.; Zhao, B.; Lv, H. *Journal of Controlled Release* **2007**, *123*, 184.

(23)   Dittrich, M.; Heinze, M.; Wölk, C.; Funari, S. S.; Dobner, B.; Möhwald, H.; Brezesinski, G. *ChemPhysChem* **2011**, *12*, 2328.

(24)   Dittrich, M.; Böttcher, M.; Oliveira, J. S. L.; Dobner, B.; Möhwald, H.; Brezesinski, G. *Soft Matter* **2011**, *7*, 10162.

(25)   Ulrich, A. S. *Bioscience Reports* **2002**, *22*, 129.

(26)   Noone, P. G.; Hohneker, K. W.; Zhou, Z.; Johnson, L. G.; Foy, C.; Gipson, C.; Jones, K.; Noah, T. L.; Leigh, M. W.; Schwartzbach, C.; Efthimiou, J.; Pearlman, R.; Boucher, R. C.; Knowles, M. R. *Molecular Therapy* **2000**, *1*, 105.

(27)   Stopeck, A. T.; Jones, A.; Hersh, E. M.; Thompson, J. A.; Finucane, D. M.; Gutheil, J.

(28)   Van Tendeloo, V. F. I.; Ponsaerts, P.; Berneman, Z. N. *Current Opinion in Molecular Therapeutics* **2007**, *9*, 423.

(29)   Zhang, S.; Zhi, D.; Huang, L. *Journal of Drug Targeting* **2012**, *20*, 724.

(30)   Mellott, A. J.; Forrest, M. L.; Detamore, M. S. *Annals of Biomedical Engineering* **2013**, *41*, 446.

(31)   Al-Lawatia, Y. M. M.; Mullaicharam, A. R. *Research Journal of Pharmaceutical, Biological and Chemical Sciences* **2013**, *4*, 813.

(32)   Herman, P. *Current Gene Therapy* **2013**, *13*, 383.

(33)   Thomas, C. E.; Ehrhardt, A.; Kay, M. A. *Nature Reviews Genetics* **2003**, *4*, 346.

(34)   Kay, M. A.; Glorioso, J. C.; Naldini, L. *Nature Medicine* **2001**, *7*, 33.

(35)   Pathak, A.; Patnaik, S.; Gupta, K. C. *Biotechnology Journal* **2009**, *4*, 1559.

(36)   Tang, G. P.; Lu, X. *Zhejiang da xue xue bao. Yi xue ban = Journal of Zhejiang University. Medical sciences* **2009**, *38*, 1.

(37)   Mintzer, M. A.; Simanek, E. E. *Chemical Reviews* **2009**, *109*, 259.

(38)   Geisbert, T. W.; Lee, A. C.; Robbins, M.; Geisbert, J. B.; Honko, A. N.; Sood, V.; Johnson, J. C.; de Jong, S.; Tavakoli, I.; Judge, A.; Hensley, L. E.; MacLachlan, I. *The Lancet* **2010**, *375*, 1896.

(39)   Hillaireau, H.; Couvreur, P. *Cellular and Molecular Life Sciences* **2009**, *66*, 2873.

(40)   Kichler, A.; Leborgne, C.; Coeytaux, E.; Danos, O. *Journal of Gene Medicine* **2001**, *3*, 135.

(41)   Tseng, W. C.; Haselton, F. R.; Giorgio, T. D. *Biochimica et Biophysica Acta - Gene Structure and Expression* **1999**, *1445*, 53.

(42)   Parker, A. L.; Newman, C.; Briggs, S.; Seymour, L.; Sheridan, P. J. *Expert Reviews in Molecular Medicine* **2003**, *5*.

(43)   Kalepu, S.; Sunilkumar, K. T.; Betha, S.; Mohanvarma, M. *International Journal of Drug Development and Research* **2013**, *5*, 62.

(44)   Maheswaran, A.; Brindha, P.; Mullaicharam, A. R.; Masilamani, K. *International Journal of Pharmaceutical Sciences Review and Research* **2013**, *23*, 295.

(45)   Allen, T. M.; Cullis, P. R. *Advanced Drug Delivery Reviews* **2013**, *65*, 36.

(46)   Zhi, D.; Zhang, S.; Wang, B.; Zhao, Y.; Yang, B.; Yu, S. *Bioconjugate Chemistry* **2010**, *21*, 563.

(47)   Balasubramaniam, R. P.; Bennett, M. J.; Aberle, A. M.; Malone, J. G.; Nantz, M. H.; Malone, R. W. *Gene Therapy* **1996**, *3*, 163.

(48)   Ilies, M. A.; Seitz, W. A.; Balaban, A. T. *Current Pharmaceutical Design* **2002**, *8*, 2441.

(49)   Karmali, P. P.; Chaudhuri, A. *Medicinal Research Reviews* **2007**, *27*, 696.

(50)   Niculescu-Duvaz, D.; Heyes, J.; Springer, C. J. *Current medicinal chemistry* **2003**, *10*, 1233.

(51)   Frolov, V. A.; Shnyrova, A. V.; Zimmerberg, J. *Cold Spring Harbor Perspectives in Biology* **2011**, *3*.

(52)   Mouritsen, O. G. *European Journal of Lipid Science and Technology* **2011**, *113*, 1174.

(53)   Holmberg, K. *Surfactants and Polymers in Aqueous Solutions*; John Willey & Sons, Ltd., 2002.

(54)   Tresset, G. *PMC Biophys* **2009**, *2*, 1.

(55)   Seddon, J. M.; Templer, R. H. In *Handbook of Biological Physics* 1995; Vol. 1, p 97.

(56)   Cevc, G. *Chemistry and Physics of Lipids* **1991**, *57*, 293.

(57)   Seddon, J. M. *Biochimica et Biophysica Acta - Biomembranes* **1990**, *1031*, 1.

(58)   Rappolt, M. In *Advances in Planar Lipid Bilayers and Liposomes* 2006; Vol. 5, p 253.

(59)   In *Handbook of Lipid Bilayers, Second Edition*; CRC Press: 2013.

(60)   Lindblom, G.; Rilfors, L. *Biochimica et Biophysica Acta (BBA) - Reviews on Biomembranes* **1989**, *988*, 221.

(61)   Norman, H. F. M. L., K. *International tables for X-ray crystallography: Symmetry Groups*; The Kynoch Press, 1969; Vol. I.

(62)   Cherezov, V.; Clogston, J.; Misquitta, Y.; Abdel-Gawad, W.; Caffrey, M. *Biophysical Journal* **2002**, *83*, 3393.

(63)   Luzzati, V.; Spegt, P. A. *Nature* **1967**, *215*, 701.

(64)   Eriksson, P. O.; Lindblom, G.; Arvidson, G. *Journal of Physical Chemistry* **1987**, *91*, 846.

(65)   Safinya, C. R. *Current Opinion in Structural Biology* **2001**, *11*, 440.

(66)   Ewert, K.; Slack, N. L.; Ahmad, A.; Evans, H. M.; Lin, A. J.; Samuel, C. E.; Safinya, C. R. *Current medicinal chemistry* **2004**, *11*, 133.

(67)   Zuhorn, I. S.; Bakowsky, U.; Polushkin, E.; Visser, W. H.; Stuart, M. C. A.; Engberts, J. B. F. N.; Hoekstra, D. *Molecular Therapy* **2005**, *11*, 801.

(68)   Koynova, R.; Wang, L.; MacDonald, R. C. *Molecular Pharmaceutics* **2008**, *5*, 739.

(69)   Lin, A. J.; Slack, N. L.; Ahmad, A.; George, C. X.; Samuel, C. E.; Safinya, C. R. *Biophysical Journal* **2003**, *84*, 3307.

(70)   Hui, S. W.; Langner, M.; Zhao, Y. L.; Ross, P.; Hurley, E.; Chan, K. *Biophysical Journal* **1996**, *71*, 590.

(71)   Sakurai, F.; Nishioka, T.; Saito, H.; Baba, T.; Okuda, A.; Matsumoto, O.; Taga, T.; Yamashita, F.; Takakura, Y.; Hashida, M. *Gene Therapy* **2001**, *8*, 677.

(72)   Pozzi, D.; Marchini, C.; Cardarelli, F.; Amenitsch, H.; Garulli, C.; Bifone, A.; Caracciolo, G. *Biochimica et Biophysica Acta - Biomembranes* **2012**, *1818*, 2335.

(73)   Wasungu, L.; Hoekstra, D. *Journal of Controlled Release* **2006**, *116*, 255.

(74)   Marshall, J.; Nietupski, J. B.; Lee, E. R.; Siegel, C. S.; Rafter, P. W.; Rudginsky, S. A.; Chang, C. D.; Eastman, S. J.; Harris, D. J.; Scheule, R. K.; Cheng, S. H. *Journal of Drug Targeting* **2000**, *7*, 453.

(75)   Blaudez, D.; Turlet, J.-M.; Dufourcq, J.; Bard, D.; Buffeteau, T.; Desbat, B. *Journal of the Chemical Society, Faraday Transactions* **1996**, *92*, 525.

(76)   Mendelsohn, R.; Brauner, J. W.; Gericke, A. *Annual Review of Physical Chemistry* **1995**, *46*, 305.

(77)   Als-Nielsen, J.; Jacquemain, D.; Kjaer, K.; Leveiller, F.; Lahav, M.; Leiserowitz, L. *Physics Reports* **1994**, *246*, 251.

(78)   Kjaer, K. *Physica B: Condensed Matter* **1994**, *198*, 100.

(79)   Stefaniu, C.; Brezesinski, G. *Current Opinion in Colloid & Interface Science* **2014**, *19*, 216.

(80)   Jensen, T. R.; Kjaer, K. In *Studies in Interface Science* 2001; Vol. 11, p 205.

(81)   Hoenig, D.; Moebius, D. *The Journal of Physical Chemistry* **1991**, *95*, 4590.

(82)   Pabst, G.; Koschuch, R.; Pozo-Navas, B.; Rappolt, M.; Lohner, K.; Laggner, P. *Journal of Applied Crystallography* **2003**, *36*, 1378.

(83)   Pabst, G.; Rappolt, M.; Amenitsch, H.; Laggner, P. *Physical Review E* **2000**, *62*, 4000.

(84)   Blaurock, A. E.; Worthington, C. R. *Biophysical Journal* **1966**, *6*, 305.

(85)   Dittrich, M., Universitaet Potsdam, 2012.

(86)   Lindblom, G.; Rilfors, L. *Advances in Colloid and Interface Science* **1992**, *41*, 101.

(87)   Marsh, D. *Chemistry and Physics of Lipids* **2012**, *165*, 59.

(88)   Gill, P.; Moghadam, T. T.; Ranjbar, B. *Journal of Biomolecular Techniques* **2010**, *21*, 167.

(89)   Wölk, C.; Heinze, M.; Kreideweiß, P.; Dittrich, M.; Brezesinski, G.; Langner, A.; Dobner, B. *International Journal of Pharmaceutics* **2011**, *409*, 46.

(90)   Heinze, M.; Brezesinski, G.; Dobner, B.; Langner, A. *Bioconjugate Chemistry* **2010**, *21*, 696.

(91)   Yuba, E.; Nakajima, Y.; Tsukamoto, K.; Iwashita, S.; Kojima, C.; Harada, A.; Kono, K. *Journal of Controlled Release* **2012**, *160*, 552.

(92)   Martini, E.; Fattal, E.; de Oliveira, M. C.; Teixeira, H. *International Journal of Pharmaceutics* **2008**, *352*, 280.

(93)   Walsh, C. L.; Nguyen, J.; Tiffany, M. R.; Szoka, F. C. *Bioconjugate Chemistry* **2013**, *24*, 36.

(94)   Koynova, R.; Tenchov, B. In *Topics in Current Chemistry* 2010; Vol. 296, p 51.

(95)   Patil, S. P.; Yi, J. W.; Bang, E. K.; Jeon, E. M.; Kim, B. H. *MedChemComm* **2011**, *2*, 505.

(96)   Johnsson, M.; Wagenaar, A.; Engberts, J. B. F. N. *Journal of the American Chemical Society* **2003**, *125*, 757.

(97)   Zhu, L.; Lu, Y.; Miller, D. D.; Mahato, R. I. *Bioconjugate Chemistry* **2008**, *19*, 2499.

(98)   Brezesinski, G.; Möhwald, H. *Advances in Colloid and Interface Science* **2003**, *100-102*, 563.

(99)   Kaganer, V. M.; Möhwald, H.; Dutta, P. *Reviews of Modern Physics* **1999**, *71*, 779.

(100)   Bringezu, F.; Dobner, B.; Brezesinski, G. *Chemistry - A European Journal* **2002**, *8*, 3203.

(101)   Brezesinski, G.; Kaganer, V. M.; Möhwald, H.; Howes, P. B. *Journal of Chemical Physics* **1998**, *109*, 2006.

(102)   Kaganer, V. M.; Loginov, E. B. *Physical Review E* **1995**, *51*, 2237.

(103)   Kenn, R. M.; Böhm, C.; Bibo, A. M.; Peterson, I. R.; Möhwald, H.; Als-Nielsen, J.; Kjaer, K. *Journal of Physical Chemistry* **1991**, *95*, 2092.

(104)   Durbin, M. K.; Malik, A.; Ghaskadvi, R.; Shih, M. C.; Zschack, P.; Dutta, P. *Journal of Physical Chemistry* **1994**, *98*, 1753.

(105)   Israelachvili, J. *Intermolecular and Surface Forces*, 2011.

(106)   Brewer, S. H.; Anthireya, S. J.; Lappi, S. E.; Drapcho, D. L.; Franzen, S. *Langmuir* **2002**, *18*, 4460.

(107)   Chen, Q.; Kang, X.; Li, R.; Du, X.; Shang, Y.; Liu, H.; Hu, Y. *Langmuir* **2012**, *28*, 3429.

(108)   Tsuboi, M. *Appl. Spectrosc. Rev.* **1970**, *3*, 45.

(109)   Garidel, P.; Blume, A. *Biochimica et Biophysica Acta - Biomembranes* **1998**, *1371*, 83.

(110)   Dörfler, H. D.; Brezesinski, G.; Miethe, P. *Chemistry and Physics of Lipids* **1988**, *48*, 245.

(111)   Blume, A.; Tuchtenhagen, J. *Biochemistry* **1992**, *31*, 4636.

(112)   Garti, N.; Karpuj, L.; Sarig, S. *Thermochimica Acta* **1980**, *35*, 343.

(113)   Garti, N.; Karpuj, L.; Sarig, S. *Journal of Lipid Research* **1981**, *22*, 785.

(114)   May, S.; Ben-Shaul, A. *Current medicinal chemistry* **2004**, *11*, 151.

(115)   Cherezov, V.; Qiu, H.; Pector, V.; Vandenbranden, M.; Ruysschaert, J. M.; Caffrey, M. *Biophysical Journal* **2002**, *82*, 3105.

(116)   Behr, J. P.; Demeneix, B.; Loeffler, J. P.; Perez-Mutul, J. *Proceedings of the National Academy of Sciences of the United States of America* **1989**, *86*, 6982.

(117)   Liu, D.; Qiao, W.; Li, Z.; Chen, Y.; Cui, X.; Li, K.; Yu, L.; Yan, K.; Zhu, L.; Guo, Y.; Cheng, L. *Chemical Biology & Drug Design* **2008**, *71*, 336.

(118)   Soltan, M. K.; Ghonaim, H. M.; El Sadek, M.; Kull, M. A.; El-Aziz, L. A.; Blagbrough, I. S. *Pharmaceutical Research* **2009**, *26*, 286.

(119)   Wölk, C.; Drescher, S.; Meister, A.; Blume, A.; Langner, A.; Dobner, B. *Chemistry – A European Journal* **2013**, *19*, 12824.

(120)   Janich, C.; Wölk, C.; Taßler, S.; Drescher, S.; Meister, A.; Brezesinski, G.; Dobner, B.; Langner, A. *European Journal of Lipid Science and Technology* **2014**.

(121)   Lipowsky, R. In *Handbook of Biological Physics* 1995; Vol. 1, p 521.

(122)   Grigoriev, D.; Miller, R.; Wüstneck, R.; Wüstneck, N.; Pison, U.; Möhwald, H. *Journal of Physical Chemistry B* **2003**, *107*, 14283.

(123)   Sakamoto, N.; Sakai, K.; Takagi, K. *Physical Review E - Statistical Physics, Plasmas, Fluids, and Related Interdisciplinary Topics* **1997**, *56*, 1838.

(124)   López-Montero, I.; Arriaga, L. R.; Rivas, G.; Vélez, M.; Monroy, F. *Chemistry and Physics of Lipids* **2010**, *163*, 56.

(125)   Lucero, A.; Rodríguez Niño, M. R.; Gunning, A. P.; Morris, V. J.; Wilde, P. J.; Rodríguez Patino, J. M. *The Journal of Physical Chemistry B* **2008**, *112*, 7651.

(126)   Niño, M. R. R.; Caro, A. L.; Patino, J. M. R. *Colloids and Surfaces B: Biointerfaces* **2009**, *69*, 15.

(127)   Montanha, E. A.; Pavinatto, F. J.; Caseli, L.; Kaczmarek, O.; Liebscher, J.; Huster, D.; Oliveira, O. N. *Colloids and Surfaces B: Biointerfaces* **2010**, *77*, 161.

(128)   Dluhy, R. A.; Cornell, D. G. *Journal of Physical Chemistry* **1985**, *89*, 3195.

(129)   Blaudez, D.; Buffeteau, T.; Cornut, J. C.; Desbat, B.; Escafre, N.; Pezolet, M.; Turlet, J. M. *Applied Spectroscopy* **1993**, *47*, 869.

(130)   Mendelsohn, R.; Mao, G.; Flach, C. R. *Biochimica et Biophysica Acta (BBA) - Biomembranes* **2010**, *1798*, 788.

(131)   Cameron, D. G.; Kauppinen, J. K.; Moffatt, D. J.; Mantsc, H. H. *Applied Spectroscopy* **1982**, *36*, 245.

(132)   Antipina, M. N.; Dobner, B.; Konovalov, O. V.; Shapovalov, V. L.; Brezesinski, G. *Journal of Physical Chemistry B* **2007**, *111*, 13845.

(133)   Heyes, J.; Palmer, L.; Bremner, K.; MacLachlan, I. *Journal of Controlled Release* **2005**, *107*, 276.

(134)   Koynova, R.; Tenchov, B.; Wang, L.; MacDonald, R. C. *Molecular Pharmaceutics* **2009**, *6*, 951.

(135)   Leveiller, F.; Jacquemain, D.; Lahav, M.; Leiserowitz, L.; Deutsch, M.; Kjaer, K.; Als-Nielsen, J. *Science* **1991**, *252*, 1532.

(136)   Mariani, P.; Luzzati, V.; Delacroix, H. *Journal of Molecular Biology* **1988**, *204*, 165.

(137)   Safinya, C. R.; Roux, D.; Smith, G. S.; Sinha, S. K.; Dimon, P.; Clark, N. A.; Bellocq, A.

M. *Physical Review Letters* **1986**, *57*, 2718.

(138) Gericke, A.; Hühnerfussf, H. *Berichte der Bunsengesellschaft für physikalische Chemie* **1995**, *99*, 641.

(139) Tenchov, B.; Koynova, R.; Rapp, G. *Biophysical Journal* **1998**, *75*, 853.

(140) Shyamsunder, E.; Gruner, S. M.; Tate, M. W.; Turner, D. C.; So, P. T. C.; Tilcock, C. P. S. *Biochemistry®* **1988**, *27*, 2332.

(141) Flach, C. R.; Gericke, A.; Mendelsohn, R. *Journal of Physical Chemistry B* **1997**, *101*, 58.

(142) Muenter, A. H.; Hentschel, J.; Borner, H. G.; Brezesinski, G. *Langmuir* **2008**, *24*, 3306.

(143) Andreeva, T. D.; Petrov, J. G.; Brezesinski, G.; Moehwald, H. *Langmuir* **2008**, *24*, 8001.

(144) Rapp, G.; Gabriel, A.; Dosière, M.; Koch, M. H. J. *Nuclear Inst. and Methods in Physics Research, A* **1995**, *357*, 178.

(145) Koch, M. H. J.; Bordas, J. *Nuclear Instruments and Methods In Physics Research* **1983**, *208*, 461.

(146) Boulin, C. J.; Kempf, R.; Gabriel, A.; Koch, M. H. J. *Nuclear Inst. and Methods in Physics Research, A* **1988**, *269*, 312.

ACKNOWLEDGEMENT

SUPPORTING INFORMATION

SUPPORTING INFORMATION TO CHAPTER 1

THE INFLUENCE OF CHAIN PURITY ON THE PHYSICAL-CHEMICAL PROPERTIES AND TRANSFECTION EFFICIENCY
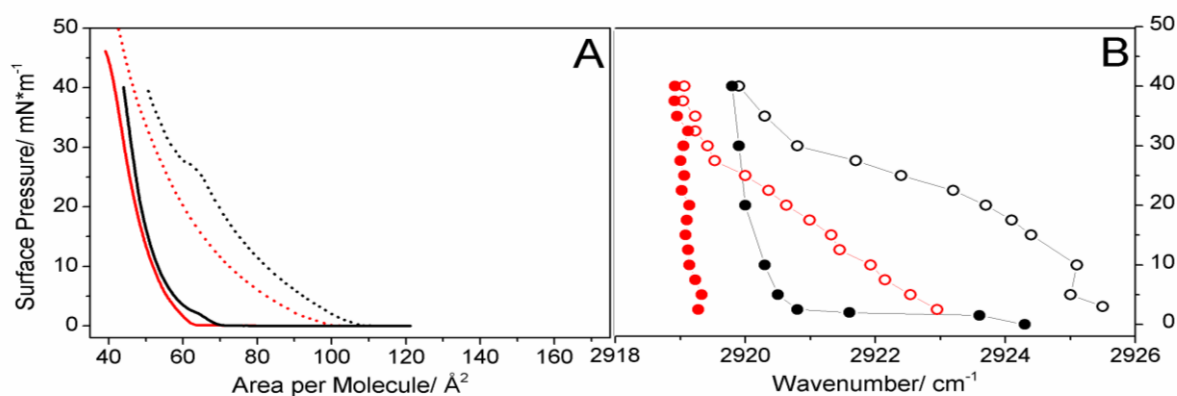
S1.1 ISOTHERMS AND IRRAS OF LIPID 8P AND LIPID 8

Fig. S1. 1 Pressure/area isotherms (A) and the positions of ν_{as} (CH$_2$) band along the compression isotherm at 5 °C (B) of lipid **8p** (black) and lipid **8** (red) on buffers: citric buffer pH 4 (A: dashed line, B: empty circles) and carbonate buffer pH 10 (A: solid line; B: filled circles).

S1.2 BREWSTER ANGLE MICROSCOPY (BAM) OF LIPID 8

A　　　　　　　　　　　　B　　　　　　　　　　　　C
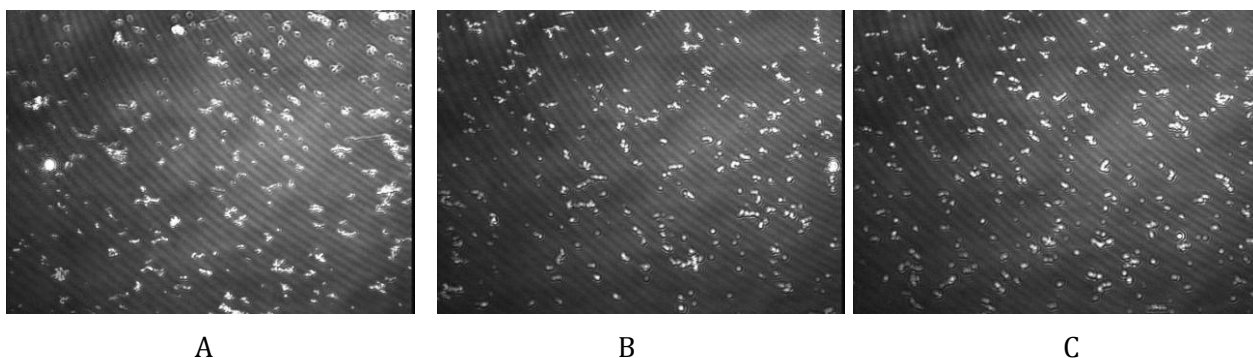
Fig. S1. 2 BAM pictures of lipid 8 at pH4, 5mM citrate buffer, at 20°C and different surface pressures: A – 0.3 mN/m, B – 0.6 mN/m and C – 5.0 mN/m

S1.3 GIXD OF LIPID 8P

Table S1.1 Bragg Peaks (Q_{xy}) and Bragg rods (Q_z) maxima, tilt angle (t), distortion (d) and their directions and chain cross-sectional area (A_0) of lipid 8p and lipid 8 at different surface pressures (π) at pH 4 and pH 10 or pH 8 at 5 °C. The index d denotes the degenerated and n-d the non-degenerated peaks. Values given in *italics* for lipid 8 at pH 8 correspond to the lattice of other components of the lipid 8 system.

π/mN/m	Q_{xy}^d/Å^{-1}	Q_{xy}^{n-d}/Å^{-1}	Q_z^d/Å^{-1}	Q_z^{n-d}/Å^{-1}	t / °	$t_{direction}$	d	$d_{direction}$	A_0/Å^2
				Lipid 8p at pH10					
5	1.463	1.447	0.225	0.45	17.3	NNN	0.0146	NNN	20.5
10	1.465	1.455	0.2235	0.447	17.1	NNN	0.0091	NNN	20.4
15	1.467	1.462	0.219	0.438	16.7	NNN	0.0045	NNN	20.3
20	1.467	1.471	0.200	0.400	15.2	NNN	0.0036	NN	20.4
30	1.471	1.499	0.190	0.380	14.2	NNN	0.0253	NN	20.2
				Lipid 8 at pH4					
40	1.516	1.482	0.080	0	3.46	NN	0.0300	NNN	20.1
				Lipid 8 at pH8					
10	1.459	1.443	0.249	0.498	19.0	NNN	0.0146	NNN	20.4
	1.528	*1.481*	*0.263*	*0*	*11.2*	*NN*	*0.0412*	*NNN*	*19.5*
20	1.470	1.462	1.470	0.409	15.6	NNN	0.0073	NNN	20.4
	1.532	*1.481*	*0.232*	*0*	*9.8*	*NN*	*0.0446*	*NNN*	*19.6*
30	1.480	1.468	1.480	0.388	14.8	NNN	0.0108	NNN	20.2
	1.542	*1.486*	*0.214*	*0*	*9.0*	*NN*	*0.0487*	*NNN*	*19.4*

S1.4 DSC OF LIPID 8P/CHOLESTEROL AND LIPID 8P/CHOLESTEROL/DNA COMPLEXES
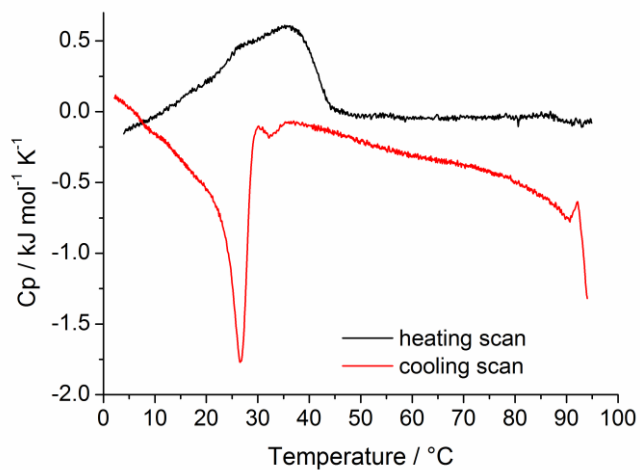
Fig. S1. 3 The DSC heating/cooling scans of lipid **8p**/chol (1:1) dispersion in water.
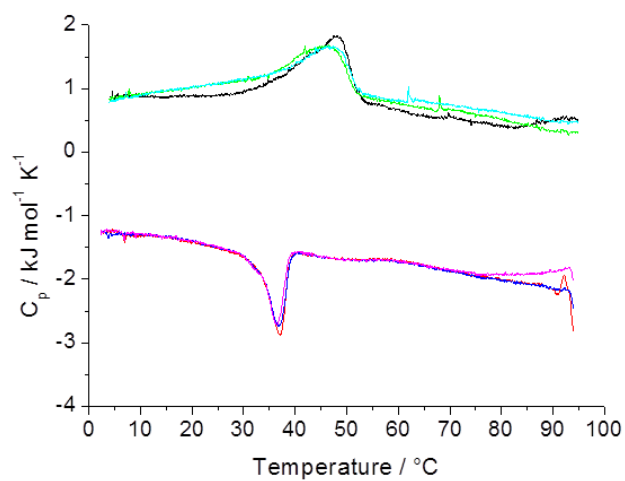
Fig. S1. 4 Repeated DSC heating/cooling scans of lipid **8p**/chol (1:1)/ DNA (N/P 3:1) dispersion in water.

SUPPORTING INFORMATION TO CHAPTER 2

THE INFLUENCE OF THE LIPID HEADGROUP STRUCTURE ON PHYSICAL-CHEMICAL PROPERTIES AND TRANSFECTION EFFICIENCY
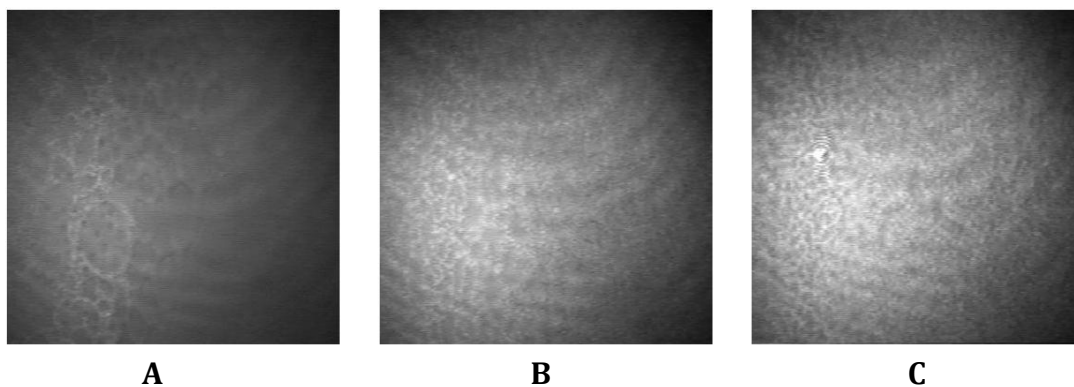
S2.1 BAM PICTURES OF E14/16 AND E14/16LYS

A   **B**   **C**

Fig. S2. 1 BAM pictures of E14/16 spread on water at 20 °C at: A – 0mN/m, B –15 mN/m, C –20 mN/m.

A   **B**   **C**

D   **E**   **F**
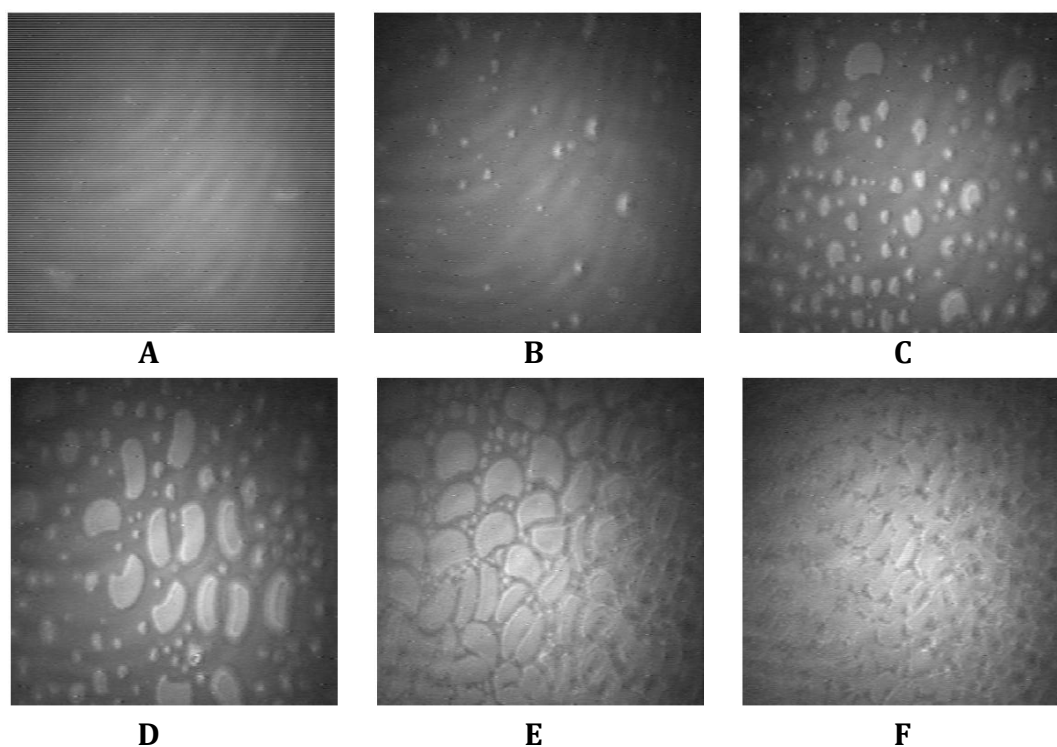
Fig. S2. 2 BAM pictures of E14/16 spread on water at 20 °C at A – 31 mN/m, B – 39 mN/m, C – 41 mN/m, D - 43 mN/m, E – 45 mN/m and F – 48 mN/m.

THE INFLUENCE OF CHAIN STRUCTURE ON THE PHYSICAL-CHEMICAL PROPERTIES AND TRANSFECTION EFFICIENCY

S3.1 SAXS OF TT10 AND TO10 AT DIFFERENT PH
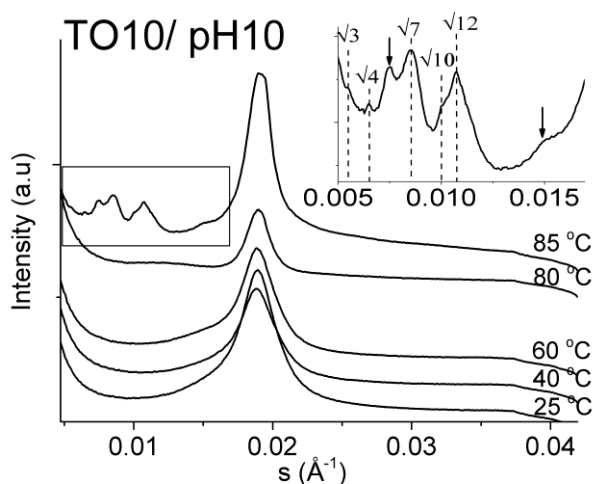
Fig. S3. 1 SAXS temperature scan of TO10 at pH 10. The inset shows magnified region marked with rectangle for the pattern at 85 ºC. Indexed peaks belong to cubic phase of Ia3d symmetry (peaks at √8 and √11 are missing) and reflexes marked with arrows come from coexisting fluid lamellar phase of TO10.
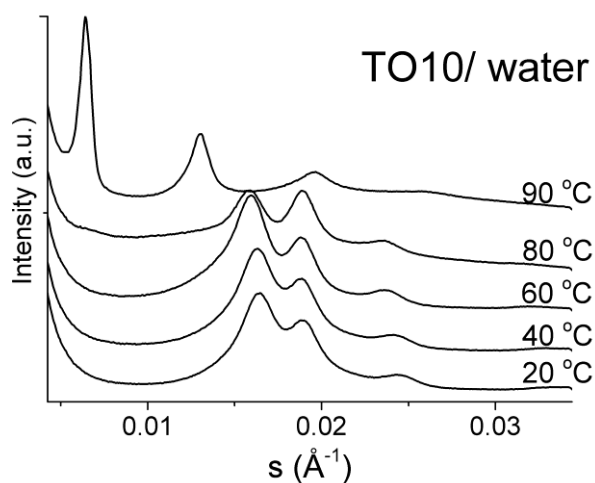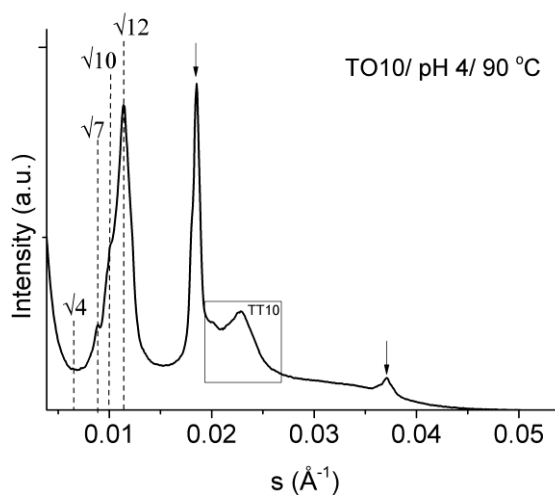

Fig. S3. 2 SAXS temperature scan of TO10 in water.

Fig. S3. 3 SAXS temperature scan of TO10 at pH 4 at 90 ℃. Indexed peaks belong to cubic phase of Ia3d symmetry (peaks at √3, √8 and √11 are missing), reflexes marked with arrows come from coexisting fluid lamellar phase of TO10 and the region identified with a rectangle comes from TT10 – one of components of the multicomponent TO10 system.
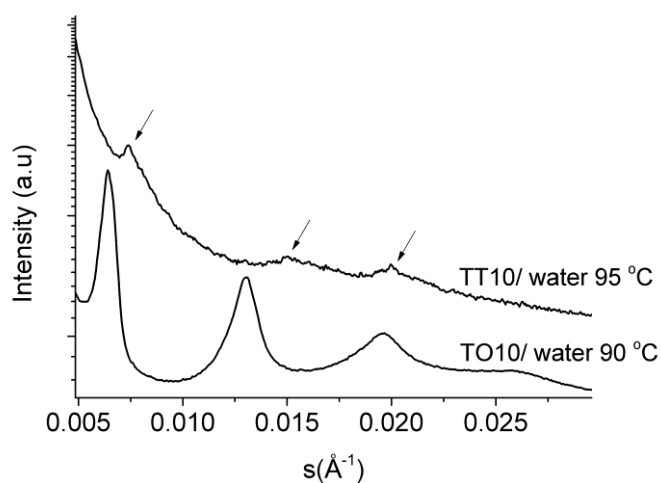

Fig. S3. 4 SAXS patterns of TT10 and TO10 in water above the phase transition temperatures. Both lipids show lamellar fluid phase (L$_\alpha$). Peaks of three orders of TT10 have been indicated by arrows for clarity.
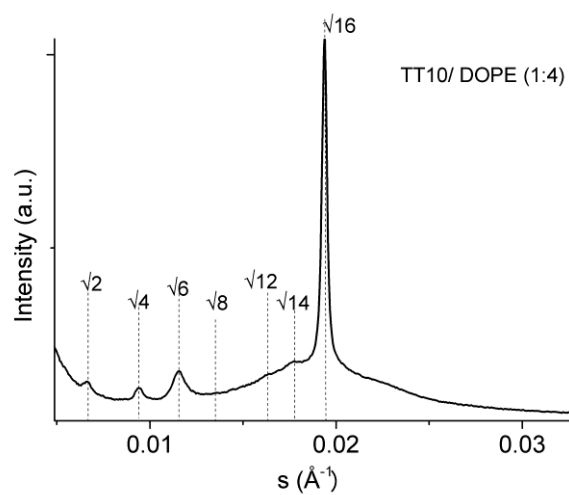
Fig. S3. 5 SAXS pattern of TT10/ DOPE (1:4) mixture in water at 20 ºC. Indexed peaks belong to cubic Im3m phase. The reflex at $\sqrt{10}$ is missing.

Eidesstattliche Erklärung

Hiermit erkläre ich gemäß der Promotionsordnung der Naturwissenschaftlichen Fakultät I (Biowissenschaften) der Martin-Luther-Universität Halle-Wittenberg, dass ich die vorliegende Dissertationsschrift selbstständig und ohne fremde Hilfe angefertigt habe. Weiterhin habe ich keine anderen als die angegebenen Quellen und Hilfsmittel verwendet und die daraus wörtlich und inhaltlich entnommenen Stellen als solche kenntlich gemacht.

Die Dissertation wurde ausschließlich der Mathematisch-Naturwissenschaftlichen-Fakultät I der Martin-Luther-Universität Halle-Wittenberg vorgelegt und an keiner anderen universitären Einrichtung weder im In- noch im Ausland zur Erlangung des Doktorgrades eingereicht. Des Weiteren habe ich bis zum jetzigen Zeitpunkt keine Promotionsversuche unternommen.

_____

Halle (Saale) im November 2014   Dorota Pawlowska